Phase Change Materials for Thermal Management in Thermal Energy Storage Applications

by

Talal Saeed Alqahtani

A Dissertation Presented in Partial Fulfillment
of the Requirements for the Degree
Doctor of Philosophy

Approved July 2020 by the
Graduate Supervisory Committee:

Patrick E. Phelan, Chair
Abdelrahman Shuaib
Sofiene Mellouli
Robert Wang
Bin Mu

ARIZONA STATE UNIVERSITY

August 2020

بسم الله الرحمن الرحيم

ABSTRACT

Thermal Energy Storage (TES) is of great significance for many engineering applications as it allows surplus thermal energy to be stored and reused later, bridging the gap between requirement and energy use. Phase change materials (PCMs) are latent heat-based TES which have the ability to store and release heat through phase transition processes over a relatively narrow temperature range. PCMs have a wide range of operating temperatures and therefore can be used in various applications such as stand-alone heat storage in a renewable energy system, thermal storage in buildings, water heating systems, etc. In this dissertation, various PCMs are incorporated and investigated numerically and experimentally with different applications namely a thermochemical metal hydride (MH) storage system and thermal storage in buildings. In the second chapter, a new design consisting of an MH reactor encircled by a cylindrical sandwich bed packed with PCM is proposed. The role of the PCM is to store the heat released by the MH reactor during the hydrogenation process and reuse it later in the subsequent dehydrogenation process. In such a system, the exothermic and endothermic processes of the MH reactor can be utilized effectively by enhancing the thermal exchange between the MH reactor and the PCM bed. Similarly, in the third chapter, a novel design that integrates the MH reactor with cascaded PCM beds is proposed. In this design, two different types of PCMs with different melting temperatures and enthalpies are arranged in series to improve the heat transfer rate and consequently shorten the time duration of the hydrogenation and dehydrogenation processes. The performance of the new designs (in chapters 2 and 3) is investigated numerically and compared with the conventional designs in the literature. The results

indicate that the new designs can significantly enhance the time duration of MH reaction (up to 87%). In the fourth chapter, organic coconut oil PCM (co-oil PCM) is explored experimentally and numerically for the first time as a thermal management tool in building applications. The results show that co-oil PCM can be a promising solution to improve the indoor thermal environment in semi-arid regions.

DEDICATION

This dissertation is dedicated to my loved ones my parents, Saeed and Nemshah, my uncle Marei, and to my siblings, Hussain, Fatimah, Sattam, Mohammed, Nora and Dalia for their prayers, love and continuous encouragement.

Last, but certainly not least, this dissertation is dedicated to my beloved my wife Nora and my sons, Muhannad, Yosef and Yazan, who have been the light of my life and who have given me the extra strength and motivation to get my PhD journey done.

This dissertation would not have been possible without you.

ACKNOWLEDGMENTS

All praise is to Allah, the Almighty, for having made everything possible and for giving me strength throughout my life and ever more during my study journey to make my dream come true.

My sincere gratitude to my advisor Prof. Patrick Phelan can't be expressed in words. Thank you, Pat, for your friendship, guidance, immense knowledge, insightful comments and encouragement. I could not have imagined having a better advisor and mentor for my PhD study.

I also extend my sincere gratitude to my committee members Dr. Abdelrahman Shuaib, Dr. Robert Wang and Dr. Bin Mu for their insightful comments and valuable discussions. A special sincere appreciation goes to my committee member Dr. Sofiene Mellouli. Thank you, Sofiene, for your immense knowledge, continuous support and for being friend.

My deepest gratitude and sincere thanks to my friend Ahmad Bamasag for his unending support over the period of this journey. Thank you for the talks, the walks, the discussions and all the moments that we have shared.

Besides, a deep appreciation goes to my colleague Prof. Faouzi Askri for providing me with his immense knowledge and for his undying belief in me from our first meeting.

The last word goes for my sponsor, King Khalid University, for financing my studies and for supporting me through my study. Looking forward to sharing what I've learned.

TABLE OF CONTENTS

Page

CHAPTER Page

LIST OF TABLES

Table Page

LIST OF FIGURES

Figure Page

Figure Page

Figure Page

Figure Page

NOMENCLATURE

A, B	plateau pressure coefficients
C	reaction rate constant, s^{-1}
C_p	heat capacity, J kg^{-1} K^{-1}
D	thickness, m
E	activation energy, J mol^{-1}
$E_{inner-PCMs}$	storage capacity of the inner PCMs amount, J
$E_{opt-tot-PCMs}$	total storage capacity of the PCMs at the optimum ϕ_{PCM591}, J
$E_{tot-PCMs}$	total storage capacity of the PCMs, J
E_{PCM580}	storage capacity of PCM580 amount, J
E_{PCM591}	storage capacity of PCM591 amount, J
E_{stor}	stored energy, J m^{-2}
f	liquid fraction
h	convective heat transfer, W m^{-2} °C^{-1}
h_{sen}	sensible enthalpy, J kg^{-1}
H	height, m
H_{PCM}	total enthalpy of PCM, J kg^{-1}
K	permeability, m^2
L	latent heat of PCM, J kg^{-1}
L_g	typical gas diffusion length, m
L_{heat}	typical heat diffusion length, m
M	molecular mass, kg mol^{-1}
$\vec{n}$	normal vector
Nu	Nusselt number H_2
P	pressure, bar
q_r	average solar heat flux (W m^{-2})
R	radius, m
R_g	universal gas constant, J mol^{-1} K^{-1}
S	source term, W m^{-3}
t	time, s
T	Temperature, K
V	volume, m^3
wt	maximum mass content of hydrogen in the metal, %
x	space coordinate, m

X	position of the liquid/solid front, m
X_{H_2}	absorbed hydrogen amount, *wt*%

Abbreviations

co-oil	coconut oil
MH	metal hydride
PCM	phase change material
TES	thermal energy storage

Greek symbols

ΔH_{mol}	molar enthalpy of reaction, J mol^{-1}
ΔH	latent heat of fusion, J kg^{-1}
ΔT	temperature difference, °C
$\Delta\varphi$	humidity difference, %
ρ	density, kg m^{-3}
φ	humidity, %
λ	thermal conductivity, W m^{-1} K^{-1}
ε	porosity
μ	dynamic viscosity of hydrogen, Pa s
ϕ_{PCM591}	distribution ratio of the storage capacity of PCM591 to the total PCMs' storage capacity
$\phi_{inner\text{-}PCMs}$	distribution ratio of the storage capacity of the inner PCMs to the total PCMs' storage capacity at the optimum ϕ_{PCM591}

subscripts

0	initial
abs	absorption
ch	charging
d	daytime
des	desorption
disch	discharging
DN	difference

eff	effective
eq	equilibrium
g	gas
H	highest
H_2	hydrogen
l	liquid region
L	lowest
m	melting
max	maximum
MH	metal hydride
mol	molar
n	nighttime
opt	optimum
PCM	phase change material
PCM580	phase change material with melting temperature of 580 K
PCM591	phase change material with melting temperature of 591 K
s	solid region
sen	sensible
sol	solidification
ref	reference

Superscript

CB	control building
E	environment
TB	test building

1. INTRODUCTION

The improvement of the performance of thermal energy storage (TES) systems is an active area of research. TES is a temporary storage of high- or low-temperature thermal energy for later use, bridging the gap between requirement and energy use. This has made TES technologies an essential option for many applications. However, the markets are looking for new TES technologies which can be used to reduce electricity consumption and its dependency on fossil fuels, to make use of renewable energy sources and to contribute to match energy supply and demand efficiently. TES systems can be categorized into three types: sensible heat, latent heat, and thermo-chemical. Among all thermal storage methods, latent heat storage has the most flexible operating temperature range and therefore can be used in many engineering applications [1]. Phase change materials (PCMs) are known as the materials used for latent heat TES that have the ability to store and release heat through phase transition processes over a relatively narrow temperature range.

As evident from the literature, phase change materials (PCMs) have brought a revolution in many engineering fields [1]. They have a variety of applications in TES units, heating and cooling systems, thermal comfort inside buildings and in textiles etc. PCMs have many advantages like high latent heat storage capacity, useful solid-liquid phase change temperatures, thermal reliability and low cost. PCMs suffer, however, from low thermal conductivity. An ideal PCM should have the above properties along with high thermal conductivity. Due to their typically low thermal conductivity, the heat storage and release rates of PCM are quite low, which lengthens the time required for the change of phase, resulting in less efficient thermal storage and thus limiting their practical applications. This

problem persists with most of the PCM categories except for metals. So, thermal storage systems should be designed such as to enhance the heat transfer rate and the utilization of stored energy.

1.1 Motivation

- Thermo-chemical metal hydride (MH) storage systems are considered as an attractive option and economically viable for renewable energy sources due to their high volumetric energy density, high efficiency, low costs and safety advantages [2–4]. MHs release heat when they are loaded with pressurized hydrogen; however, they require heat while releasing hydrogen. Hence, these MHs necessitate an external source of heat during the unloading process. The requirement of an electrical apparatus to generate the required heat for the dehydrogenation process which is lost during the hydrogenation process is the major drawback of the MH storage system. Thereby the overall efficiency of the MH storage device is reduced. Development of new devices that solve this problem is a necessity. One of the options, which will be described in this dissertation, is that the thermal energy generated by the MH is recuperated by a PCM-based latent heat TES system. Thus, the use of PCMs is an elegant solution to store the generated heat throughout the hydrogenation process and reuse it in the subsequent dehydrogenation process.
- The energy consumption by the building sector represents roughly 40% of total global consumption as a result of the excessive use of air conditioning and heating systems [5]. PCMs are proving to be a viable option for solving this problem in buildings. However, the performance of PCMs in building applications is directly affected by

climatic conditions [6,7]. In certain climate regions, using a proper PCM may minimize or completely eliminate the need for air conditioning.

- A recent literature review reveals that PCM-based TES systems necessitate engineers and researchers to focus their efforts on the development of experimental studies and numerical simulations to achieve optimal design of PCM-based TES systems, dynamic analysis of the thermal storage systems to predict their thermal performance, and to integrate PCM in various applications [8].

1.2 Research Objective

The objective of this dissertation is to assess the overall thermal performance of integrating PCMs into a thermo-chemical metal hydride storage system, and in a building application. This assessment is based on the following:

- Conduct numerical and experimental investigations to analyze the working characteristics of these systems.
- Perform a detailed analysis to monitor the impact of the PCM on the overall performance of these systems.
- Use suitable PCMs based on their thermophysical properties to achieve the highest efficacy with the integrated applications.
- Propose new designs for MH-PCM storage systems.
- Develop rigorous mathematical models to evaluate the efficacy of the proposed designs for MH-PCM systems.

1.3 Dissertation Structure

This dissertation is structured into three main parts, each one concerning a potential application of a TES system based on PCM. The PCM is integrated into different applications in the three parts of the dissertation with the goal of improving the overall thermal performance of these applications.

Chapter 2: Metal hydride reactor encircled by PCM sandwich bed – presents a numerical analysis of a new design of a thermo-chemical storage system equipped with PCM. The new design consists of a metal hydride (MH) reactor encircled by a PCM sandwich bed.

Chapter 3: Metal hydride reactor encircled by cascaded PCM beds – presents a numerical analysis of a novel design of an MH reactor equipped with PCMs. In the new design, cascaded PCM beds are integrated into the MH reactor.

Chapter 4: Unconditioned building equipped with coconut oil PCM – presents an experimental and numerical assessment of using coconut oil as a PCM for unconditioned buildings.

Chapter 5: Conclusion – presents conclusions from the entire study.

1.4 Publications

Papers included in this dissertation:

I. **T. Alqahtani**, S. Mellouli, A. Bamasag, F. Askri, & P.E. Phelan, Thermal performance analysis of a metal hydride reactor encircled by a phase change material sandwich bed, *Int. J. Hydrog. Energy*. (in press, 2020).

II. **T. Alqahtani**, A. Bamasag, S. Mellouli, F. Askri, & P.E. Phelan, Cyclic behaviors of a novel design of a metal hydride reactor encircled by cascaded phase change materials. Manuscript submitted for publication.

III. **T. Alqahtani**, S. Mellouli, A. Bamasag, F. Askri, & P. Phelan, Experimental and numerical assessment of using coconut oil as a phase-change material for unconditioned buildings, *Int J Energy Res.* (2020) 1–20. doi:10.1002/er.5176.

Papers not included in this dissertation:

I. **T. Alqahtani**, S. Mellouli, F. Askri, & P.E. Phelan, Performance analysis of a metal hydride-thermal energy storage system for concentrating solar power plants, ASTFE Digit. Libr. (2019) 1667–1676. doi:10.1615/TFEC2019.sol.027379.

II. A. Bamasag, **T. Alqahtani**, S. Sinha, P. Phelan, Experimental Investigation of a Membrane Distillation System Using Solar Evacuated Tubes, ASME 2019 Int. Mech. Eng. Congr.

III. R. Elarem, **T. Alqahtani**, S. Mellouli, F. Askri, A. Edacherian, T. Vineet, I.A. Badruddin, J. Abdelmajid, A comprehensive review of heat transfer intensification methods for latent heat storage units, Energy Storage. (2020) 1–30. doi:10.1002/est2.127.

IV. A. Bamasag, **T. Alqahtani**, S. Sinha, N. Ghaffour, P. Phelan, Experimental investigation of a solar-heated direct contact membrane distillation system using evacuated tube collectors, Desalination. 487 (2020) 114497. doi:10.1016/j.desal.2020.114497.

V. S. Mellouli, F. Askri, A. Edacherian, **T. Alqahtani**, S. Algarni, J. Abdelmajid, P. Phelan, Performance analysis of a thermal energy storage system based on paired metal hydrides for concentrating solar power plants, Appl. Therm. Eng. 144 (2018). doi:10.1016/j.applthermaleng.2018.09.014.

VI. A. Bamasag, **T. Alqahtani**, S. Sinha, N. Ghaffour, P. Phelan, Solar-heated submerged vacuum membrane distillation system with agitation techniques for desalination. Manuscript submitted for publication.

VII. R. Elarem, **T. Alqahtani**, S. Mellouli, A. Edacherian, F. Askri, J. Abdelmajid, Thermal Performance Study of a Metal Hydride Bed Equipped With Nano-Enhanced PCM and U-Tube Heat Exchanger Using Nanofluid for Heat Reaction Recovery. Manuscript submitted for publication.

VIII. S. Algarni, S. Mellouli, **T. Alqahtani**, K. Almutairi, A. khan, A. Anqi, Experimental investigation of an evacuated tube solar collector incorporating nano-enhanced PCM as a thermal booster. Manuscript submitted for publication.

2. METAL HIDRIDE REACTOR ENCIRCLED BY PCM SANDWICH BED[1]

The scarcity and pollution of fossil fuels mandate the need for sustainable energy resources. Concentrating solar power (CSP) plants are recognized nowadays as one of the most important renewable energy sources, as they have a high potential to provide highly dispatchable power among all others [2]. However, such methods of energy generation suffer from their intermittent nature and must therefore be combined with thermal energy storage (TES) systems. TES systems can be categorized into three types: sensible heat, latent heat, and thermo-chemical. Among all thermal storage methods, latent and thermo-chemical heat storage were found to be the most attractive because of their high volumetric energy density [1].

Among the thermo-chemical storage systems that are currently being considered (metallic hydrides, carbonates, hydroxides, redox, and ammonia systems) [9–11], metal hydrides (MH) are a very appealing option for numerous reasons. Indeed, MH has high volumetric energy density, high efficiency, low costs and safety advantages [3,4,12]. However, because of their low thermal conductivities [13], MH systems suffer from slow charging and discharging times, a key performance criterion in MH systems [14,15].

MH storage systems have been widely investigated in the literature [16–19]. MH storage systems are considered viable and cost effective for many applications such as fuel cells

[1] Accepted in the International Journal of Hydrogen Energy as:

***T. Alqahtani**, S. Mellouli, A. Bamasag, F. Askri, P.E. Phelan, Thermal performance analysis of a metal hydride reactor encircled by a phase change material sandwich bed, Int. J. Hydrog. Energy. (in press, 2020).*

[20,21], CSP [22–26] and water pumping systems [27,28]. Recent studies have concentrated more on improving the heat transfer rate in MH storage systems *internally* (i.e., within the MH reactor) and *externally* (i.e., outside the MH reactor) in order to achieve shorter times of reaction [29–31].

2.1 Review of Literature

The augmentation methods to enhance the heat transfer rate *internally* include adding high conductivity porous matrices [32], embedding cooling tubes within the bed such as a bank of tubes [33,34], finned tubes [35–37], finned spiral tubes [38–40], and/or the use of additives (e.g., graphite) [41]. Mellouli et al. [32] found that adding aluminum foam to the MH reactor decreases the hydrogenation time by 60% when compared to that without aluminum foam. A numerical study by Askri et al. [35] found that the use of an annular finned cylindrical storage bed can reduce the hydrogenation time by 40%. Embedding a cooling finned spiral tube into MH reactors was investigated experimentally by Dhaou et al. [39] and it was found that it significantly decreased the hydrogenation/dehydrogenation time. Another technique to enhance the internal heat transfer rate in MHs is to enhance their thermal conductivity by using additive materials. Chaise et al. [41] studied the effect of adding natural graphite (ENG) into magnesium hydride (MgH_2) powders under an argon atmosphere. The results showed that, when 20% of ENG is added, the filling time of hydrogen was reduced by 25 minutes due to the improvement in thermal conductivity. The study found that a similar reduction time can be achieved with 5% of ENG if copper finned tubes were used.

To improve the heat transfer rate of MH reactors *externally*, researchers have proposed the use of passive cooling systems such as phase change materials (PCMs) [29,42]. This allows PCM to store the heat produced throughout the hydrogenation process and to release it later throughout the dehydrogenation process when the MH needs input heat. The use of PCMs has been intensively investigated in many applications such as stand-alone heat storage in CSP systems [43], thermal storage in buildings [44], in thermal regulating textiles [45], and in solar water heating [46]. However, relatively few researchers [42,47–55] have studied the integration of PCMs with MH storage systems as summarized in Table 2.1. Garrier et al. [47] experimentally investigated the integration of PCM with a magnesium hydride storage bed. The results revealed that the charging and discharging time was three hours with 70% storage efficiency. A numerical study was conducted by Mellouli et al. [48] to compare a cylindrical and spherical design of an MH reactor integrated with PCM. The spherical design was found to be 20% faster compared to the cylindrical reactor to store 80% of the hydrogen. Mghari et al. [53] found that the integration of PCM with an MH reactor had a positive effect on the hydrogenation/dehydrogenation time. They concluded that the latent heat of the PCMs had more impact on the system's performance than their thermal conductivity. Nyamsi et al. [54], on the contrary, found that the effect of the PCM thermal conductivity was more important than its latent heat.

The objective of this chapter is to reduce the time-duration of the hydrogenation and dehydrogenation processes in an MH-PCM storage system. To attain this objective, a new design of an MH reactor equipped with PCM is proposed. For this design, the MH reactor is encircled by a cylindrical sandwich bed packed with PCM which increases the heat

transfer area. A detailed analysis of the impacts of volume distribution of PCM in the new design on the time-duration of the hydrogenation and dehydrogenation processes is performed. The outcomes of the study provide insight into the use of a cylindrical sandwich bed packed with PCM as thermal exchange stimulators in MH storage systems.

Table 2.1: Summary of the Studies for Cylindrical MH-PCM Storage Systems.

Study	**Study type**	**Design of PCM bed integrated with a cylindrical MH reactor**	**Metal hydride type**	**PCM type**	**Operating condition**			
					abs		**des**	
					P (bar)	**T (K)**	**P (bar)**	**T (K)**
[47]	Experiment	Pool bed(1)	Mg	$Mg_{69}Zn_{28}Al_3$	10	573	2	633
[48]	2-D simulation	Jacket bed(2)	Mg	$Mg_{69}Zn_{28}Al_3$	10	615	1	617
[49]	2-D simulation	Pool bed(1)	$LiNi_5$	$LiNO_3$-$3H_2O$	10	293	1	-
[50,51]	3-D simulation	Jacket bed(2)	Mg_2Ni	$NaNO_3$	15	579	2	580
[42]	2-D simulation	Pool bed(1)	$LiNi_5$	Rubitherm	10-20	301	1.5-2	305
[52]	2-D simulation	Pool bed(1)	Mg_2Ni	$Mg_{69}Zn_{28}Al_3$	-	-	1	633
[53]	2-D simulation	Pool bed(1)	$LiNi_5$	$LiNO_3$-$3H_2O$	8	293	1	313
[54]	2-D simulation	Pool bed(1)	$LiNi_5$	Rubitherm	3.098	293	-	-
[55]	2-D simulation	Pool bed(1)	$LiNi_5$	Paraffin RT35	8	293	-	-
Present chapter [56]	3-D simulation	Sandwich bed(3)	Mg_2Ni	$NaNO_3$	12	579	3	580

(1) 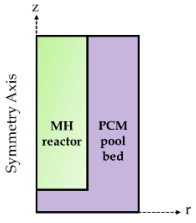

(2) 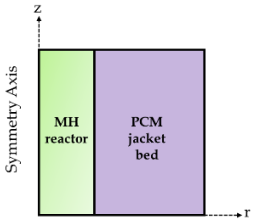

(3) 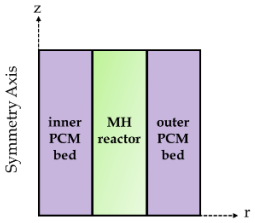

2.2 Models, Method and Validation

2.2.1 Model Description of the MH-PCM System

Two designs of an insulated MH-PCM system are evaluated in this chapter:

Case 1: Figure 2.1(a) shows the conventional design of the MH-PCM system in which the cylinder of the MH is encircled by a cylindrical jacket packed with PCM. It consists of an inner cylindrical tank filled with MH (Mg_2Ni) and an outer cylinder filled with PCM ($NaNO_3$). In this case, the thermal exchange between the MH reactor and the PCM jacket occurs through the interface as indicated in Figure 2.1(a).

Case 2: A new proposed design of the MH-PCM system consists of three concentric cylinders in which the MH reactor is encircled by a cylindrical sandwich bed packed with PCM as illustrated in Figure 2.1(b). In this case, the heat transfer area is increased by increasing the number of interfaces when compared with the conventional design (*case 1*).

The required volume of PCM was calculated by assuming all the released heat from the MH reactor can be totally stored in the PCM (see Eq. (2.12)). For a practical comparison, the total volume of the MH reactor and that of the PCM are kept the same in both cases. However, the volume distribution of the PCM (i.e., the PCM volume in the inner and outer beds) in the new design (*case 2*) is examined and the most effective distribution is identified.

The height and radius of the conventional MH reactor are 100 mm and 20 mm, respectively. The selection of the height and radius was based on the findings reported by the co-author Mellouli et al. [57]. It was found that the ratio of height-to-radius (H/R) of the MH reactor should be greater than 2 in order to achieve better performance. As can be seen, the H/R

ratio is selected to be 5. A small opening with a radius of 4 mm is positioned at the top of the MH reactors in both designs for the injection or extraction of hydrogen. Table 2.2 summarizes the geometrical parameters of the MH-PCM system. The properties of Mg_2Ni are presented in Table 2.3.

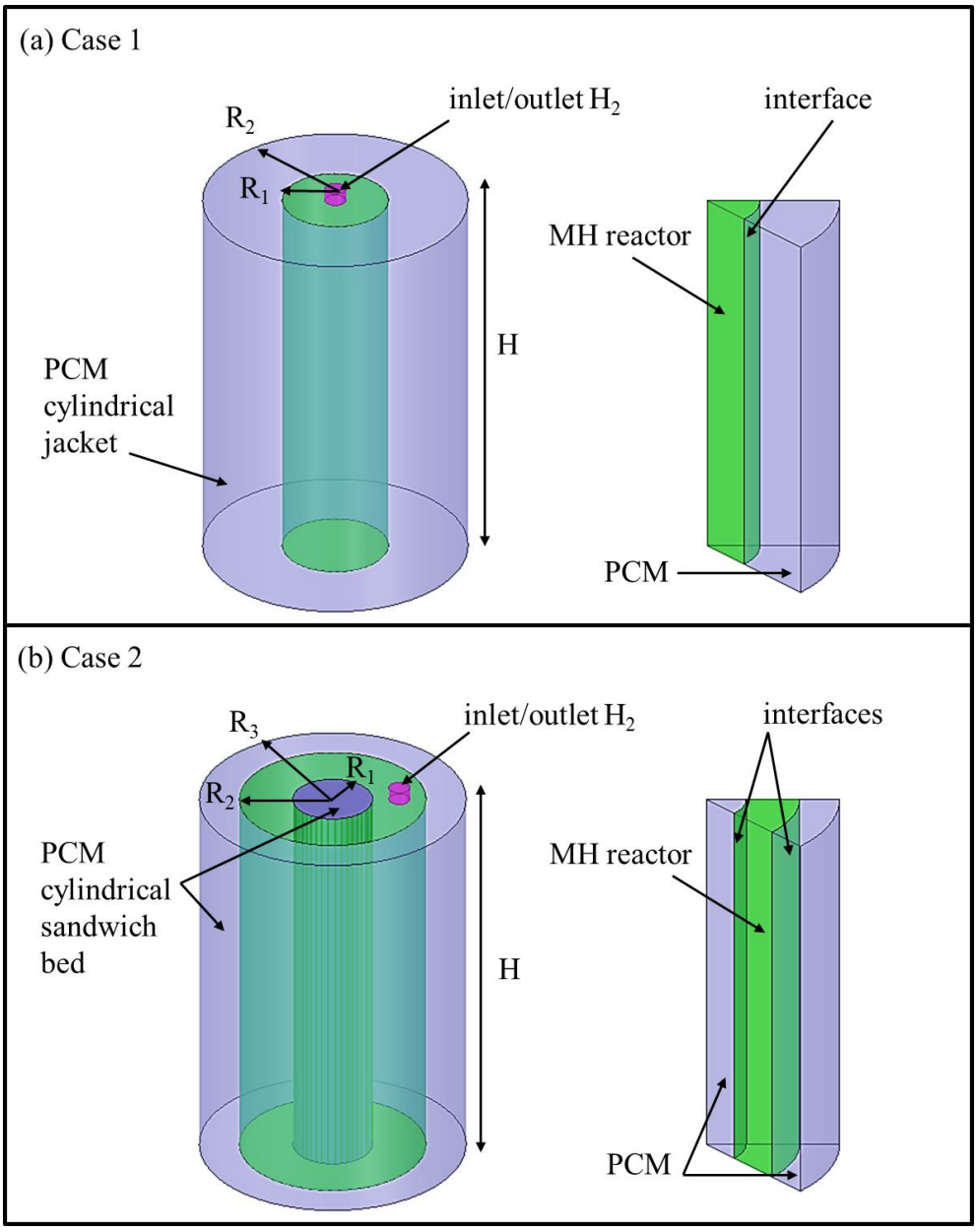

Figure 2.1: Schematics of Simulation Geometries of Two Designs of MH-PCM Storage System: (a) MH Encircled by a Cylindrical Jacket Packed with PCM, (b) MH Encircled by a Cylindrical Sandwich Bed Packed with PCM.

2.2.2 Selection of the PCM

It is challenging to select an appropriate PCM that has a phase-change temperature within the operating temperature range of the Mg_2Ni hydride alloy. Figure 2.2 illustrates the equilibrium chart of the Mg_2Ni-Mg_2NiH_4 system. As this storage system aims to attain an equilibrium state, the operating pressures of the absorption and desorption processes constrain the operating temperatures. The melting temperature of the PCM is therefore obligated to lie in the vicinity of the average temperature of the absorption and desorption processes of the MH bed because it has an influence on the hydrogenation/dehydrogenation process time [50]. In the current chapter, the pressures of the absorption and desorption processes are set to be 12 bar and 3 bar, respectively. Thus, a PCM with a melting temperature of T_m=580 K (i.e., the average temperature of the absorption and desorption processes of the MH reactor) can be chosen. One candidate that meets this criterion is sodium nitrate ($NaNO_3$). Table 2.3 summarizes its properties [51,58].

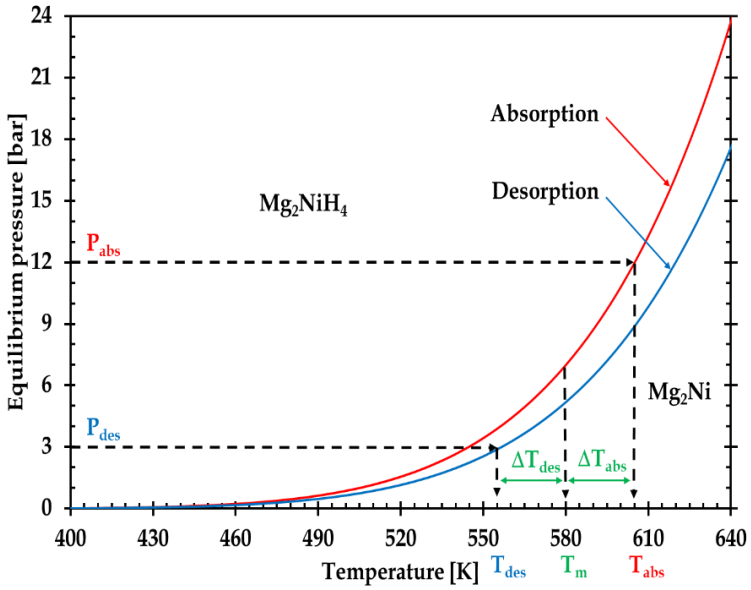

Figure 2.2: Mg_2Ni–Mg_2NiH_4 Equilibrium Chart Showing the Absorption and Desorption Temperatures Imposed by the Absorption and Desorption Pressures.

Table 2.2: Geometrical Parameters of the Simulated Designs.

Parameters		**Values**	
		Case 1	**Case 2**
R_1	[mm]	20	30.6
R_2	[mm]	47.7	36.55
R_3	[mm]	-	47.7
H	[mm]	100	100
The volume occupied by metal hydride, V_{Mg2Ni}	[cm^3]	125.6	125.6
The volume of PCM jacket, $V_{PCM\text{-}jacket}$	[cm^3]	589.14	-
The volume of inner PCM bed, $V_{inner\text{-}PCM}$	[cm^3]	-	294.17*
The volume of outer PCM bed, $V_{outer\text{-}PCM}$	[cm^3]	-	294.98*
* These values are based on the optimum volume distribution of PCM obtained in section 3.1			

Table 2.3: Thermophysical Properties of Mg_2Ni Hydride and the PCM ($NaNO_3$) [50,58,59].

Parameters	**Mg_2Ni hydride**	**PCM ($NaNO_3$)**
Density, ρ [kg m^{-3}]	3200	2260
Heat capacity, C_p [J kg^{-1} K^{-1}]	1414	1820
Thermal conductivity, λ [W m^{-1} K^{-1}]	1.33*	0.48
Latent heat of PCM, L (J g^{-1})	-	174
Solidus temperature, T_{sol} [K]	-	579
Melting temperature, T_m [K]	-	580
Permeability, K [m^2]	10^{-8}	-
Porosity, ε	0.5	-
Maximum mass content of hydrogen in the metal, wt [%]	3.6	-
Molar enthalpy of reaction, ΔH [J mol^{-1}]	-64000	-
Absorption plateau pressure coefficient, A_{abs}	26.481	-
Desorption plateau pressure coefficient, A_{des}	26.181	-
Absorption plateau pressure coefficient, B_{abs} [K]	7552.5	-
Desorption plateau pressure coefficient, B_{des} [K]	7552.5	-
Absorption rate constant, C_{abs} [s^{-1}]	175.31	-
Desorption rate constant, C_{des} [s^{-1}]	5452.3	-
Activation energy for absorption, E_{abs} [J mol^{-1}]	52205	-
Activation energy for desorption, E_{des} [J mol^{-1}]	63468	-
* This value is the effective thermal conductivity of Mg_2Ni with aluminum foam [50]		

2.2.3 Numerical Model

Figure 2.1(a,b) shows the 3D computational domain of the MH-PCM system for both cases. Due to the axisymmetric nature of this particular design, only 1/8th portion of the computational domain is simulated. The following assumptions were made:

- Local thermal equilibrium is valid [51,59,60].
- Constant thermophysical properties [51,54,59].
- The thermal capacity and thermal resistance of the interfaces of the MH-PCM system. are negligible relative to those of the external walls [48,51].
- The effect of the flow of hydrogen is negligible [51,61].
- The hydrogen pressure during the reaction is uniform [51,61,62].
- Radiative heat transfer is neglected [51,61].
- The convection heat transfer within the PCM domain can be neglected because the liquid PCM is assumed to be highly viscous [48,51,63].
- The effect of expansion and contraction during the phase transition is negligible [42,49,52,54].

2.2.3.1 Mathematical model of the Mg_2Ni hydride reactor

Energy balance

Due to the thermal equilibrium between the MH reactor and hydrogen, the temperature of the system can be computed by the following heat balance equation [50,61]:

$$(\rho \cdot C_P)_{eff} \frac{\partial T}{\partial t} = \nabla \cdot \left(\lambda_{eff} \cdot \nabla(T)\right) + S \qquad (2.1)$$

where $(\rho \cdot C_P)_{eff}$ is the effective heat capacity and λ_{eff} represents the effective thermal conductivity, which can be estimated by the following relations [50]:

$$(\rho \cdot C_P)_{eff} = \varepsilon \cdot \rho_{H_2} \cdot C_{P_{H_2}} + (1-\varepsilon) \cdot \rho_{MH} \cdot C_{P_{MH}} \quad (2.2)$$

$$\lambda_{eff} = \varepsilon \cdot \lambda_{H_2} + (1-\varepsilon) \cdot \lambda_{MH} \quad (2.3)$$

where ε , ρ, C_P, T and λ are respectively the porosity, the density, the heat capacity, the temperature, and the thermal conductivity.

The term *S* in Eq. (2.1) is the source term [61]. This is related to the reaction rate and can be assessed as follows:

$$S = \frac{\rho_{MH} \cdot wt \cdot (1-\varepsilon) \cdot \Delta H_{mol}}{M_{H_2}} \left(\frac{\partial X_{H_2}}{\partial t} \right) \quad (2.4)$$

where M_{H_2} = 0.002 kg mol^{-1} is the molecular mass of hydrogen, ΔH_{mol} the molar enthalpy of reaction, $\frac{\partial X_{H_2}}{\partial t}$ the kinetic reaction, and wt the maximum mass content of hydrogen that can be absorbed by the Mg_2Ni alloy.

Mass balance

The effect of the flow of hydrogen is neglected to simplify the computational simulation and avoid the momentum equations by meeting the conditions below [50,61]:

- Conductive heat transfer inside the MH reactor is significantly greater than the convective and radiation heat transfer.
- Required sensible energy to change the temperature inside the MH reactor is negligible when compared to the enthalpy of the reaction.
- The variation between the equilibrium and hydrogen pressure induced by the flow of hydrogen has no effect on the reaction velocity.

Chaise et al. [61] derived a dimensionless criterion *N* which allows to determine the validity of neglecting the effect of the flow of hydrogen. They concluded that the effect of the flow of hydrogen can be neglected in the simulation of reaction as long as *N* is lower than 0.1 approximately. *N* is expressed as:

$$N = \frac{\lambda \cdot M \cdot L_g^2 \cdot \mu}{P_{eq} \cdot \left(\frac{\Delta H_{mol}^2}{R_g \cdot T^2}\right) \cdot \rho_g \cdot K \cdot L_{heat}^2} \tag{2.5}$$

where L_g = 0.1 m the typical gas diffusion length, L_{heat} = 0.02 m typical heat diffusion length, μ = 8.9×10^{-6} Pa·s the dynamic viscosity of hydrogen, K = 10^{-8} m^2 the permeability, and ρ_g = 0.32 kg·m^{-3} the hydrogen density at 7.7 bar and 600 K.

In this study, the calculation shows that N = 1.75×10^{-7} which is less than 0.1 and that demonstrates the validity of neglecting the effect of the flow of hydrogen in the simulation.

Kinetic reaction

The kinetic reaction of Mg_2Ni hydride for the hydrogenation/dehydrogenation process takes the following general form [50]:

$$\frac{\partial X_{H_2}}{\partial t} = \begin{cases} C_{abs}\, exp\left(-\frac{E_{abs}}{R_g\, T}\right)\left(\frac{P_{H_2} - P_{eq,abs}}{P_{eq,abs}}\right)\left(X_{H_2,max} - X_{H_2}\right) & ,for\ P_{H_2} > P_{eq,abs} \\ C_{des}\, exp\left(-\frac{E_{des}}{R_g\, T}\right)\left(\frac{P_{H_2} - P_{eq,des}}{P_{eq,des}}\right) X_{H_2} & ,for\ P_{H_2} < P_{eq,des} \end{cases} \tag{2.6}$$

where C is the absorption/desorption rate constant, E the activation energy for absorption/desorption, $X_{H_2,max}$ the maximum absorbable hydrogen amount in weight fraction (*wt%*), P_{H_2} the hydrogen pressure, and R_g= 8.314 J K^{-1} mol^{-1} the universal gas constant.

The absorption/desorption equilibrium pressure P_{eq} is estimated by the Van't Hoff relation and defined as a function of temperature [59]:

$$\frac{P_{eq}}{P_{ref}} = \begin{cases} 10^{-5} \cdot exp\left(A_{abs} - \frac{B_{abs}}{T}\right) \\ 10^{-5} \cdot exp\left(A_{des} - \frac{B_{des}}{T}\right) \end{cases} \quad (2.7)$$

where P_{ref} is 1 bar [59], and the A and B coefficients represent the plateau pressure for absorption and desorption as presented in Table 2.3.

2.2.3.2 Mathematical model of the PCM

The phase-change process can be modeled using the formulation of enthalpy-porosity [42,50]. In this approach, every computational cell is given a liquid fraction according to its enthalpy balance. The thermal energy equation is described as:

$$\frac{\partial}{\partial t}(\rho_{PCM} H_{PCM}) = \nabla(\lambda_{PCM} \nabla T_{PCM}) \quad (2.8)$$

where H_{PCM} is the total enthalpy which is a combination of the latent heat and sensible enthalpy of the PCM as given below:

$$H_{PCM} = h_{sen} + (f \cdot L_{PCM}) \quad (2.9)$$

where h_{sen}, f and L_{PCM} are respectively the sensible enthalpy, the liquid fraction, and latent heat of the PCM.

The sensible enthalpy is assessed as follows:

$$h_{sen} = \int_{T_m}^{T} C_{p,PCM} dT_{PCM} \quad (2.10)$$

where $C_{p,PCM}$ is the heat capacity of the PCM.

The latent heat content of the PCM (fL_{PCM}) can vary from zero (solid phase of PCM) to the value L_{PCM} (liquid phase of PCM). Therefore, the liquid fraction f can be calculated via [50]:

$$f = \begin{cases} 0 & T \leq T_{sol} \\ \dfrac{T - T_{sol}}{T_m - T_{sol}} & T_{sol} < T < T_m \\ 1 & T \geq T_m \end{cases} \tag{2.11}$$

where T_{sol} and T_m are the PCM temperature of the solid and liquid phases, respectively.

The required volume of the PCM jacket and PCM sandwich bed was calculated by assuming the heat released from the MH reactor can be stored in the PCM [50]:

$$V_{PCM} = \frac{V_{MH} \cdot wt \cdot \Delta H_{mol} \cdot \rho_{MH} \cdot (1 - \varepsilon)}{M_{H_2} \cdot \rho_{PCM} \cdot L_{PCM}} \tag{2.12}$$

Because the effect of the sensible enthalpy is negligible relative to other terms, it is not included in the calculation of the required amount of PCM.

2.2.3.3 Initial and boundary conditions

Initial conditions

- For hydrogenation:

$$T_0 = 579\ K \tag{2.13}$$

$$P_0 = 12\ bar \tag{2.14}$$

- For dehydrogenation:

$$T_0 = 580\ K \tag{2.15}$$

$$P_0 = 3\ bar \tag{2.16}$$

Boundary conditions

The geometrical boundaries of the system domain are shown in Figure 2.1(a,b) and can be expressed as:

- The boundary condition at symmetric and adiabatic walls is

$$\nabla T_{MH} \cdot \vec{n} = \nabla T_{PCM} \cdot \vec{n} = 0 \tag{2.17}$$

- The boundary condition at the interface between the MH reactor and the PCM is

$$\lambda_{MH} \nabla T_{MH} \cdot \vec{n} = \lambda_{PCM} \nabla T_{PCM} \cdot \vec{n} \tag{2.18}$$

where $\vec{n}$ represents the normal vector to the corresponding wall. This interface is defined as a coupled wall to allow conjugate heat transfer [30].

2.2.3.4 Numerical method and model validation

ANSYS Fluent 19.2 software is used to solve the set of coupled partial differential governing equations. User-defined functions are written to solve the source term in the energy equation (Eq. (2.1)), the kinetic reaction rate (Eq. (2.6)), and the equilibrium pressure equations (Eq. (2.7)).

The present model was previously used in previous studies conducted by the co-author Mellouli [50,51]. Mellouli et al. [50] previously validated this model with experimental data reported by Garrier et al. [47] in which an Mg-PCM storage system was studied. Here,

the same model is applied for an Mg_2Ni-PCM storage system for which experimental data are not available in the literature.

2.3 Results and Discussion

2.3.1 Volume Distribution of the PCM in the New Design

Considering the objective to increase the heat transfer rate between the MH reactor and the PCM, it is necessary to determine the optimal volume distribution of the PCM between the inner and outer beds in the new design (*case 2*) in order to be adopted for comparison with the conventional design (*case 1*).

Therefore, a parametric study is conducted to evaluate the effect of the PCM volume distribution on the performance of the MH system. Figure 2.3 shows the time-duration of the hydrogenation and dehydrogenation processes as a function of the ratio of the inner PCM bed volume to the total PCM volume ($V_{inner\text{-}PCM} / V_{tot\text{-}PCM}$). As can be seen in Figure 2.3, the 50% volume distribution of the PCM achieves the shortest hydrogenation and dehydrogenation times. Thus, the PCM volume is distributed evenly between the inner and outer beds in the new design.

In the following sections, a detailed analysis of the impact of the design on the temperature, hydrogen-reacted fraction and the PCM's liquid fraction for both the hydrogenation and dehydrogenation processes is performed, and the best design for the augmentation of thermal exchange is identified.

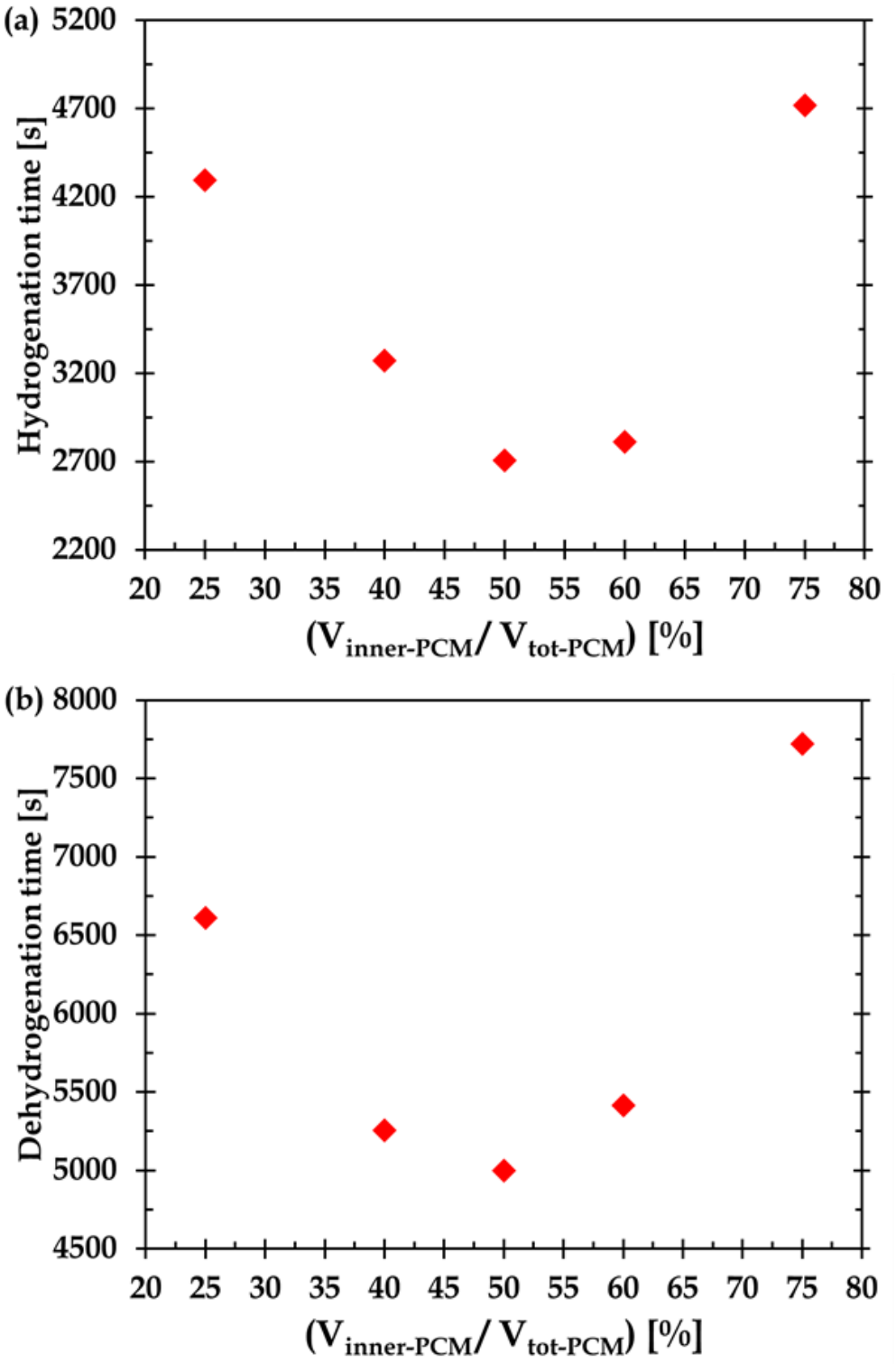

Figure 2.3: The Time-duration of the (a) Hydrogenation and (b) Dehydrogenation Processes as a Function of the Ratio of the Inner PCM Bed Volume to the Total PCM Volume.

2.3.2 Hydrogenation Process

Considering the objective to recover the heat of reaction from the MH reactor, a detailed comparison of the MH reaction and the PCM's liquification times is carried out. Comparison trends are performed for both cases to investigate the impact of the design on the performance of the MH-PCM system.

The time evolution of the hydrogen-reacted fraction of the MH reactor and the PCM's liquid fraction throughout the hydrogenation process for both cases is presented in Figure 2.4. As shown in Figure 2.4(a), the MH reactor in the conventional design (*case 1*) reaches saturation at 14600 seconds whereas it reaches saturation at 2700 seconds for the new design (*case 2*). This indicates an 81.5% improvement in hydrogenation time which is attributed to the increase in heat transfer area. Hence, the new design offers a better thermal exchange between the MH reactor and the PCM.

In Figure 2.4(b), the PCM's liquid fraction for each case shows a good correspondence to the hydrogen-reacted fraction throughout the hydrogenation process. At the end of the hydrogenation process in *case 2*, it can be noted that the outer PCM bed is fully melted while the inner PCM bed is partially melted even though both beds have an equivalent amount of PCM. This is due to the fact that the surface area of the interface between the MH reactor and the outer PCM bed is larger than that with the inner PCM bed.

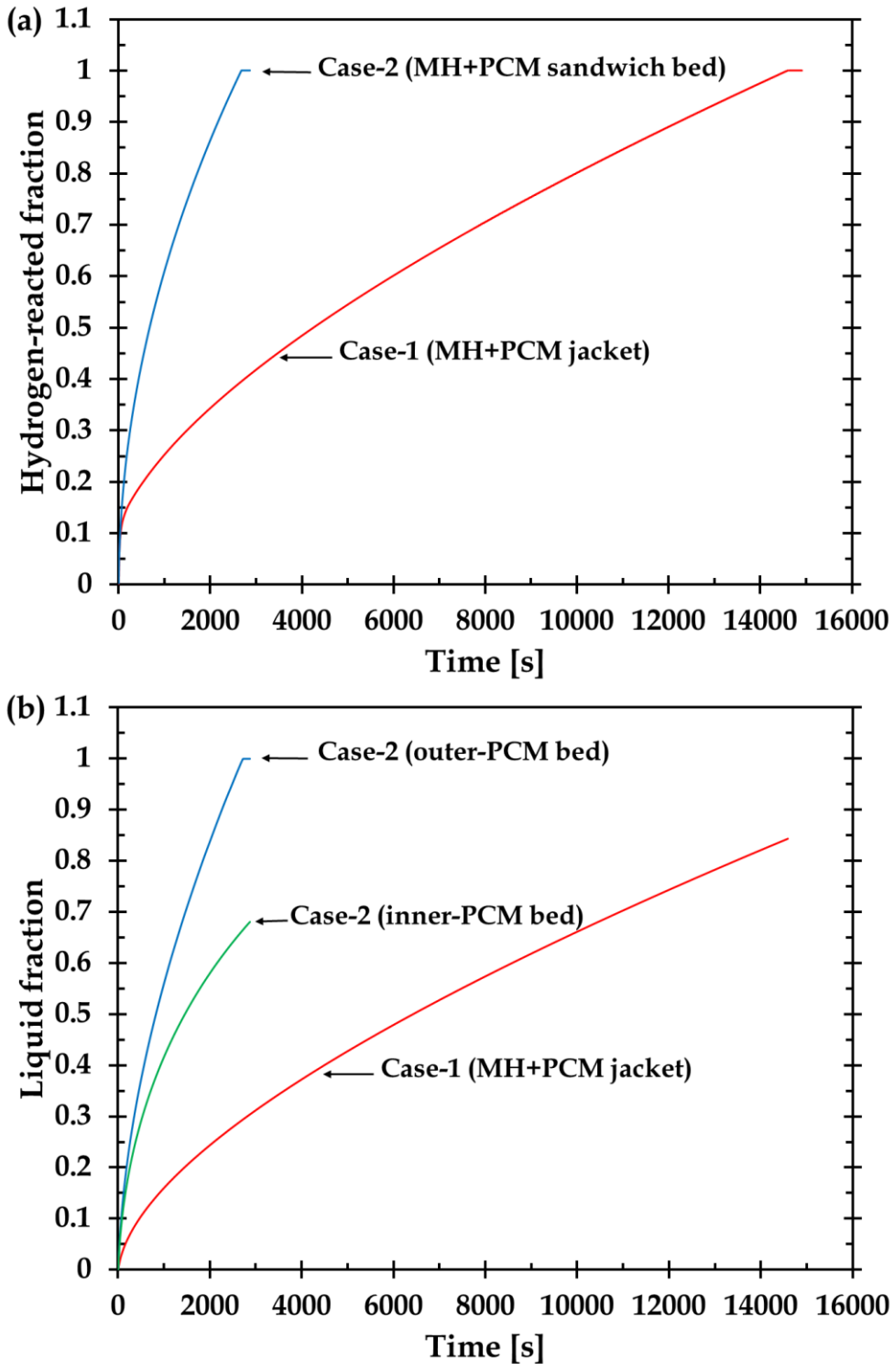

Figure 2.4: Comparison of the Time Evolution of (a) Hydrogen-reacted Fraction and (b) the PCM's Liquid Fraction Throughout the Hydrogenation Process Between Case 1 and Case 2.

For *case 1*, Figure 2.5(a) depicts the average temperature of the MH reactor and the PCM jacket throughout the hydrogenation process. At the initial stage of the hydrogenation process, the average temperature of the MH reactor increases rapidly due to the increase in reaction rate term to its peak in the source equation (Eq. (2.4)). This is interconnected with the fact that the rate of reaction reaches its maximum value when the difference between the hydrogen pressure and MH equilibrium pressure is highest, which occurs at the beginning of the exothermic reaction (see Eq. (2.7) and Eq. (2.14)). Therefore, the source term in the energy equation (Eq. (2.1)) results in a rapid increase in the average temperature of the MH reactor as it is a function of reaction rate. Once the heat starts to transfer from the MH reactor to the PCM jacket, the temperature of the MH reactor then decreases. In *case 2*, however, Figure 2.5(b) indicates that the rapid increase in the average temperature of the MH reactor is lower compared to that in *case 1*. This reduction is due to the fact that the rate of heat transfer in *case 2* is higher because of the increase in heat transfer area.

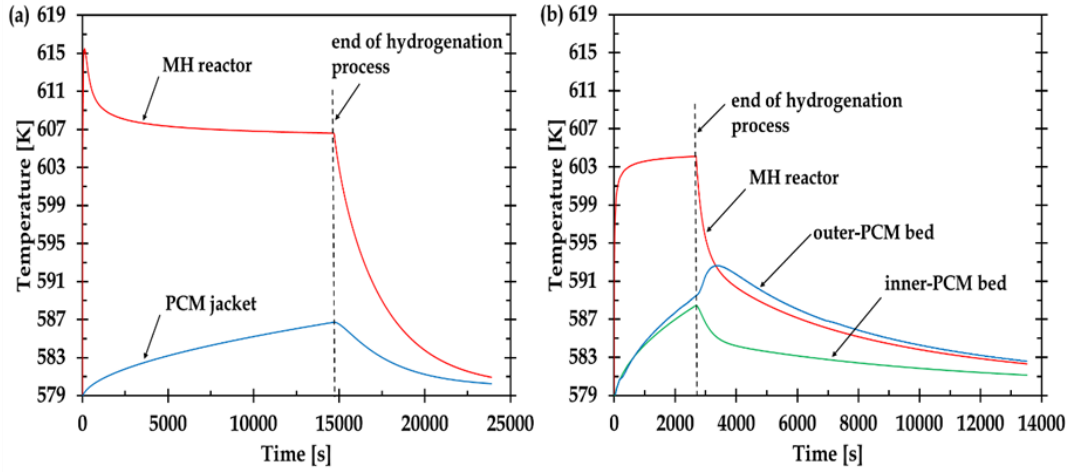

Figure 2.5: Time Evolution of the Average Temperature of (a) the MH-PCM Jacket Bed (*case 1*) and (b) the MH-PCM Sandwich Bed (*case 2*) Throughout the Hydrogenation Process.

At the end of the hydrogenation process, for both cases, a dramatic decrease in the average temperatures of the MH reactors is observed until a thermal equilibrium state is reached as annotated in Figure 2.5(a,b). This is interconnected with the fact that when the heat of reaction stops at the end of the hydrogenation process, there is no more heat generated in the MH reactor to compensate for the heat transfer to the PCM and that explains the rapid decrease in the average temperature of the MH reactor.

With regard to the average PCM temperature in both cases, it can be observed that it reaches its maximum at the end of the hydrogenation process when the PCM is partially melted as shown in Figure 2.5(a) for the PCM jacket in *case 1* and in Figure 2.5(b) for the inner PCM bed in *case 2*. Then, a gradual decrease in the average PCM temperatures is observed until a thermal equilibrium state is reached. This may be explained as follows: when the hydrogenation process ends, a portion of the PCM is not melted. As a result, heat flows from the PCM liquid phase to the solid phase causing a decrease in the average temperature of the PCM.

On the contrary, the average temperature of the outer PCM bed shows a different behavior. It can be seen in Figure 2.5(b) that it keeps increasing after the end of the hydrogenation process until it intersects with the MH average temperature trend. This is because at the end of the hydrogenation process, the outer PCM is fully melted and its thermal exchange with the MH reactor is only via a sensible heat mechanism.

To clarify this behavior in more detail, the time evolution of local temperature at various locations inside the domains is reported in Figure 2.6(b) throughout the hydrogenation

process. As can be seen in Figure 2.6(a), nine points are set in the radial direction starting from the core of the inner PCM bed (*point 1*) to the far edge of the outer PCM bed (*point 9*). As shown in Figure 2.6(b), the local temperatures at points 3 through 7 (T_{P3}, T_{P4}, T_{P5}, T_{P6}, *and* T_{P7}) are identical shortly after the end of the hydrogenation process. At this moment, these local temperatures have the highest values within the domains which consequently exchange heat with the outer and the inner PCM domains. However, the thermal exchange between the MH and the outer PCM domains is controlled by the sensible heat mechanism since the PCM is fully melted. This explains the rapid increase of T_{P8} and T_{P9} until they intersect with the five neighboring points mentioned before (at 3400 seconds) as shown in Figure 2.6(c). In the meantime, the inner PCM domain is not fully melted, and therefore T_{P1} and T_{P2} have the lowest values within the domains which cause the heat to be transferred from the MH domain to the inner PCM domain. As a result, the temperature of the MH domain becomes lower relative to the outer PCM domain. This explains the intersection between the local temperature trends of the MH and the outer PCM. In other words, at a time when the MH and the outer PCM domains have identical temperatures, the inner PCM domain temperature is the lowest and consequently the heat transfer is directed from the outer PCM domain (hotter domain) to the MH domain and then to the inner PCM domain (cooler domain). This explains why the temperature (local or average) of the outer PCM domain becomes slightly higher than the temperature (local or average) of the MH domain at t=3600 seconds until the equilibrium condition is reached.

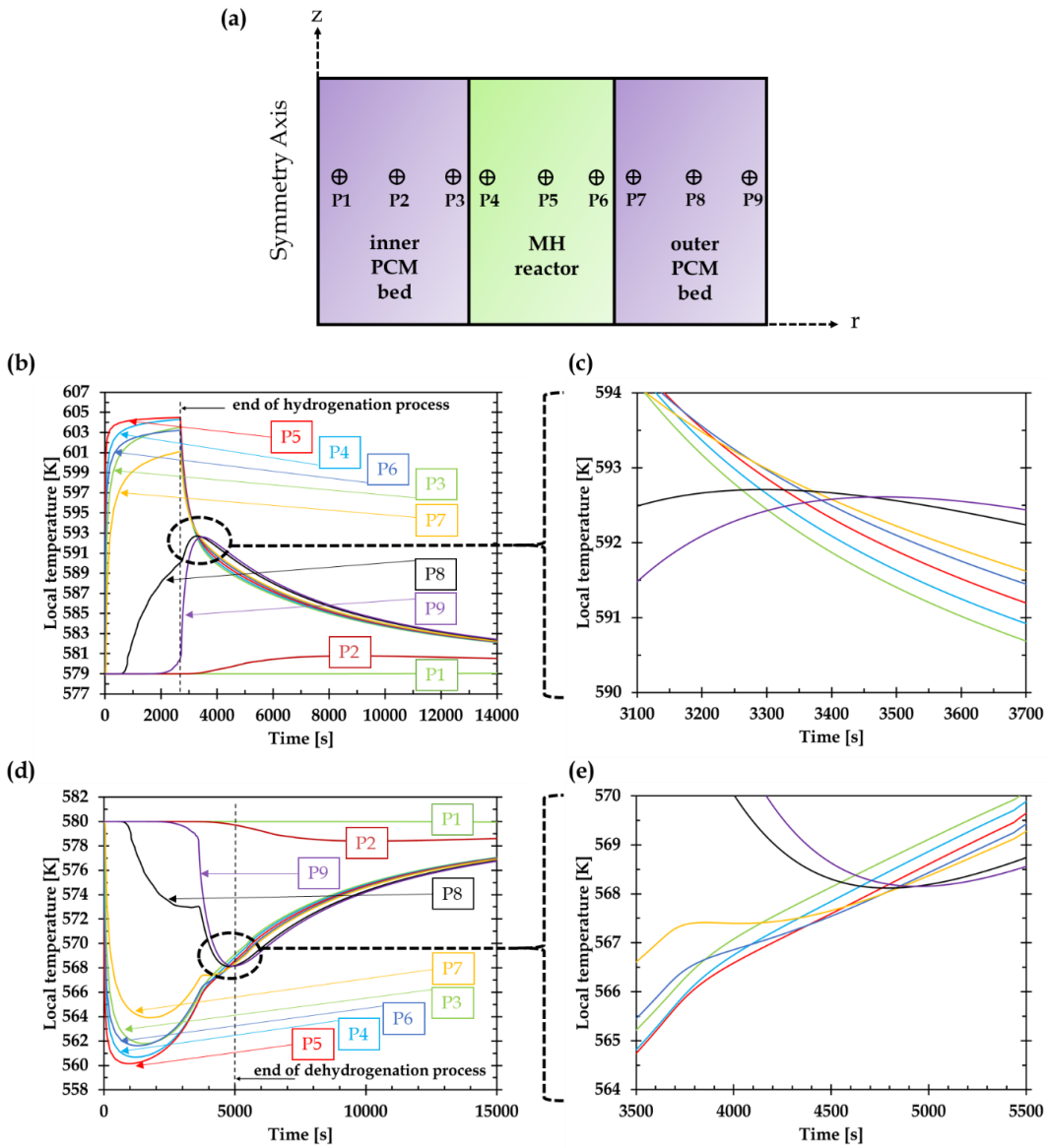

Figure 2.6: (a) Distribution of Local Points within the Domains and the Time Evolution of the Local Temperatures Throughout (b) Hydrogenation, (c) Hydrogenation Between 3100 and 3700s, (d) Dehydrogenation, and (e) Dehydrogenation Between 3500 and 5500s.

Figure 2.7 depicts the temperature distribution of the MH-PCM system and the PCM domain liquid fraction at selected times throughout the hydrogenation process for *case 1*. In the early stage of the hydrogenation process, the PCM temperature at the interface with the MH reactor starts to increase and subsequently the PCM starts to transform from the

solid phase to the liquid phase. Once the MH reactor reaches the saturation state (t=14600s), it can be observed that only a small portion of PCM is not melted. This proves that the PCM amount is adequate to store all the heat released from the MH reactor during the hydrogenation process.

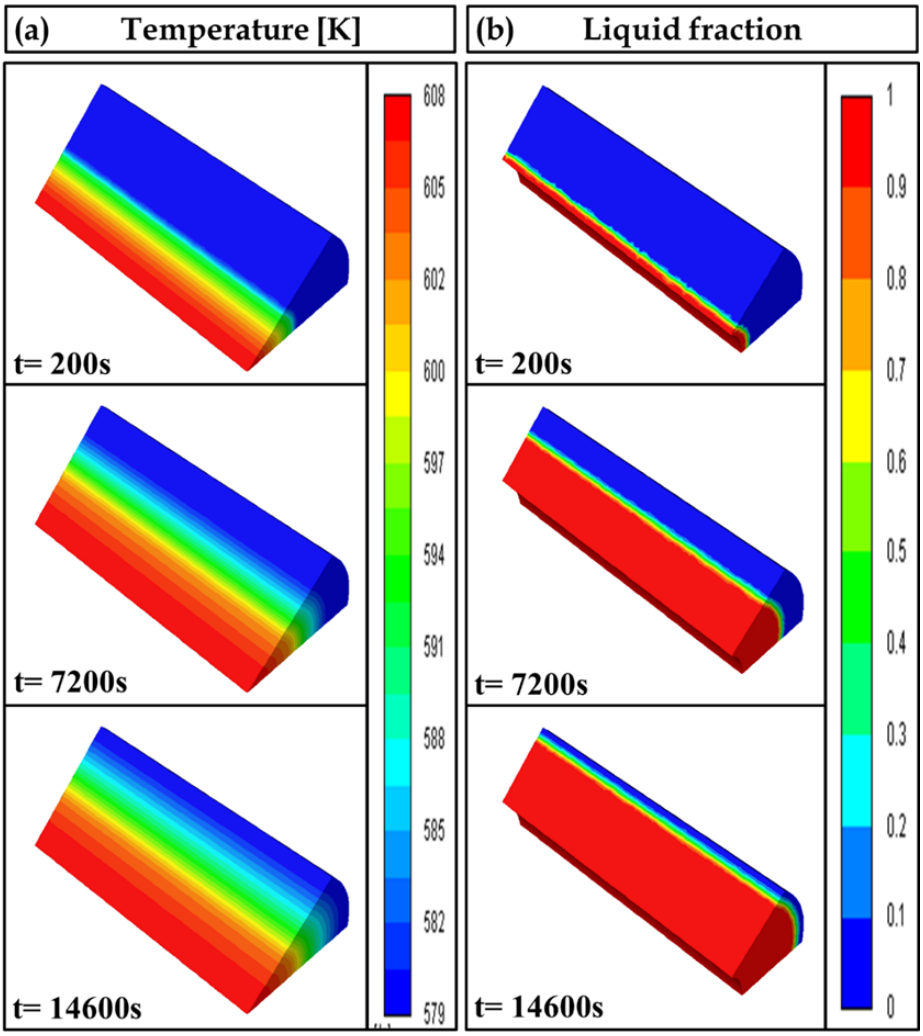

Figure 2.7: Time Distribution of (a) the Temperature of the MH-PCM System and (b) the PCM Domain's Liquid Fraction at Selected Times Throughout the Hydrogenation Process for Case 1.

The temperature distribution of the MH-PCM system and the PCM domain's liquid fraction at selected times throughout the hydrogenation process for *case 2* are presented in

Figure 2.8. Unlike *case 1*, the heat of reaction transfers from the MH reactor to the PCM sandwich bed via two interfaces which contributes to an increase in the rate of heat transfer. As can be observed, the new design (*case 2*) increases the rate of heat extraction from the MH reactor and therefore reduces the time of the hydrogenation process (t=2700s) compared to the design of *case 1*.

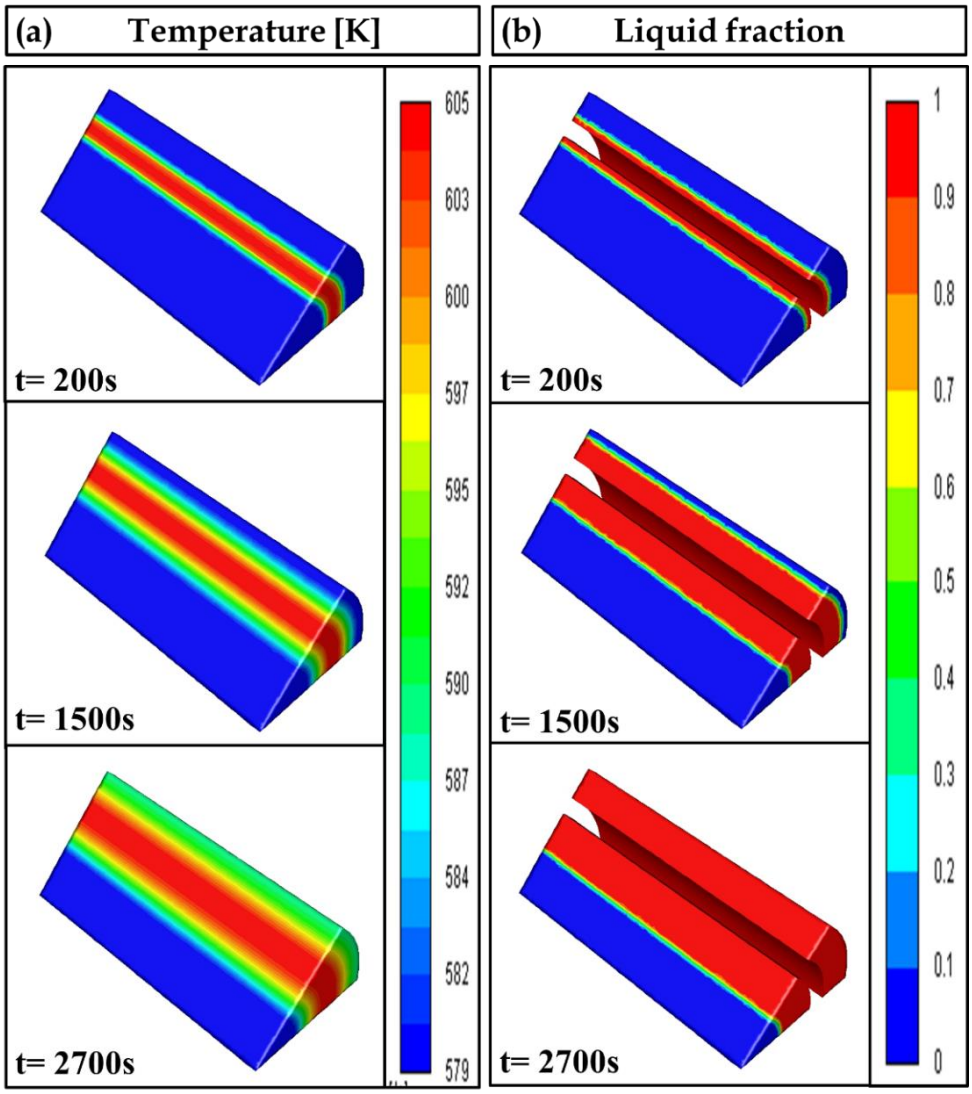

Figure 2.8: Time Distribution of (a) the Temperature of the MH-PCM System and (b) the PCM Domain Liquid Fraction at Selected Times Throughout the Hydrogenation Process for Case 2.

2.3.3 Dehydrogenation Process

To compare between *case 1* and *case 2* throughout the dehydrogenation process, Figure 2.9(a,b) show the time durations of the dehydrogenation and PCM solidification processes for both cases, respectively. From Figure 2.9(a), it can be seen that the dehydrogenation process is completed at 5000 seconds in the new design (*case 2*) compared to 18500 seconds in the conventional design (*case 1*). This represents a 73% enhancement in the dehydrogenation time. This implies that the PCM sandwich-bed design may offer a huge advantage in the performance of the MH-PCM system.

The PCM's liquid fraction trend mostly matches the dehydrogenation trend as illustrated in Figure 2.9(b). Furthermore, at the end of the dehydrogenation process in *case 2*, the outer PCM bed is fully solidified while the inner PCM bed is only partially solidified. As explained earlier, this is because the interface of the MH reactor and the outer PCM is larger than that with the inner PCM bed.

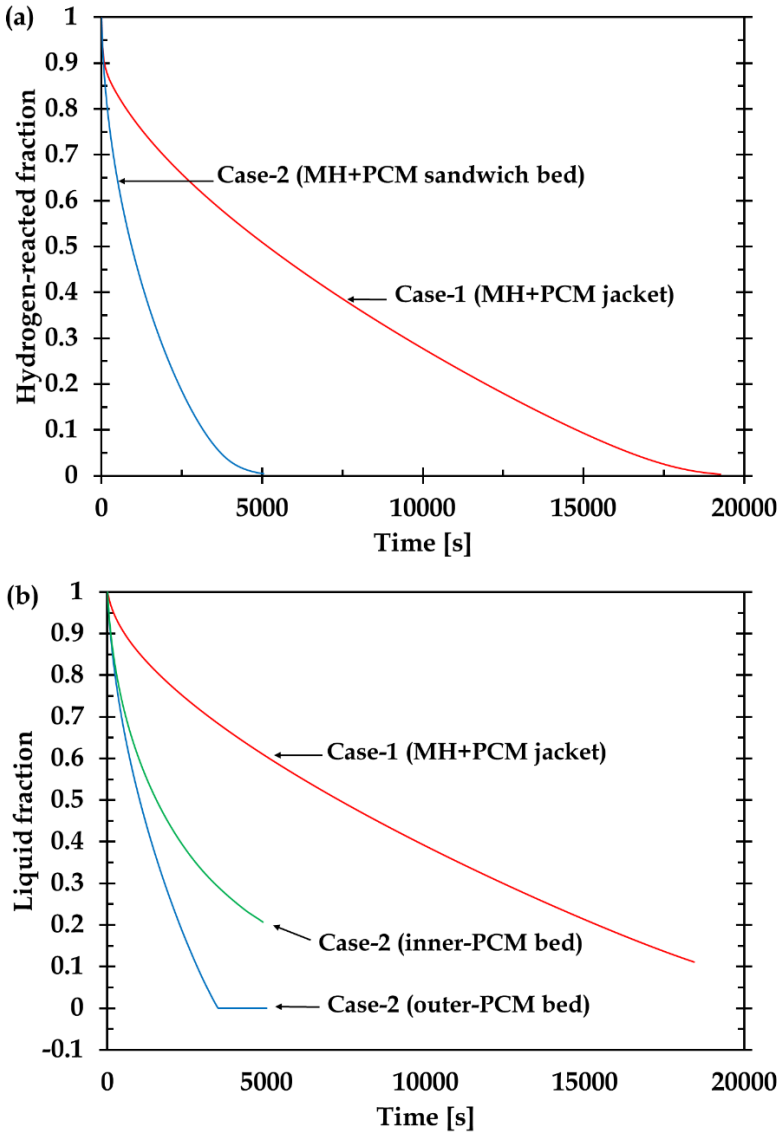

Figure 2.9: Comparison of the Time Evolution of (a) Hydrogen-reacted Fraction and (b) the PCM's Liquid Fraction Throughout the Dehydrogenation Process Between Case 1 and Case 2.

Figure 2.10(a) illustrates the average temperature of the MH reactor and PCM jacket as a function of time for *case 1* throughout the dehydrogenation process. A rapid decrease in the average temperature of the MH reactor is observed at the initial stage of the dehydrogenation reaction ($t \cong 200$s). As the reaction continues, the average temperature of the MH reactor increases gradually. The dehydrogenation process is sustained by the heat

released by the PCM solidification, which experiences a decline in average temperature as shown in Figure 2.10(a). For *case 2*, the temperature drop in the MH reactor at the initial time of the dehydrogenation process was relatively lower than that in *case 1* as shown in Figure 2.10(b). This might be attributed to the increase in heat transfer area with the PCM as discussed earlier.

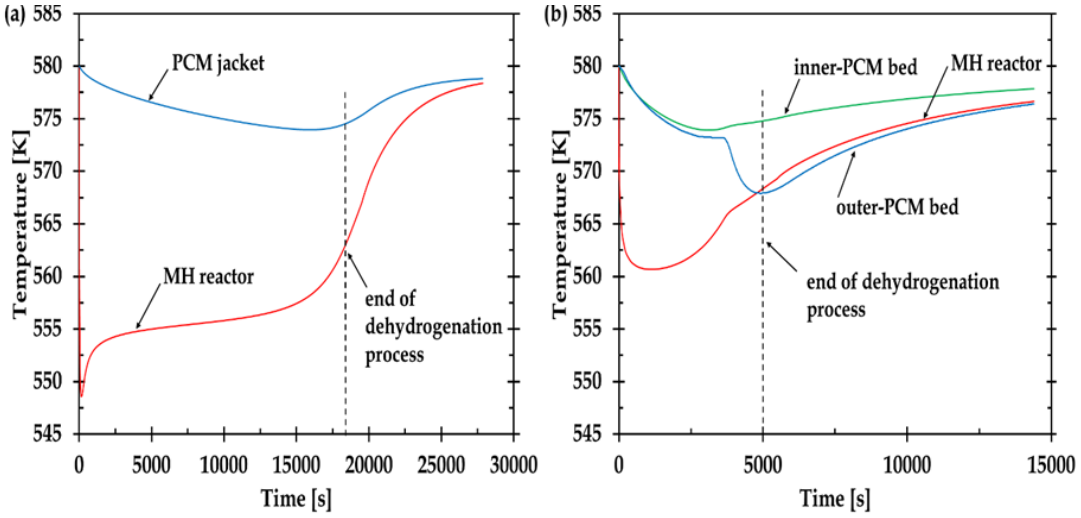

Figure 2.10: Time Evolution of the Average Temperature of (a) MH-PCM Jacket Bed (*case 1*) and (b) MH-PCM Sandwich Bed (*case 2*) Throughout the Dehydrogenation Process.

For both cases, by the end of the dehydrogenation process, the average temperatures of the MH reactor and the PCM increase gradually until a thermal equilibrium state is achieved as annotated in Figure 2.10(a,b).

Because the outer PCM bed is fully solidified before the end of dehydrogenation process in *case 2*, a dramatic decrease in the average temperature of the outer PCM bed is observed until it intersects with the MH average temperature trend as shown in Figure 2.10(b). This decrease is a result of the thermal exchange between the outer PCM bed and the MH rector in the form of sensible heat which takes place at the end of the solidification process.

To clarify this behavior in more detail, the time evolution of local temperature at various locations inside the domains is reported in Figure 2.6(d) throughout the dehydrogenation process. As soon as the outer PCM bed is fully solidified ($t \cong 3640$s), the thermal exchange between the MH and the outer PCM domains takes place only in the form of sensible heat and this explains the dramatic decrease in T_{P8} and T_{P9} until they intersect (at $t \cong 5000$s) with the temperatures of point 3 through point 7 as shown in Figure 2.6(e). After that, the temperature profiles of both the MH and the outer PCM domains are increasing where the temperatures of the MH domain (T_{P4}, T_{P5}, *and* T_{P6}) become relatively higher than those of the outer PCM domain (T_{P7}, T_{P8}, *and* T_{P9}). To explain this, it is important to note that the inner PCM domain is the source of heat since it is not fully solidified. This generated heat is directed first to the MH domain and then to the outer PCM domain which is relatively cooler. This illustrates why the temperature (local or average) of the MH domain becomes slightly higher than the temperature (local or average) of the outer PCM domain after t=5000 seconds until the equilibrium condition is reached.

For *case 1*, the temperature distribution of the MH-PCM system and the PCM domain's liquid fraction throughout the dehydrogenation process at selected times are shown in Figure 2.11. A rapid decrease in the MH temperature was observed at the initial stage of the dehydrogenation process due to the higher rate of endothermic reaction. This caused a high solidification rate in the PCM near the MH-PCM interface. As the reaction progressed, the solid fraction in the PCM increased, suppling heat energy to the MH reactor to sustain the dehydrogenation process. By the end of the dehydrogenation process (t=18500s), almost 88% of the PCM became solid.

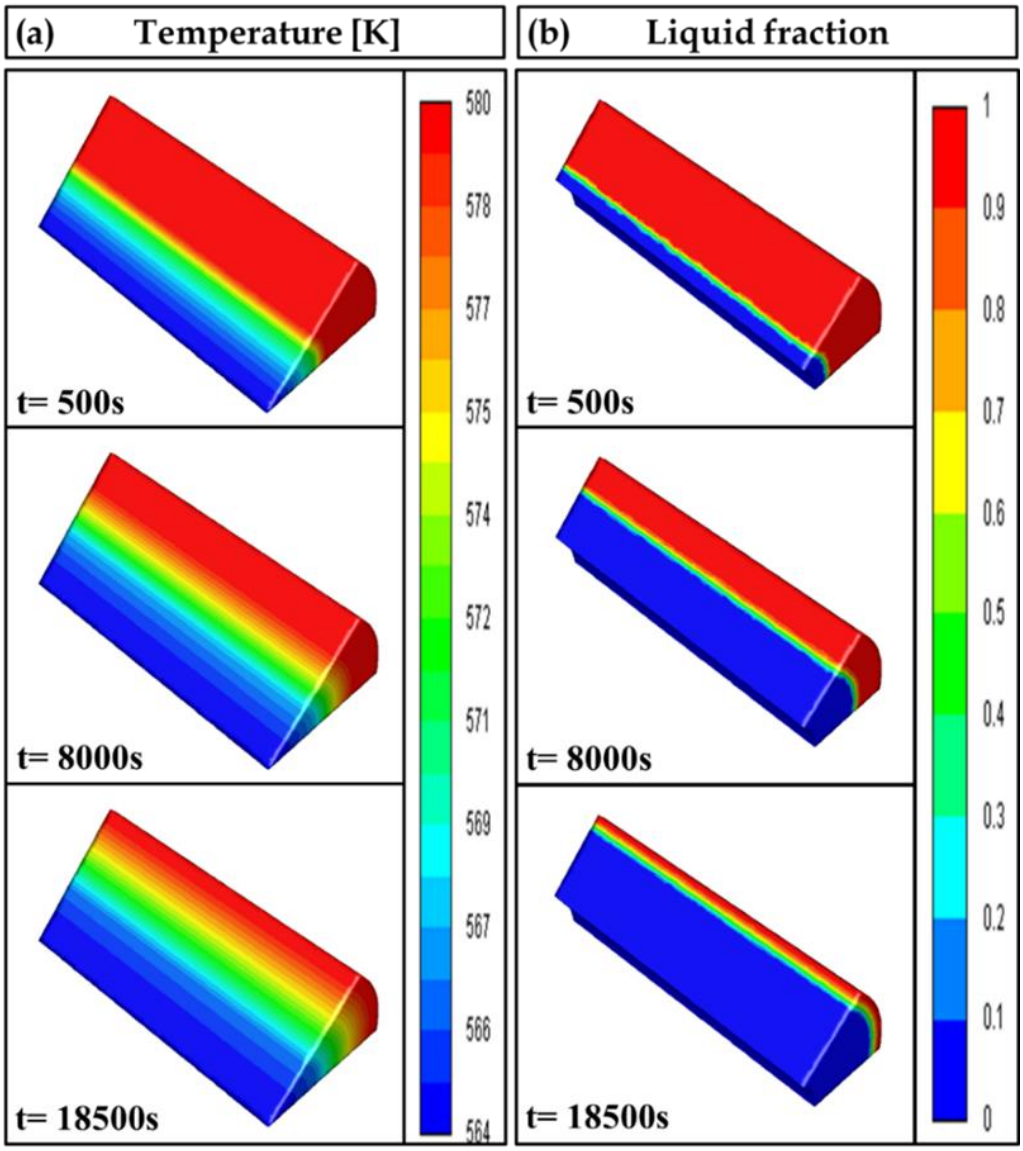

Figure 2.11: Time Distribution of (a) the Temperature of the MH-PCM System and (b) the PCM Domain's Liquid Fraction at Selected Times Throughout the Dehydrogenation Process for Case 1.

Figure 2.12 shows the temperature distribution of the MH-PCM and the PCM domain's liquid fraction in *case 2* at selected times throughout the dehydrogenation process. It is clear that the PCM sandwich bed design significantly enhances the heat transfer rate, as most of the PCM solidified in ~5000 seconds compared to 18500 seconds in *case 1*, resulting in faster dehydrogenation in the MH reactor. In other words, the dehydrogenation

process was more efficient because heat was transferred through two interfaces instead of one.

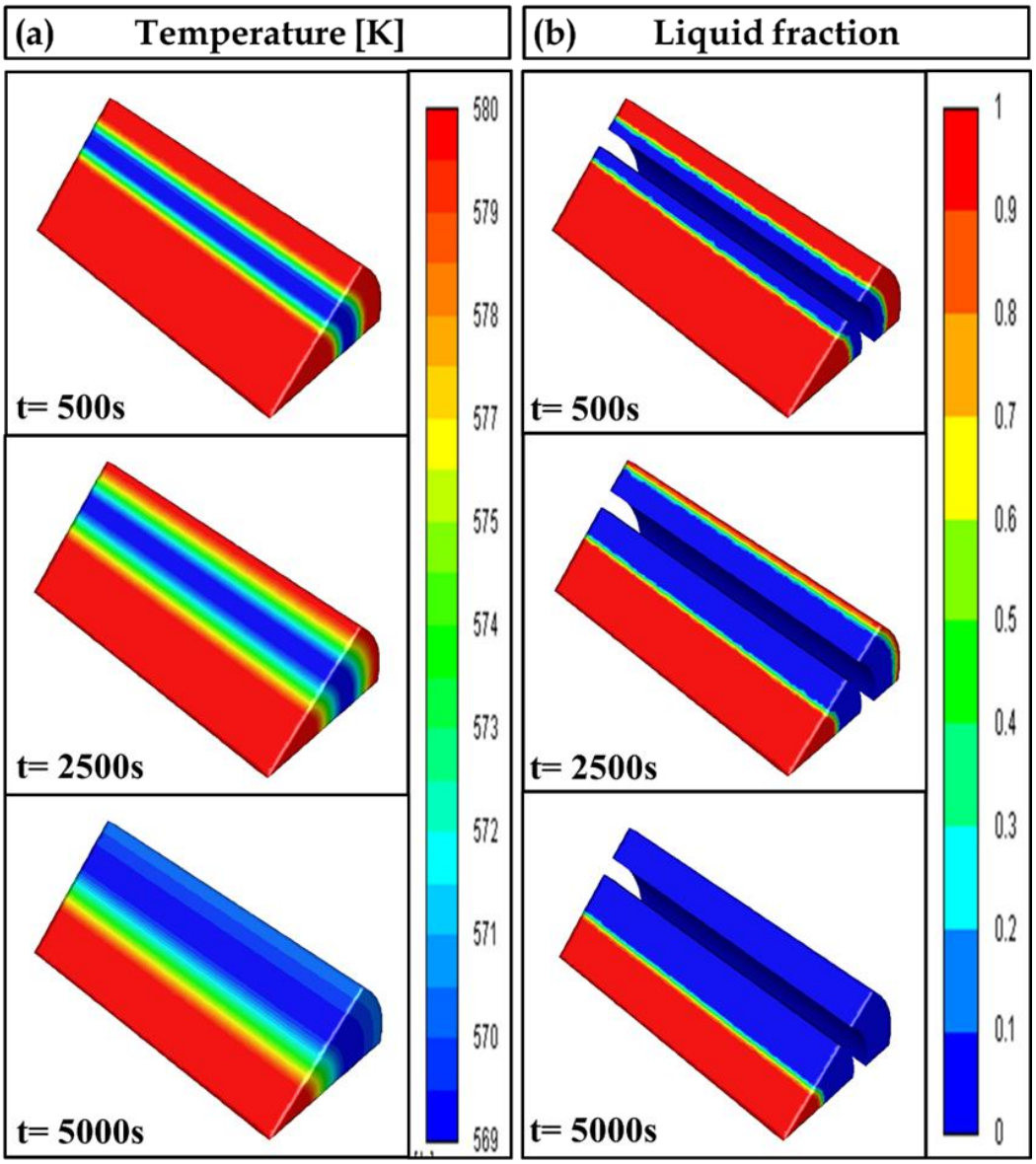

Figure 2.12: Time Distribution of (a) the Temperature of the MH-PCM System and (b) the PCM Domain's Liquid Fraction at Selected Times Throughout the Dehydrogenation Process for Case 2.

2.3.4 Comparison of the Present Study's Design and the Previous Studies' Designs

As discussed earlier in the introduction section, Table 2.1 summarized the studies that integrated an MH reactor with PCM. From the table, it is challenging to compare between these studies' results since they are based on different metal hydrides, PCMs, designs, sizes and operating conditions. However, it may be useful to use the design as a criterion to perform a comparison study between the present and previous studies. As illustrated in Table 2.1, previous studies have adopted two PCM designs with a cylindrical MH reactor, namely PCM jacket bed and PCM pool bed. Figure 2.13 shows the time duration of the hydrogenation and dehydrogenation of the present design (MH+PCM sandwich bed) and that of previous designs (MH+PCM jacket bed and MH+PCM pool bed) using the same materials and volume of the MH (Mg_2Ni) and PCM ($NaNO_3$). It is apparent that the PCM sandwich bed design outperformed the previous designs. Therefore, the adoption of the proposed MH-PCM sandwich bed design should be taken into consideration in future work.

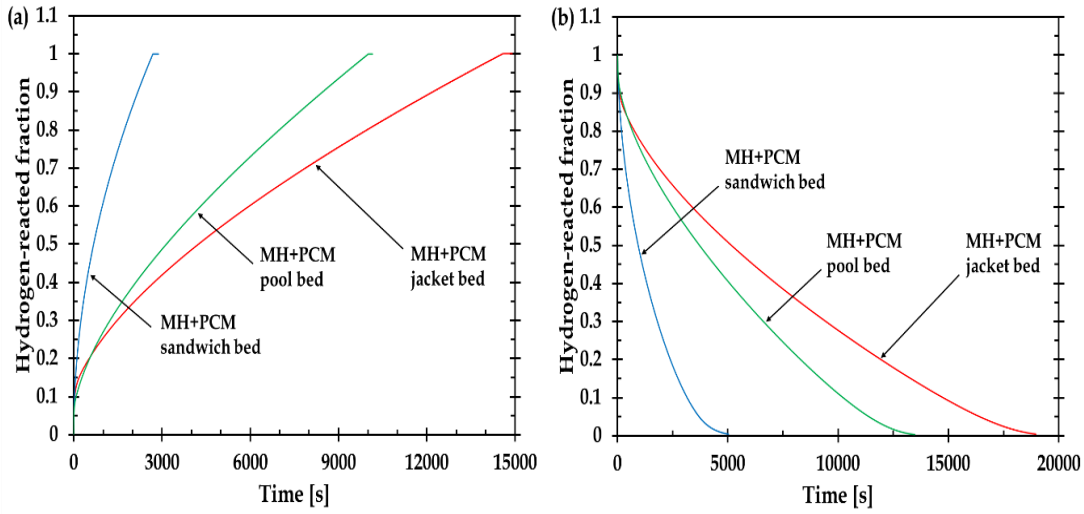

Figure 2.13: Comparison of the Time Evolution of Hydrogen-reacted Fraction Between the Present study's Design (*Sandwich Bed*) and Previous Studies' Designs (*Pool Bed and Jacket Bed*) Throughout the (a) Hydrogenation and (b) Dehydrogenation Processes.

2.4 Summary

The hydrogenation and dehydrogenation processes of a metal hydride (MH) reactor encircled by phase change material (PCM) were numerically investigated. A detailed analysis was performed to predict the time evolution of the MH-PCM system temperature, hydrogen-reacted fraction and liquid fraction. The heat transfer surface area between the MH and PCM was increased in the new design where the number of interfaces between the MH reactor and PCM was doubled by encircling the MH reactor with a cylindrical sandwich bed filled with PCM. The results showed that the time duration required for the hydrogenation and dehydrogenation processes was improved by 81.5% and 73%, respectively, for the new MH-PCM system design compared to a conventional MH-PCM system that includes only a single PCM bed.

3. METAL HYDRIDE REACTOR ENCIRCLED BY CASCADED PCM BEDS[2]

Metal hydride (MH) storage systems are considered as an attractive option and economically viable for many applications such as heating/cooling [64,65], fuel cells [20,21], concentrated solar power [24,25] and water pumping systems [27,28]. MH storage systems are characterized by their high volumetric energy storage density, high efficiency, good reversibility and safety advantages relative to other storage systems such as sensible and latent heat storage systems. In addition, MHs have an intrinsic capability of absorbing and releasing heat at relatively constant gas pressure [11].

3.1 Review of Literature

Thermal management of an MH storage system is essential for its optimum use, as its processes of hydrogenation/dehydrogenation are highly affected by the rate of extracted/supplied heat from/to the system [14,15,66]. As a result, abundant heat and mass transfer studies have emphasized the thermal management of MH storage systems and have proposed various methods in order to improve the rate of heat transfer. These methods include using a helical coil heat exchanger [38–40,67], embedding cooling tubes [29,33,34], adding fins to the cooling tubes [30,35,36], adding high conductive porous matrices [32], making MH powder compacts [19,37], and/or adding nanoparticles (e.g., graphite) [41]. These studies have demonstrated the effectiveness of their techniques in improving the rate of heat transfer throughout the hydrogenation and dehydrogenation

[2] Submitted for publication as:

***T. Alqahtani**, A. Bamasag, S. Mellouli, F. Askri, P.E. Phelan, Cyclic behaviors of a novel design of a metal hydride reactor encircled by cascaded phase change materials.*

processes. One major disadvantage of these investigations is that the extracted heat is released to the environment during the hydrogenation process, thus necessitating an external source to provide the required heat for the dehydrogenation process. Therefore, the required heat for the dehydrogenation process can also be considered as an essential factor for optimum utilization of an MH storage system since this heat is usually provided by an auxiliary heater which therefore leads to a reduction in the overall efficiency of the system.

Several researchers have suggested an elegant solution to store the generated heat throughout the hydrogenation process and reuse it in the subsequent dehydrogenation process [42,47–55]. This solution is essentially based on the integration of the MH storage system with a latent heat storage (LHS) system. The materials used for LHS are called phase change materials (PCMs). In fact, thermal regulation of an MH storage system using PCM is considered an attractive option because of its high volumetric energy storage density and its capability to store/release energy over a relatively narrow temperature range [1,44,68].

Table 2.1 summarizes the previous studies that integrated an MH storage system with a PCM (MH-PCM). Even though these studies are based on different metal hydrides, PCMs, designs, sizes and operating conditions, they agree that the integration of PCM with an MH reactor is an efficient way to operate the MH storage system. Recently, in chapter 2 [56], we proposed a new design of an MH-PCM storage system in which the MH reactor is encircled by a cylindrical sandwich bed packed with PCM. Also, a comparison study was performed to investigate the effect of the new design (MH+PCM sandwich bed) relative to

the previous designs (MH+PCM jacket bed and MH+PCM pool bed) using the same materials and volume of the MH and PCM. The results show that our new design (MH+PCM sandwich bed) outperformed the previous designs (MH+PCM jacket bed and MH+PCM pool bed). Therefore, the performance of the MH-PCM storage system is highly affected by its design, which deserves further improvement. One way that can be considered to further improve the design is to integrate the MH storage system with *cascaded* PCMs. In this technique, multiple PCMs with different melting temperatures and enthalpies are arranged in series (i.e., cascaded) with the aim of providing multi-grade thermal energies and enhancing the overall heat transfer performance of the system.

Even though cascaded PCMs have been widely investigated in various applications [69–71], we are not aware of any previous study that has investigated the integration of cascaded PCMs with an MH storage system. Therefore, the objective here is to implement cascaded PCMs in an MH system to provide further improvement in its performance by reducing the time-duration of the hydrogenation and dehydrogenation processes, a key performance criterion in MH systems. Two different types of PCMs with different melting temperatures and enthalpies are arranged in series and integrated with the MH storage system. A detailed analysis of the impacts of cascaded PCMs and the storage capacity distribution of PCMs on the thermal behavior of the MH storage system is carried out. The findings of the research provide further insight into the use of cascaded PCMs as a thermal regulator in MH storage systems.

3.2 Models, Method and Validation

3.2.1 Model Description of the MH-PCM System

Two designs (i.e., PCM jacket bed and PCM sandwich bed) of the three shown in Table 2.1 are adopted to apply and evaluate the cascaded PCMs technique. Two PCMs are considered: one with a melting point of 591 K (PCM591) and another with a melting point of 580 K (PCM580). The selection criteria of these PCMs will be discussed further in the next section.

For the PCM jacket bed design, Figure 3.1(a) shows the conventional design of the MH-PCM jacket system in which the cylinder of the MH (Mg_2Ni) is encircled by a cylindrical jacket packed with PCM580. The required volume of PCM580 was calculated by assuming all the released heat from the MH reactor can be totally stored in the PCM (see Eq. (3.18)).

To analyze the PCMs' distribution in the cascaded designs, the following parameters are defined:

$E_{tot-PCMs}$: the total storage capacity of the PCMs:

$$E_{tot-PCMs} = E_{PCM580} + E_{PCM591} \tag{3.1}$$

E_{PCM580}: the storage capacity of PCM580 (i.e., the PCM with a melting point of 580 K):

$$E_{PCM580} = V_{PCM580} \cdot \rho_{PCM580} \cdot L_{PCM580} \tag{3.2}$$

E_{PCM591}: the storage capacity of PCM591 (i.e., the PCM with a melting point of 591 K):

$$E_{PCM591} = V_{PCM591} \cdot \rho_{PCM591} \cdot L_{PCM591} \tag{3.3}$$

ϕ_{PCM591}: the distribution ratio of the storage capacity of PCM591 to the total PCMs' storage capacity:

$$\phi_{PCM591} = \frac{E_{PCM591}}{E_{tot-PCMs}} \tag{3.4}$$

$E_{opt-tot-PCMs}$: the total PCMs' storage capacity at the optimum ϕ_{PCM591}:

$$E_{opt-tot-PCMs} = \left(V_{opt-PCM580} \cdot \rho_{PCM580} \cdot L_{PCM580}\right) + \left(V_{opt-PCM591} \cdot \rho_{PCM591} \cdot L_{PCM591}\right) \tag{3.5}$$

$E_{inner-PCMs}$: the storage capacity of the inner PCMs:

$$E_{inner-PCMs} = (V_{inner-PCM580} \cdot \rho_{PCM580} \cdot L_{PCM580}) + (V_{inner-PCM591} \cdot \rho_{PCM591} \cdot L_{PCM591}) \tag{3.6}$$

$\phi_{inner-PCMs}$: the distribution ratio of the storage capacity of the inner PCMs to the total PCMs' storage capacity at the optimum ϕ_{PCM591}:

$$\phi_{inner-PCMs} = \frac{E_{inner-PCMs}}{E_{opt-tot-PCMs}} \tag{3.7}$$

Figure 3.1(b) shows the new design of the MH-PCM jacket system in which the single PCM580 storage capacity in Figure 3.1(a) is distributed between the two PCMs (i.e., PCM580 and PCM591) that are arranged in series. The value of $\phi_{PCM591}$is examined to identify the optimum distribution ratio (Eq. (3.4)).

For the PCM sandwich bed design, the volume of the MH reactor is kept the same as in the PCM jacket design. The value of $\phi_{inner-PCMs}$ is examined to identify the optimum distribution ratio in the new design of the cascaded PCMs' sandwich bed (Eq. (3.7)). Therefore, the new design of the cascaded MH-PCM sandwich system consists of five

concentric cylinders in which the MH (Mg_2Ni) reactor is encircled by two cylindrical sandwich beds packed with two different PCMs (i.e., PCM580 and PCM591), which are also arranged in series as illustrated in Figure 3.1(c).

In the new designs, the PCMs are placed around the MH reactor and arranged in decreasing order of their melting temperatures. Table 3.1 summarizes the thermophysical properties of the PCMs and Mg_2Ni [51,59,72]. The geometrical parameters of the simulated designs are summarized in Table 3.2.

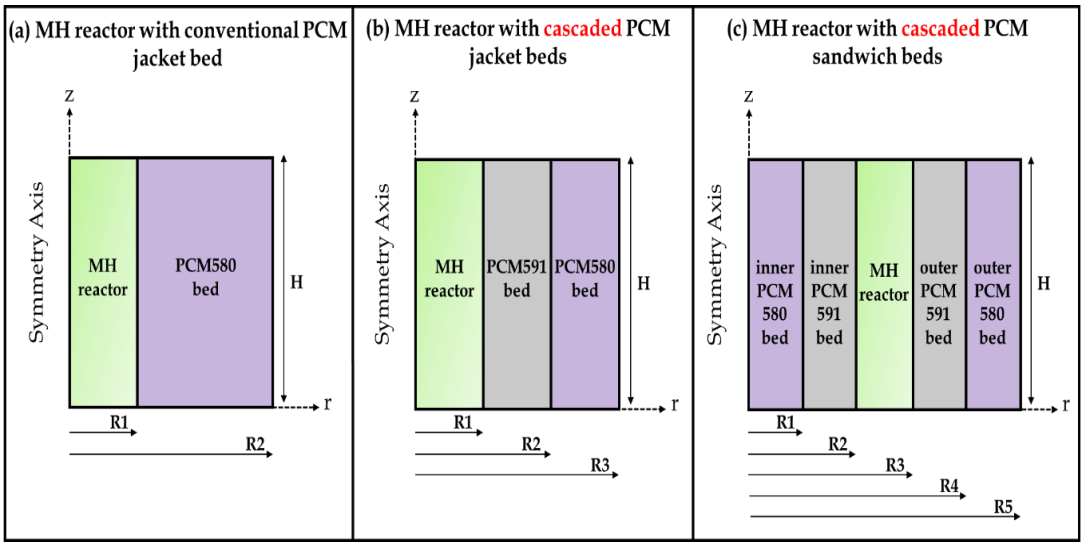

Figure 3.1: Conceptual Schematic of the Three Designs of an MH-PCM Storage System: (a) Conventional MH-PCM Jacket Bed, (b) Cascaded MH-PCM Jacket Beds and (c) Cascaded MH-PCM Sandwich Beds.

Table 3.1: Thermophysical Properties of Mg_2Ni Hydride, PCM580 ($NaNO_3$) and PCM591 (NaOH) [50,59,72].

Parameters	**Mg_2Ni hydride**	**PCM580 ($NaNO_3$)**	**PCM591 (NaOH)**
Density, ρ [kg m^{-3}]	3200	2260	2100
Heat capacity, C_p [J kg^{-1} K^{-1}]	1414	1820	2080
Thermal conductivity, λ [W m^{-1} K^{-1}]	1.33*	0.48	0.92
Latent heat of PCM, L (J g^{-1})	-	174	165
Solidus temperature, T_{sol} [K]	-	579	590
Melting temperature, T_m [K]	-	580	591
Permeability, K [m^2]	10^{-8}	-	-
Porosity, ε	0.5	-	-
Maximum mass content of hydrogen in the metal, *wt* [%]	3.6	-	-
Molar enthalpy of reaction, ΔH [J mol^{-1}]	-64000	-	-
Absorption plateau pressure coefficient, A_{abs}	26.481	-	-
Desorption plateau pressure coefficient, A_{des}	26.181	-	-
Absorption plateau pressure coefficient, B_{abs} [K]	7552.5	-	-
Desorption plateau pressure coefficient, B_{des} [K]	7552.5	-	-
Absorption rate constant, C_{abs} [s^{-1}]	175.31	-	-
Desorption rate constant, C_{des} [s^{-1}]	5452.3	-	-
Activation energy for absorption, E_{abs} [J mol^{-1}]	52205	-	-
Activation energy for desorption, E_{des} [J mol^{-1}]	63468	-	-
* This value is the effective thermal conductivity of Mg_2Ni with aluminum foam [50]			

Table 3.2: Geometrical Parameters of the Simulated Designs.

Parameters		**Values**		
		Fig. 1(a)	**Fig. 1(b)**	**Fig. 1(c)**
R_1	[mm]	20	20	25.98
R_2	[mm]	47.7	35.37	34.43
R_3	[mm]	-	48.74	39.82
R_4	[mm]	-	-	43.88
R_5	[mm]	-	-	48.74
H	[mm]	100	100	100
The volume occupied by metal hydride, V_{Mg2Ni}	[cm^3]	125.66	125.66	125.66
The volume of PCM580, V_{PCM580}	[cm^3]	589.01	353.40*	-
The volume of PCM591, V_{PCM591}	[cm^3]	-	267.38*	-
The volume of inner PCM580 bed, $V_{inner\text{-}PCM580}$	[cm^3]	-	-	212.04**
The volume of inner PCM591 bed, $V_{inner\text{-}PCM591}$	[cm^3]	-	-	160.43**
The volume of outer PCM580 bed, $V_{outer\text{-}PCM580}$	[cm^3]	-	-	141.36**
The volume of outer PCM591 bed, $V_{outer\text{-}PCM591}$	[cm^3]	-	-	106.95**
* These values are based on the optimum storage capacity distribution ratio obtained in section 3.1				
** These values are based on the optimum storage capacity distribution ratio obtained in section 3.2				

3.2.2 Selection of the PCMs

For better performance of a PCM integrated with an MH system, the melting temperature T_m of the PCM should lie in the vicinity of the average temperature of the hydrogenation and dehydrogenation processes of the MH bed, since it impacts the hydrogenation and dehydrogenation times [50]. In chapter 2 [56], PCM580 ($NaNO_3$) was found to be a good candidate to be integrated with Mg_2Ni hydride alloy at hydrogenation and dehydrogenation operating pressures of 12 bar and 3 bar, respectively. The reason is that the PCM580 has T_m=580 K which is equal to the average of the operating temperatures that are constrained

by the operating pressures (i.e., 12 bar and 3 bar) as illustrated in Figure 3.2. Therefore, the same operating pressures and the same PCM580 will be used in chapter 3.

For selecting the second PCM, the T_m of the second PCM has intrinsic influence on the performance of the cascaded PCMs system. For better performance in both the hydrogenation and dehydrogenation processes, this melting temperature must be between the T_m of the first PCM (i.e., PCM580) and the temperature constrained by the hydrogenation operating pressure (i.e., T_{abs} = 605 K) as can be seen in Figure 3.2. Therefore, sodium hydroxide (NaOH) has been chosen as the second PCM (i.e., PCM591) since its melting temperature is 591 K which meets the mentioned criterion. PCM591 absorbs the heat of reaction during the hydrogenation process and consequently its average temperature exceeds the melting temperature of PCM580 (i.e., 580 K). This allows the heat to be absorbed by both PCMs simultaneously and therefore increases the rate of heat transfer. For the dehydrogenation process, the pressure difference between the equilibrium pressure at the melting temperature of PCM591 (~ 9 bar) and the hydrogen pressure (i.e., 3 bar) is larger relative to that with a single PCM (i.e., between ~7 bar and 3 bar). This is beneficial for the process since a larger pressure difference leads to a shorter dehydrogenation time.

On the contrary, choosing a PCM with a melting temperature between the T_m of the first PCM (i.e., PCM580) and the temperature constrained by the dehydrogenation operating pressure (i.e., T_{des} = 555 K) induces a small pressure difference which is not beneficial for the dehydrogenation process. At the same time, it induces a large pressure difference which is advantageous for the hydrogenation process. As a result, it is important to choose a PCM

that attains the best possible performance for both the hydrogenation and dehydrogenation processes. The thermophysical properties of both PCMs (i.e., PCM580 and PCM591) are presented in Table 3.1.

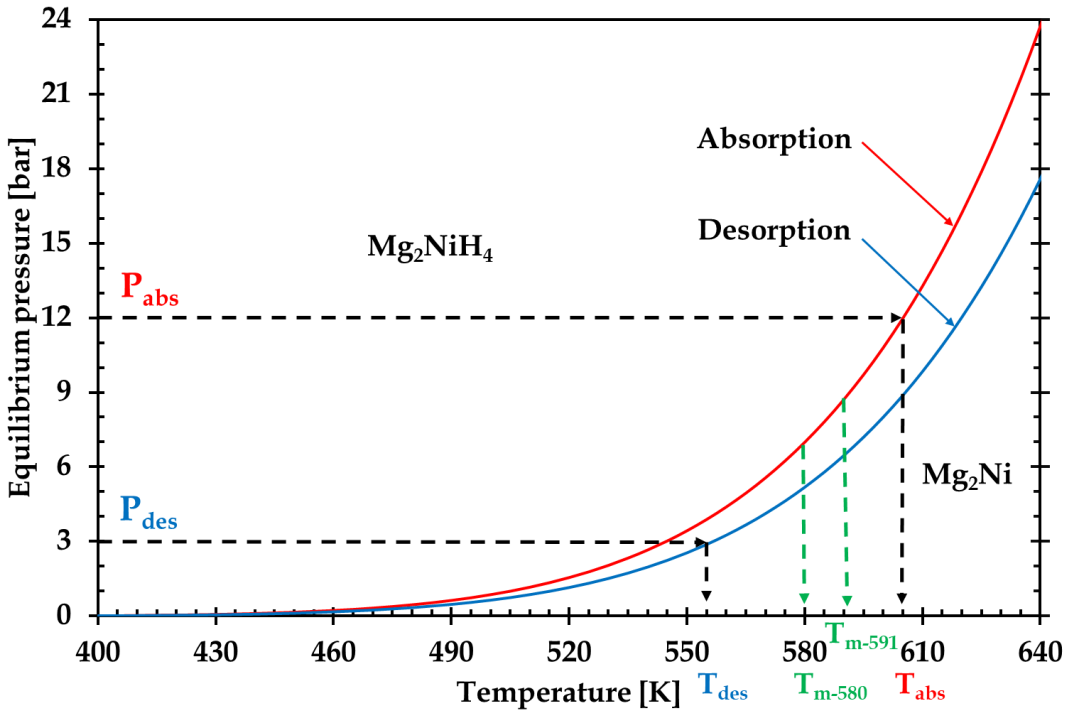

Figure 3.2: Mg_2Ni–Mg_2NiH_4 Equilibrium Chart Showing the Absorption and Desorption Temperatures Imposed by the Absorption and Desorption Pressures.

3.2.3 Numerical Model

The three-dimensional computational domain of the MH-PCM system for the conventional jacket, cascaded jacket and cascaded sandwich designs are shown in Figures 3.1(a), 3.1(b) and 3.1(c), respectively. Because of the axisymmetric nature of this design, only $1/8^{th}$ portion of the computational domain is considered in the numerical simulation. The following assumptions are adopted in the study:

- Local thermal equilibrium is valid [51,59,60].
- The thermophysical properties (density, specific heat and thermal conductivity) are constant [51,54,59].
- The thermal resistance of the interfaces of the MH-PCM system are negligible [48,51].
- The effect of the hydrogen flow is negligible [51,61].
- The hydrogen pressure is uniform throughout the reaction [51,61,62].
- Heat transfer via radiation is neglected [51,61].
- The liquid PCM is assumed to be highly viscous and so the convection heat transfer within it can be neglected [48,51,63].
- The expansion/contraction effect is negligible during the phase transition [42,49,52,54].

3.2.3.1 Mathematical model of the Mg_2Ni hydride reactor

Energy balance

Because of the thermal equilibrium between the MH reactor and hydrogen, the following heat balance equation can be used to compute the system's temperature [50,61]:

$$(\rho \cdot C_P)_{eff} \frac{\partial T}{\partial t} = \nabla \cdot \left(\lambda_{eff} \cdot \nabla(T)\right) + S \tag{3.8}$$

where $(\rho \cdot C_P)_{eff}$ is the effective heat capacity and λ_{eff} is the effective thermal conductivity. The following formula is used to calculate them [50]:

$$(\rho \cdot C_P)_{eff} = \varepsilon \cdot \rho_{H_2} \cdot C_{P_{H_2}} + (1-\varepsilon) \cdot \rho_{MH} \cdot C_{P_{MH}} \quad (3.9)$$

$$\lambda_{eff} = \varepsilon \cdot \lambda_{H_2} + (1-\varepsilon) \cdot \lambda_{MH} \quad (3.10)$$

where ε , ρ, C_P, T and λ are the porosity, the density, the heat capacity, the temperature, and the thermal conductivity, respectively.

The source term (S in Eq. (3.8)) is related to the reaction rate as follows [61]:

$$S = \frac{\rho_{MH} \cdot wt \cdot (1-\varepsilon) \cdot \Delta H_{mol}}{M_{H_2}} \left(\frac{\partial X_{H_2}}{\partial t} \right) \quad (3.11)$$

where M_{H_2} = 0.002 kg mol^{-1} is the molecular mass of hydrogen, ΔH_{mol} the molar enthalpy of reaction, $\frac{\partial X_{H_2}}{\partial t}$ the kinetic reaction, and wt the maximum mass content of hydrogen that can be absorbed by the Mg_2Ni alloy.

Mass balance

In order to simplify the computational simulation and eliminate the need to consider the momentum equations, the effect of the flow of hydrogen is neglected as mentioned above. This can be adopted when the following conditions are met [50,61]:

- The heat transfer by conduction inside the MH reactor is significantly higher than that by convection and radiation.
- The required sensible energy to change the MH temperature is insignificant relative to the enthalpy of the reaction.

- The variation between the equilibrium and hydrogen pressure resulting from the flow of hydrogen doesn't affect the reaction velocity.

Kinetic reaction

The following equation is used to describe the kinetic reaction of the Mg_2Ni hydride for the hydrogenation/dehydrogenation processes [50]:

$$\frac{\partial X_{H_2}}{\partial t} = \begin{cases} C_{abs}\, exp\left(-\frac{E_{abs}}{R_g\, T}\right)\left(\frac{P_{H_2} - P_{eq,abs}}{P_{eq,abs}}\right)\left(X_{H_2,max} - X_{H_2}\right), for\ P_{H_2} > P_{eq,abs} \\ C_{des}\, exp\left(-\frac{E_{des}}{R_g\, T}\right)\left(\frac{P_{H_2} - P_{eq,des}}{P_{eq,des}}\right) X_{H_2} \qquad , for\ P_{H_2} < P_{eq,des} \end{cases} \tag{3.12}$$

where C is the absorption/desorption rate constant, E the activation energy for absorption/desorption, $X_{H_2,max}$ the maximum absorbable hydrogen amount in weight fraction (*wt%*), P_{H_2} the hydrogen pressure, and R_g= 8.314 J K^{-1} mol^{-1} the universal gas constant.

To calculate the absorption/desorption equilibrium pressure P_{eq}, the Van't Hoff relation is used [59]:

$$\frac{P_{eq}}{P_{ref}} = \begin{cases} 10^{-5} \cdot exp\left(A_{abs} - \frac{B_{abs}}{T}\right) \\ 10^{-5} \cdot exp\left(A_{des} - \frac{B_{des}}{T}\right) \end{cases} \tag{3.13}$$

where P_{ref} is 1 bar [59], and the A and B coefficients represent the plateau pressure for absorption and desorption as presented in Table 3.1.

3.2.3.2 Mathematical model of the PCM

The enthalpy-porosity technique is used to model the solidification/liquification process [42,50]. In this method, each computational cell is given a liquid fraction based on its enthalpy balance. The thermal energy equation is expressed as:

$$\frac{\partial}{\partial t}(\rho_{PCM} H_{PCM}) = \nabla(\lambda_{PCM} \nabla T_{PCM}) \tag{3.14}$$

where H_{PCM} is the total enthalpy which combines the latent heat (L_{PCM}) and sensible enthalpy (h_{sen}) of the PCM as expressed below:

$$H_{PCM} = h_{sen} + (f \cdot L_{PCM}) \tag{3.15}$$

where f is the liquid fraction the PCM.

The following formula is used to estimate h_{sen}:

$$h_{sen} = \int_{T_m}^{T} C_{p,PCM} dT_{PCM} \tag{3.16}$$

where $C_{p_{,PCM}}$ is the heat capacity of the PCM.

The value of f represents the liquid fraction of each computational cell (e.g., f = 1 liquid, f = 0, solid and 0 < f < 1 for a two-phase cell). This can be calculated as follows [50]:

$$f = \begin{cases} 0 & T \leq T_{sol} \\ \dfrac{T - T_{sol}}{T_m - T_{sol}} & T_{sol} < T < T_m \\ 1 & T \geq T_m \end{cases} \tag{3.17}$$

where T_{sol} and T_m are the PCM temperature of the solid and liquid phases, respectively.

The required volume of the single PCM and the cascaded PCMs was calculated by assuming the heat released from the MH reactor can be fully stored in the PCM/PCMs. This can be calculated as follows [50]:

- For single PCM design:

$$\frac{V_{MH} \cdot wt \cdot \Delta H_{mol} \cdot \rho_{MH} \cdot (1-\varepsilon)}{M_{H_2}} = E_{PCM580} \tag{3.18}$$

- For cascaded PCMs design:

$$\frac{V_{MH} \cdot wt \cdot \Delta H_{mol} \cdot \rho_{MH} \cdot (1-\varepsilon)}{M_{H_2}} = E_{PCM580} + E_{PCM591} \tag{3.19}$$

The effect of the sensible enthalpy is not taken into consideration to estimate the required amount of PCM because it is assumed to be negligible relative to other terms.

3.2.3.3 Initial and boundary conditions

Initial conditions

$$T_0 = 579\ K \tag{3.20}$$

$$P_0 = 12\ bar \tag{3.21}$$

Boundary conditions

The geometrical boundaries of the system domain are shown in Figure 3.1(a,b,c) and can be expressed as:

- The boundary condition at symmetric and adiabatic walls is

$$\nabla T_{MH} \cdot \vec{n} = \nabla T_{PCM} \cdot \vec{n} = 0 \tag{3.22}$$

- The boundary condition at the interface between the MH reactor and the PCM is

$$\lambda_{MH}\nabla T_{MH}\cdot\vec{n}=\lambda_{PCM}\nabla T_{PCM}\cdot\vec{n} \quad (3.23)$$

- The boundary condition at the interface between the PCM580 and the PCM591 beds is

$$\lambda_{PCM580}\nabla T_{PCM580}\cdot\vec{n}=\lambda_{PCM591}\nabla T_{PCM591}\cdot\vec{n} \quad (3.24)$$

where $\vec{n}$ represents the normal vector to the corresponding wall. These interfaces are defined as coupled walls to allow conjugate heat transfer [30].

3.2.3.4 Numerical method and model validation

The coupled partial differential equations are solved using the ANSYS Fluent 19.2 software. User-defined functions are created to solve the source term in Eq. (3.8), the kinetic reaction rate (Eq. (3.12)), and the equilibrium pressure equations (Eq. (3.13)). This model was validated in our previous study [50] with experimental results reported by Garrier et al. [47].

3.3 Results and Discussion

3.3.1 Determination of the Optimum Storage Capacity Distribution Ratio ϕ_{PCM591}

Finding the optimum distribution of the two PCMs in the cascaded PCM jacket beds design (Figure 3.4(a)) is essential to attain the best performance for its integration with the MH system. Therefore, a parametric study is carried out to investigate the influence of ϕ_{PCM591} on the time-duration of the hydrogenation and dehydrogenation processes of the MH system. Figure 3.3 shows the time-duration of the hydrogenation and dehydrogenation processes as a function of the ratio of the storage capacity of PCM591 to the total PCMs' storage capacity (ϕ_{PCM591}). It can be seen that, when $\phi_{PCM591} > 45\%$, the cascaded MH-PCM system design has a negative effect on the hydrogenation time relative to the MH-PCM system design that integrates only a single PCM580 (i.e., when $\phi_{PCM591} = 0\%$). However, the cascaded MH-PCM system achieves the shortest hydrogenation reaction when $\phi_{PCM591} = 40\%$ as shown in Figure 3.3(a). On the contrary, the dehydrogenation time of the cascaded MH-PCM system design is reduced as ϕ_{PCM591} increases as shown in Figure 3.3(b). From this, it can be concluded that the most appropriate ratio (ϕ_{PCM591}) for both the hydrogenation and dehydrogenation processes is 40%. This ratio determines the amount of PCM591 in the cascaded PCM jacket beds design according to Eq. (3.1)-(3.4). Therefore, the total PCMs' storage capacity is distributed between the PCM591 and the PCM580 with a ratio of 40% and 60%, respectively, as shown in Figure 3.4(a). This optimum distribution ratio ($\phi_{PCM591} = 40\%$) is adopted in the new design of the MH-PCM sandwich system (Figure 3.4(b)) in the following section.

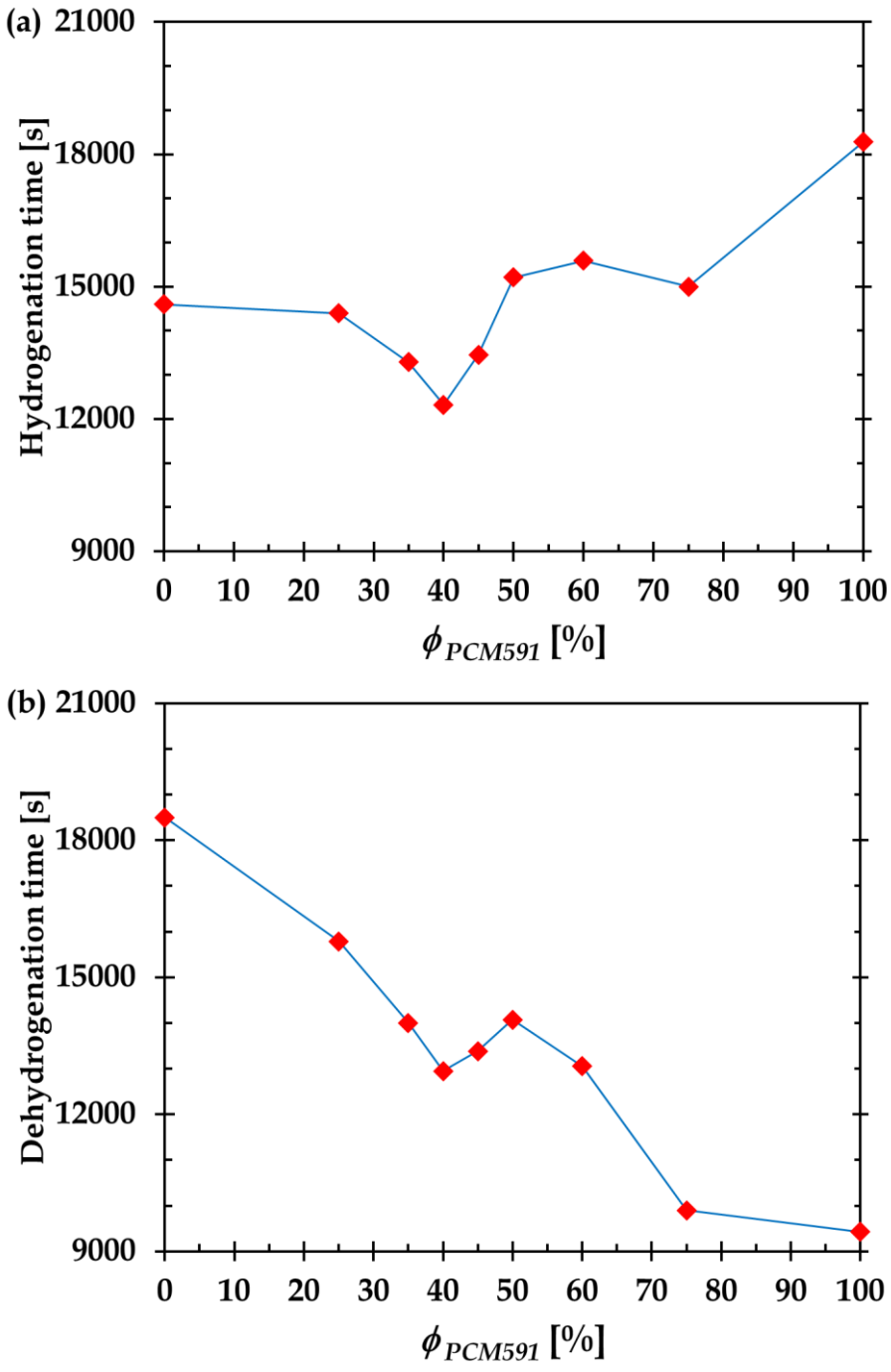

Figure 3.3: The Time-duration of the (a) Hydrogenation and (b) Dehydrogenation Processes as a Function of the Ratio of the Storage Capacity of PCM591 to the Total PCMs' Storage Capacity.

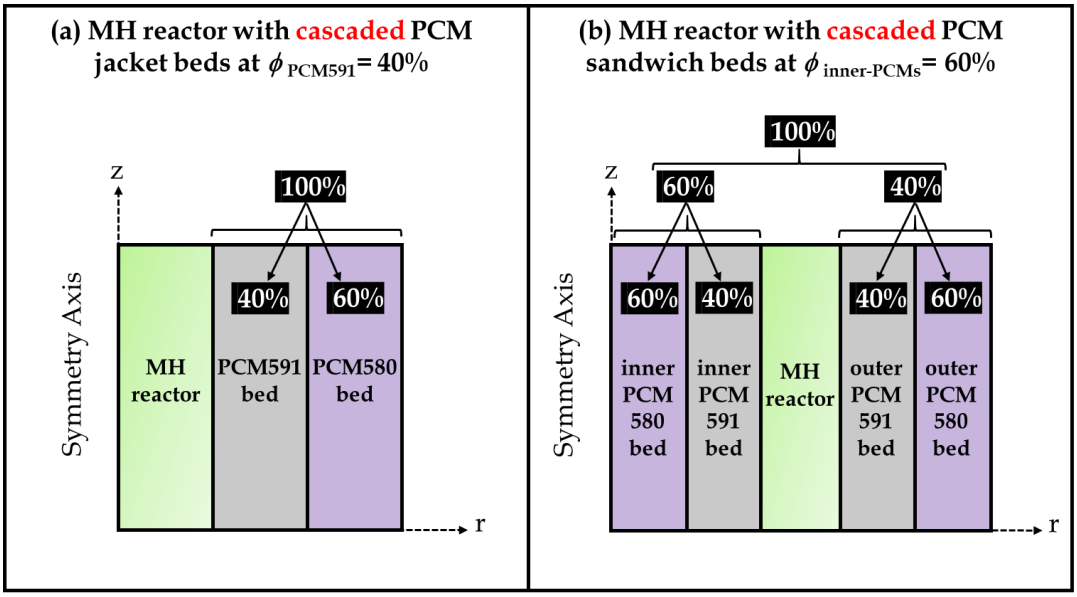

Figure 3.4: Conceptual Schematic of the Optimum Storage Capacity Distribution of the PCMs in (a) the Cascaded MH-PCM Jacket Design and (b) the Cascaded MH-PCM Sandwich Design.

3.3.2 Determination of the Optimum Storage Capacity Distribution Ratio $\phi_{inner-PCMs}$

Considering the objective to achieve the best performance by applying cascaded PCMs in the new design of the MH-PCM sandwich system (Figure 3.4(b)), it is necessary to determine the optimum distribution ratio $\phi_{inner-PCMs}$ between the inner and outer beds. As mentioned earlier in section 3.1, the optimum distribution ratio ($\phi_{PCM591} = 40\%$) is adopted for both the inner and outer beds of the MH-PCM sandwich system as shown in Figure 3.4(b). Then, a parametric study is carried out to investigate the influence of $\phi_{inner-PCMs}$ on the time-duration of the hydrogenation and dehydrogenation processes for the MH system. Figure 3.5 shows the time-duration of the hydrogenation and dehydrogenation processes as a function of $\phi_{inner-PCMs}$. As can be seen in Figure 3.5, the ratio of 60% is the optimum distribution ratio ($\phi_{inner-PCMs}$) in which the shortest

hydrogenation and dehydrogenation times are achieved. Figure 3.4(b) shows the final optimum distribution of the two PCMs for the MH-PCM sandwich design which is adopted for the rest of this chapter.

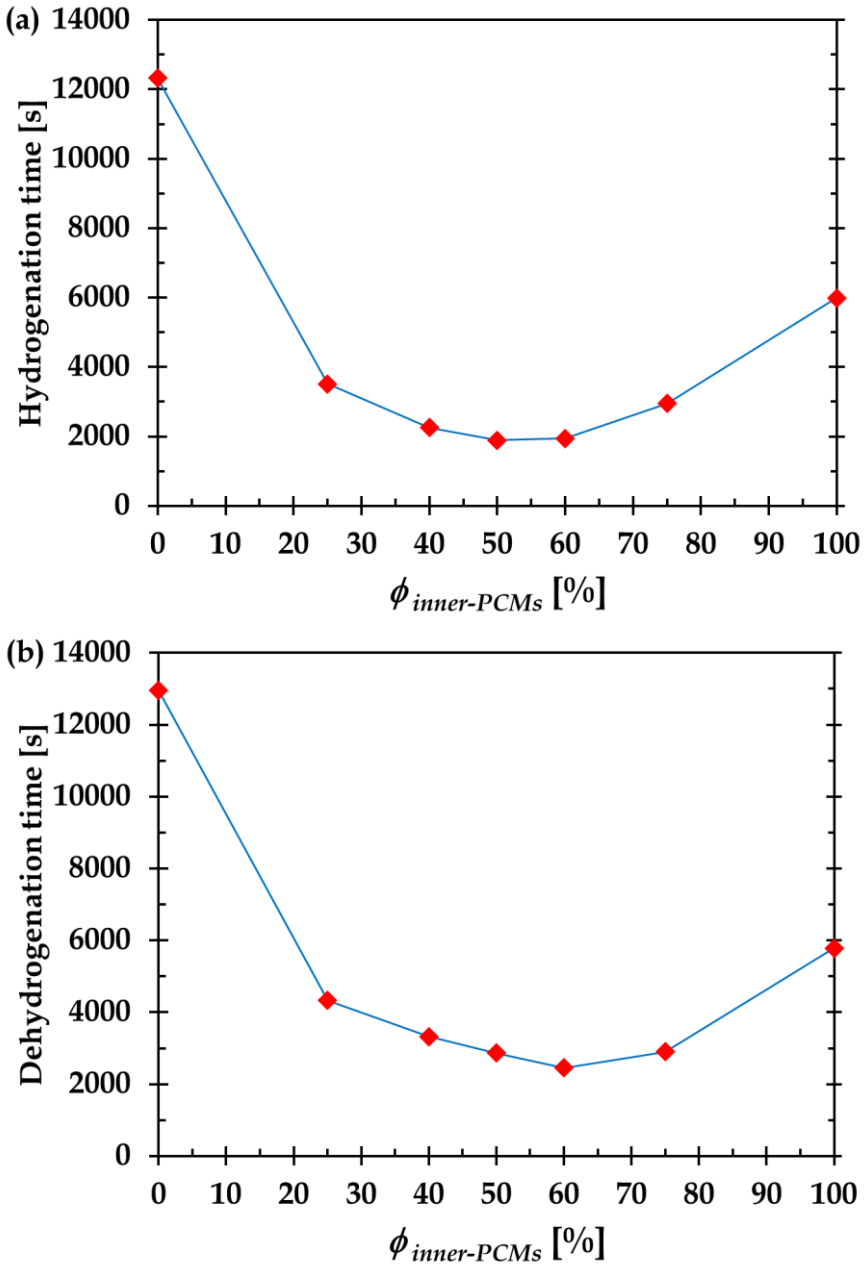

Figure 3.5: The Time-duration of the (a) Hydrogenation and (b) Dehydrogenation Processes as a Function of the Ratio of the Storage Capacity of the Inner PCMs to the Total PCMs' Storage Capacity, at the Optimum Ratio $\phi_{PCM591}=40\%$.

3.3.3 Hydrogenation and Dehydrogenation Cycling of the Cascaded MH-PCM Sandwich Beds Design

To investigate the cyclic behavior of the cascaded MH-PCM sandwich beds design, a detailed analysis of the temperature, equilibrium pressure, hydrogen-reacted fraction and the PCMs' liquid fraction for both the hydrogenation and dehydrogenation processes is performed.

Figure 3.6 depicts the average temperatures of the MH reactor (T_{MH}) and the PCMs ($T_{inner\text{-}PCM591}$, $T_{outer\text{-}PCM591}$, $T_{inner\text{-}PCM580}$ *and* $T_{outer\text{-}PCM580}$) throughout the hydrogenation and dehydrogenation processes for four consecutive cycles. At the initial stage of the hydrogenation process for each cycle, there is a rapid increase in T_{MH} because of the increase in the kinetic reaction term to its maximum in the source equation (Eq. (3.12)) which results in an abrupt increase in T_{MH} according to the energy equation (Eq. (3.8)). This is due to the fact that the rate of reaction reaches its highest value at the initial stage of the exothermic reaction when the difference is maximum between the hydrogen pressure and MH equilibrium pressure (see Eq. (3.13) and Eq. (3.21)). Moreover, the average temperatures of the PCM591 beds adjacent to the MH reactor (i.e., $T_{inner\text{-}PCM591}$ and $T_{outer\text{-}PCM591}$) increase remarkably due to the increase in T_{MH}. On the other hand, the average temperatures of the PCM580 beds (i.e., $T_{inner\text{-}PCM580}$ and $T_{outer\text{-}PCM580}$) increase at a lower rate since they gain heat from the adjacent PCM591 beds. However, $T_{outer\text{-}PCM580}$ increases dramatically after the half-time of the hydrogenation process due to the fact that the outer PCM beds (i.e., outer-PCM591 and outer-PCM580) are fully melted (see Figure 3.7(b)) and therefore they exchange heat only in the form of sensible heat.

For the second half of the first cycle, the MH reactor starts releasing hydrogen throughout the endothermic process, which causes a dramatic decrease in T_{MH} as shown in Figure 3.6. This process is driven by the heat released by the solidification of the PCMs, which experience a decline in their average temperatures. As the reaction continues, the PCM591 beds solidify (see Figure 3.7(b)) and as a result $T_{inner\text{-}PCM591}$ and $T_{outer\text{-}PCM591}$ start increasing gradually due to the gained heat from the adjacent PCM580 beds. These beds (i.e., inner-PCM591 and outer-PCM591) exchange heat with the adjacent MH reactor in the form of sensible heat and this explains the gradual increase in T_{MH}. Before the end of the dehydrogenation process, the outer PCM580 bed solidifies and as a result $T_{outer\text{-}PCM580}$ experiences a dramatic decease until the end of the process. In the following three cycles, the temperature profiles experience the same behavior which demonstrates the consistency of the proposed design.

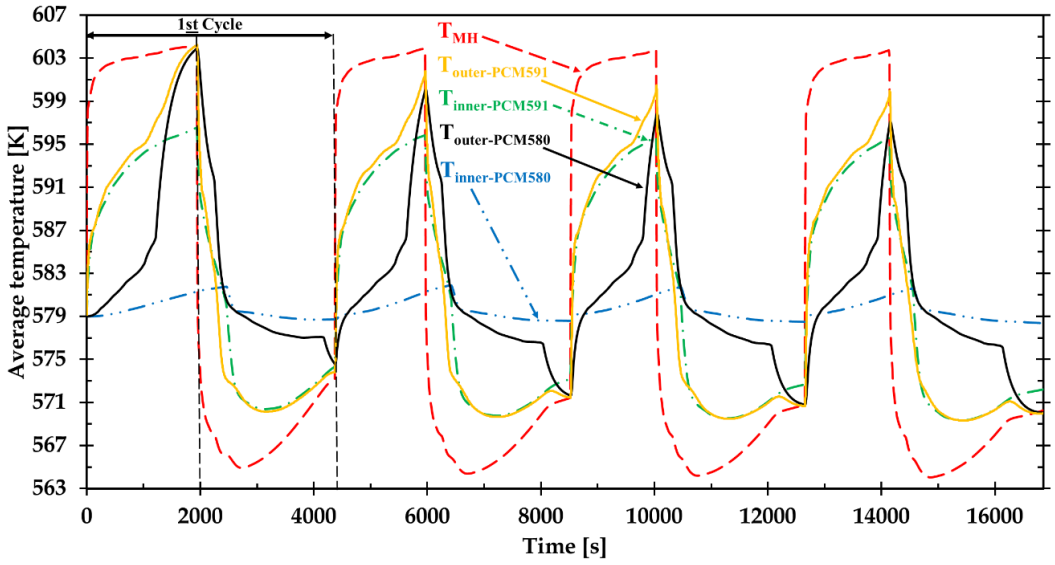

Figure 3.6: Time Evolution of the Average Temperature of the Cascaded MH-PCM Sandwich Design Throughout the Hydrogenation and Dehydrogenation Processes for Four Consecutive Cycles.

Figure 3.7(a) illustrates the time evolution of the hydrogen-reacted fraction throughout the hydrogenation and dehydrogenation processes for four consecutive cycles. For the first cycle, the time durations of the hydrogenation and dehydrogenation processes are 2000 and 2450 seconds, respectively. Apparently, the hydrogenation processes in the last three cycles last for shorter time (~ 1600s) relative to that in the first cycle (2000s). This can be mostly attributed to the fact that the pressure difference (P_{eq}–P_{H2}= ~7.5 bar) is greater in the last three consecutive cycles than that in the first cycle (~5 bar) as shown in Figure 3.8. In other words, the driving force of the hydrogenation reaction in the first cycle is relatively lower than that in the following three cycles. To clarify this, it important to point out that the starting equilibrium pressure for the first cycle is higher (~7 bar) and that is attributed to the starting T_{MH} (~579 K) as annotated in Figure 3.8. On the contrary, in the last three cycles, the starting T_{MH} (~573 K) (see Figure 3.6) constrains the equilibrium pressure at a lower value (~4.5 bar) as described by Eq. (3.13). In general, the last three cycles demonstrate a consistent behavior of hydrogenation and dehydrogenation processes for extended cycling, which enables stable operation of the MH-PCM storage system.

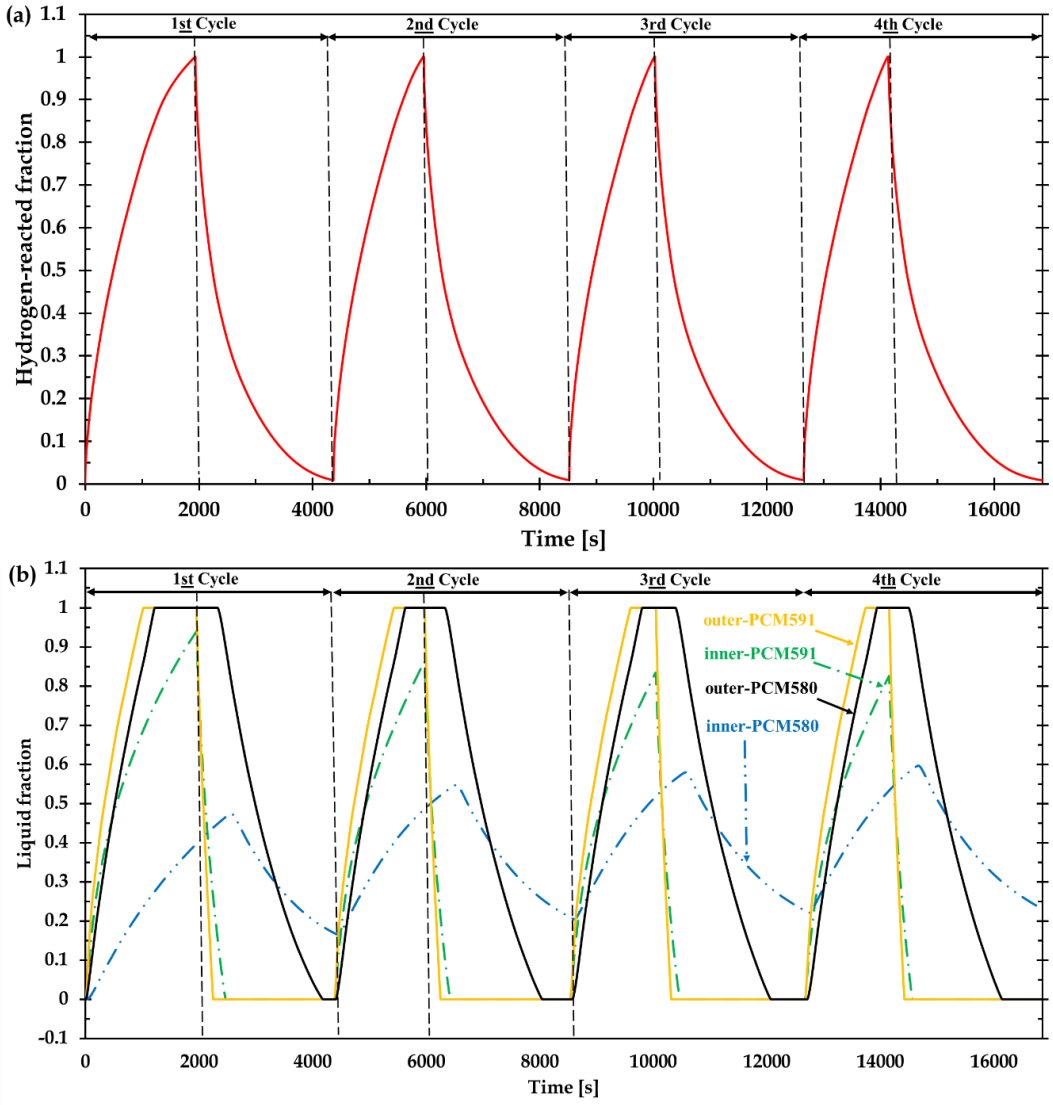

Figure 3.7: The Time Evolution of (a) the Hydrogen-reacted Fraction and (b) the PCMs' Liquid Fraction Throughout the Hydrogenation and Dehydrogenation Processes for Four Consecutive Cycles.

The time evolution of the PCMs' liquid fraction (inner-PCM591, outer-PCM591, inner-PCM580 and outer-PCM580) for four consecutive cycles is shown in Figure 3.7(b). In general, the liquid fraction trends show a good correspondence to the hydrogen-reacted fraction throughout the hydrogenation and dehydrogenation processes. During the hydrogenation process in the four consecutive cycles, it can be noted that the outer PCM beds (i.e., outer-PCM591 and outer-PCM580) are fully melted while the inner PCM beds

(i.e., inner-PCM591 and inner-PCM580) are only partially melted. This is mostly because of two reasons: (i) the storage capacity of the outer PCMs is less than that of the inner PCMs, and (ii) the surface area of the outer PCM beds' interfaces are larger than those of the inner PCM beds. On the other hand, during the dehydrogenation process, the PCM591 beds (i.e., inner and outer PCM591) are fully solidified first and this is due to the fact that these beds are adjacent to the MH rector. Figure 3.8 shows the average equilibrium pressures (P_{eq}) within the MH reactor throughout the hydrogenation and dehydrogenation processes for four consecutive cycles. Because P_{eq} is a function of T_{MH} (Eq. (3.13), the trends for P_{eq} are quite similar to those of T_{MH} in Figure 3.6.

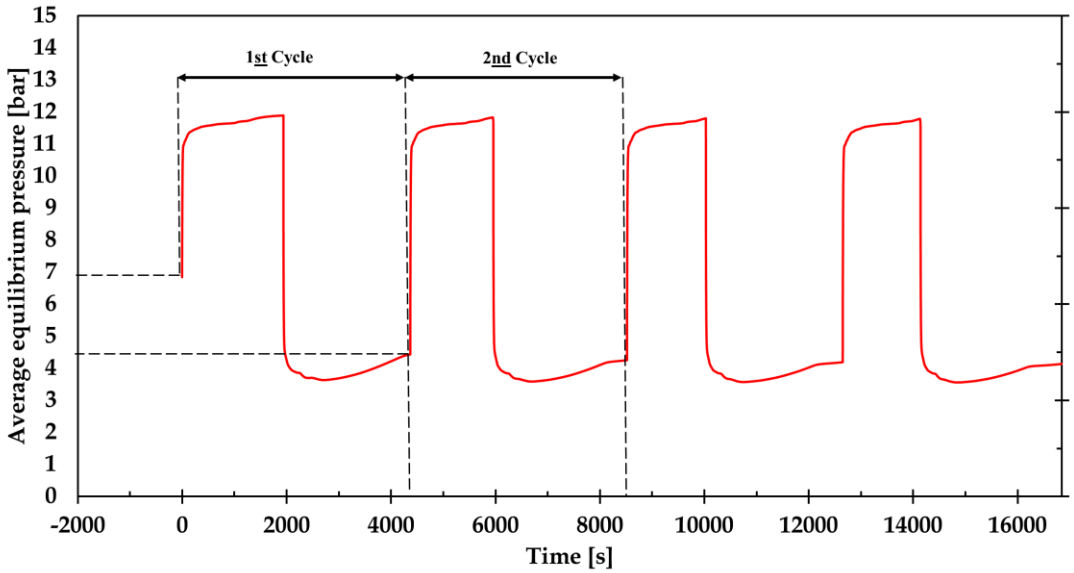

Figure 3.8: The Time Evolution of the Equilibrium Pressure Throughout the Hydrogenation and Dehydrogenation Processes for Four Consecutive Cycles.

3.3.4 Comparison Between the Cascaded MH-PCM Designs and the MH-PCM Designs with a Single PCM

To investigate the effectiveness of the proposed design in the current study, the cascaded MH-PCM designs are compared with the MH-PCM designs that include only a single PCM. For a practical comparison, the volume of the MH reactor and the storage capacity of the PCM(s) are kept the same in all cases. Figure 3.9 shows a comparison of the time evolution of the hydrogen-reacted fraction throughout the hydrogenation (Figure 3.9(a)) and the dehydrogenation (Figure 3.9(b)) processes between the cascaded MH-PCM designs and the MH-PCM designs only with a single PCM.

First, an MH reactor with cascaded PCM jacket beds is compared with a conventional MH-PCM design that includes only a single PCM jacket. As shown in Figure 3.9(a,b), the time duration required for the hydrogenation and dehydrogenation processes was improved by 16% and 30%, respectively, for the cascaded MH-PCM jacket beds design compared to the MH-PCM design that includes only a single PCM.

Second, in chapter 2 [56], an MH reactor was integrated with a single PCM sandwich bed design and compared with other designs from previous studies as summarized in Table 2.1. It was apparent that the MH-PCM sandwich bed design which includes only a single PCM outperformed the previous designs. To investigate the effectiveness of the proposed design here, the cascaded MH-PCM sandwich beds design is compared with the MH-PCM sandwich bed design that includes only a single PCM. The results showed that the time duration required for the hydrogenation and dehydrogenation processes was improved by 26% and 51%, respectively as shown in Figure 3.9(a,b). Therefore, integrating cascaded

PCMs with the MH storage system demonstrates its feasibility to be taken into consideration in future work for further performance improvement.

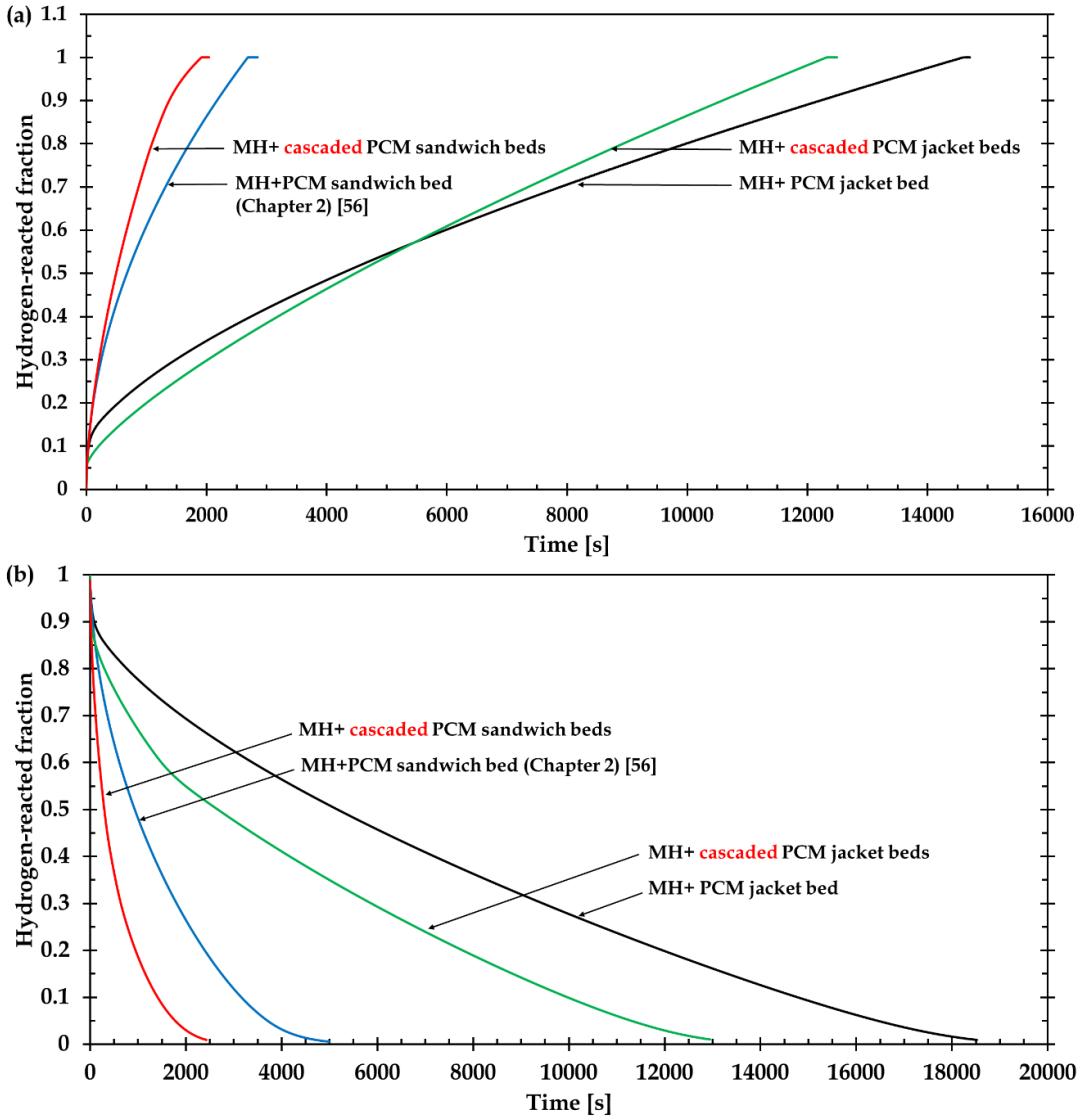

Figure 3.9: Comparison of the Time Evolution of the Hydrogen-reacted Fraction Throughout the (a) Hydrogenation and (b) Dehydrogenation Processes Between the Cascaded MH-PCM Designs and the MH-PCM Designs with Only a Single PCM.

3.4 Summary

A new design that integrates an MH storage system with cascaded PCM (PCM = phase change material) beds is proposed. The system performance is investigated numerically to predict the optimum storage capacity distribution ratio of the PCMs, the time evolution of the MH-PCM system temperature, equilibrium pressure, hydrogen-reacted fraction and liquid fraction. Two PCMs were considered: one with a melting point of 591 K (PCM591) and another with a melting point of 580 K (PCM580). It is found that the optimum storage capacity ratio of the PCM591 to the PCMs' total storage capacity (ϕ_{PCM591}) is 40%, whereas the optimum storage capacity of the inner PCM beds to the total PCMs' storage capacity, with ϕ_{PCM591} = 40%, is 60%.

The time duration required for the hydrogenation and dehydrogenation processes was improved by 16% and 30%, respectively, for the proposed cascaded MH-PCM jacket beds design compared to the MH-PCM jacket design that includes only a single PCM. Moreover, the improvement (time reduction) for the hydrogenation and dehydrogenation processes was 26% and 51%, respectively, for the cascaded MH-PCM sandwich beds design relative to the MH-PCM sandwich design that includes only a single PCM.

Furthermore, the proposed design in the current study demonstrates a consistent behavior of hydrogenation and dehydrogenation processes for extended cycling, which enables stable operation of the MH-PCM storage system.

4. UNCONDITIONED BUILDING EQUIPPED WITH COCONUT OIL PCM[3]

Nowadays, because of the excessive use of air conditioning and heating systems, energy consumption by the building sector represents roughly 40% of total global consumption [5]. Thermal Energy Storage (TES) technologies are proving viable options for solving this problem in buildings. Sensible or latent heat storage techniques could be used to implement TES in buildings [73,74]. Sensible heat storage requires massive materials (stone, concrete etc.) to absorb a considerable amount of heat inside the building's skin and has been used for decades in traditional construction. However, this technique is not compatible with the widely used lightweight envelopes due to their low thermal inertia. Unlike sensible heat storage, latent heat TES introduces a higher energy storage density in a narrow temperature range [75,76]. Thus, various PCMs can be used to control the indoor environment of unconditioned lightweight building.

Lightweight buildings may result in overheating during the day and heat loss during the night. Otherwise, increasing the thermal mass in lightweight envelope structures can reduce indoor temperature fluctuations during the hot season, and act as insulators in the cold season [77]. Thus, because of their high volumetric storage density, the integration of PCMs in the building envelope can be an acceptable solution to raise the thermal mass of building structures with very small mass materials [1,78], especially for unconditioned buildings.

[3] Published in the International Journal of Energy Research as:

***T. Alqahtani**, S. Mellouli, A. Bamasag, F. Askri, P. Phelan, Experimental and numerical assessment of using coconut oil as a phase-change material for unconditioned buildings, Int J Energy Res. (2020) 1–20. doi:10.1002/er.5176.*

4.1 Review of Literature

Over the past three decades various PCMs have been studied and assessed both experimentally and numerically in various ranges of outdoor conditions [78,79]. Schossig et al. [80] introduced optimized microencapsulated PCMs which were added to the walls of a full-size test room, and compared with a control room. They noted that, for the test room, the indoor air temperature was lowered by 4°C during summer time and the number of hours at which the indoor temperature was above 28 °C was significantly reduced. Cabeza et al. [81] conducted experimentally a similar research, where an innovative concrete with macro encapsulated PCM was used in a PCM cubicle. The results indicated that, compared to the control cubicle, the indoor temperature fluctuation was lowered. Kuznik et al. [82] studied a full-scale retrofit room with a new PCM wallboard. It was found that a PCM thickness of 5 mm doubled the energy stored and minimized variations in the indoor air temperature by 26%. Berroug et al. [83] discussed and analyzed the effect of a north wall built with PCM in an east-west faced. They found that relative humidity was reduced by 10-15% at night time and 4 cm of PCM was sufficient for heating a greenhouse located in Marrakesh, Morroco. Athienitis et al. [84] experimentally and numerically studied a passive solar retrofit room equipped with a PCM gypsum board. A 4°C reduction of the room temperature during the daytime was obtained with the PCM. Meng et al. [85] explored a new composite PCM room where two PCMs with different melting points were placed in different walls. The authors found that the room temperature was lowered by a maximum of 7.7 °C during sunny summer days. During winter nights, the temperature increased by 6.9 - 9.5 °C. Zhang et al. [86] experimentally evaluated a frame wall equipped with a macro-encapsulated highly crystalline paraffin PCM. The obtained results showed

that maximum heat fluxes at the wall were reduced by 38%. In a similar simulation for California, USA, Lee and Medina [87] assessed the influence of phase change frame walls using a hydrated salt PCM on the thermal performance of two side-by-side houses with identical construction. Simulated results indicated that the phase change walls would reduce the top heat fluxes by 27.3%. The thermal performance of a gypsum wallboard incorporated with nano-PCM, which is made of a fatty acid-based PCM (capric and palmitic acids) and graphite-joined nano sheets, was tested experimentally and numerically by Sayyar et al. [88]. It was found that, for the test cell, the top load shifting of the control cell was much less than that of the test cell. Also, this work noted that the variations of the indoor air temperature of the control cell (13-32°C) were higher than those of the nano-PCM cell (18.5-26.5°C). Shi et al. [89] experimentally evaluated concrete walls incorporated with macro-encapsulated paraffin PCM in Hong Kong. The results showed a decrease in the indoor temperature by 4 °C and indoor relative humidity by 16%. A commercial BioPCM (soy and palm kernel oils) was used by Sage-Lauck and Sailor [90] in an unconditioned house in Oregon, USA, to enhance the internal comfort and to lower the number of overheated hours. The BioPCM incorporated in the walls and ceiling of the west and east units served as a reference. The results indicated that a reduction from 400 to 200 of the annual overheated hours can be obtained with the PCM application. The energy performance of an envelope equipped with PCMs was evaluated numerically by Lei et al. [91]. A simplified cubic model was proposed to predict the cooling load reduction given by the integration of a PCM into the envelope structure. It was noted that, with a proper phase change point, the PCM can lead to a reduction of about 32% of the heat gains through the building envelopes. Hasan et al. [92] tested experimentally the impact of using paraffin wax

PCM wallboard on thermal comfort in Iraq. Two identical envelopes were built and evaluated according to the orientation and PCM thickness. It was found that the indoor air temperature and the cooling load of the test envelope were reduced by 2.18 °C and 20.9%, respectively. Goia et al. [93] compared a traditional double-glazed window with a glass with incorporated paraffin wax PCM window in three different seasons. The results showed a considerable improvement in indoor thermal environment for the entire year except for cloudy days.

The thermal behavior of many PCMs such as salt hydrates, paraffin waxes, and non-paraffin organic acids, has been studied by many researchers. Among all PCMs, fatty acids have attractive features, like congruent cooling and melting; high latent heat of fusion; nontoxicity; nonflammability; little or no volume change and super cooling; low cost; and good thermal and chemical stability after many thermal cycles [73,94,95]. Thus, fatty acids seem to be suitable PCM candidates for building applications**.** Coconut oil (co-oil) belongs to the fatty acid organic PCMs class made from renewable feedstocks and is currently relatively little studied and used.

Coconut oil, for a large number of phase-change cycles, is thermally stable and with no risk of oxidation. This is because it is fully hydrogenated. It melts and freezes at human body comfort temperatures. Also, coconut oil can store and release a large amount of heat (77-100 kJ kg^{-1} [96]) in a manner like conventional paraffin [97]. So, its use in passive solar TES application in buildings is very appropriate. On the other hand, its low thermal conductivity represents a major drawback [98]. Nevertheless, the promising characteristics

of co-oil PCM has prompted several researchers to study the thermal behavior of co-oil PCM for building applications.

Wonorahardjo et al. [96] experimentally investigated the effect of co-oil on a room air conditioning system in a tropical climate in Indonesia. Three different co-oil cell sizes were tested in an idealistic room environment where the desired environment was adjusted by using a thermal chamber. Results showed that the use of 135-170 kg of co-oil can reduce the temperature of an ideal 12 m^2 room by 2-2.5 °C in the afternoon. Low thermal conductivity, however, is a major drawback of co-oil and to overcome this problem, researchers have added appropriate dopant materials such as graphite or metal nanoparticles. Boussaba et al. [99] explored a novel composite-PCM to enhance the thermal inertia of building envelopes. They incorporated the co-oil into a composite matrix from fibers of cellulose and clay. The results showed that the composite-PCM is appropriate for passive solar TES application in building envelopes. Wi et al. [98] prepared and investigated fatty acid organic PCMs to enhance their fire-retardant properties and thermal conductivity. They impregnated co-oil and palm oil into exfoliated graphite nanoplatelets (xGnP). It was noted that the thermal conductivity of the new composite invreased by 400% and can enhance significantly the TES rate in buildings. Özonur et al. [100] evaluated coco fatty acid microcapsules mix with gelatin-gum as a wall material by a complex coacervation technique. Results indicated that the prepared mixture of coco fatty acid would be a candidate for PCM building applications. So far, these studies have only been performed within laboratory environments, and there remains no study conducted in the field, i.e., under ambient weather conditions, to evaluate the effectiveness of the use of coconut oil

for TES in buildings. This is the impetus behind the present research. To the best of the authors' knowledge, no published work has investigated building envelopes with co-oil PCM in the field with realistic-sized buildings.

The main objectives of chapter 3 are to demonstrate the possibility of integrating co-oil PCM into lightweight envelopes for heat gain reduction, and to study the effect on the indoor temperature and humidity change. Additionally, this research deals with the effect of window orientation and the thickness of the co-oil layer. This study is performed in two phases. The first phase involves experimental field tests on two identical single-room buildings under ambient weather conditions rather than a laboratory setting. In the second phase, a numerical model is validated with the experimental data, and is used to investigate the contribution of co-oil to the thermal performance of buildings for the entire year. Therefore, the results are expected to show the efficacy of integrating co-oil PCM into lightweight buildings for heat gain reduction as well as for improving the thermal comfort of the inhabitants.

4.2 Experimental Setup

4.2.1 Materials and Test Rooms

During the months of February and March 2018, the field tests were conducted using two identical unconditioned single-room test buildings (120 cm × 120 cm × 220 cm) located at King Khalid University, Abha, Saudi Arabia. A double-glazed window (80 cm × 60 cm) was installed on one side of each building. The two test buildings are shown in Figure 4.1, are built with the same structural materials. One building was used as the control and the other as the test which contained 105 kg of PCM. The walls and ceilings of the buildings were made of lightweight construction, as described next.

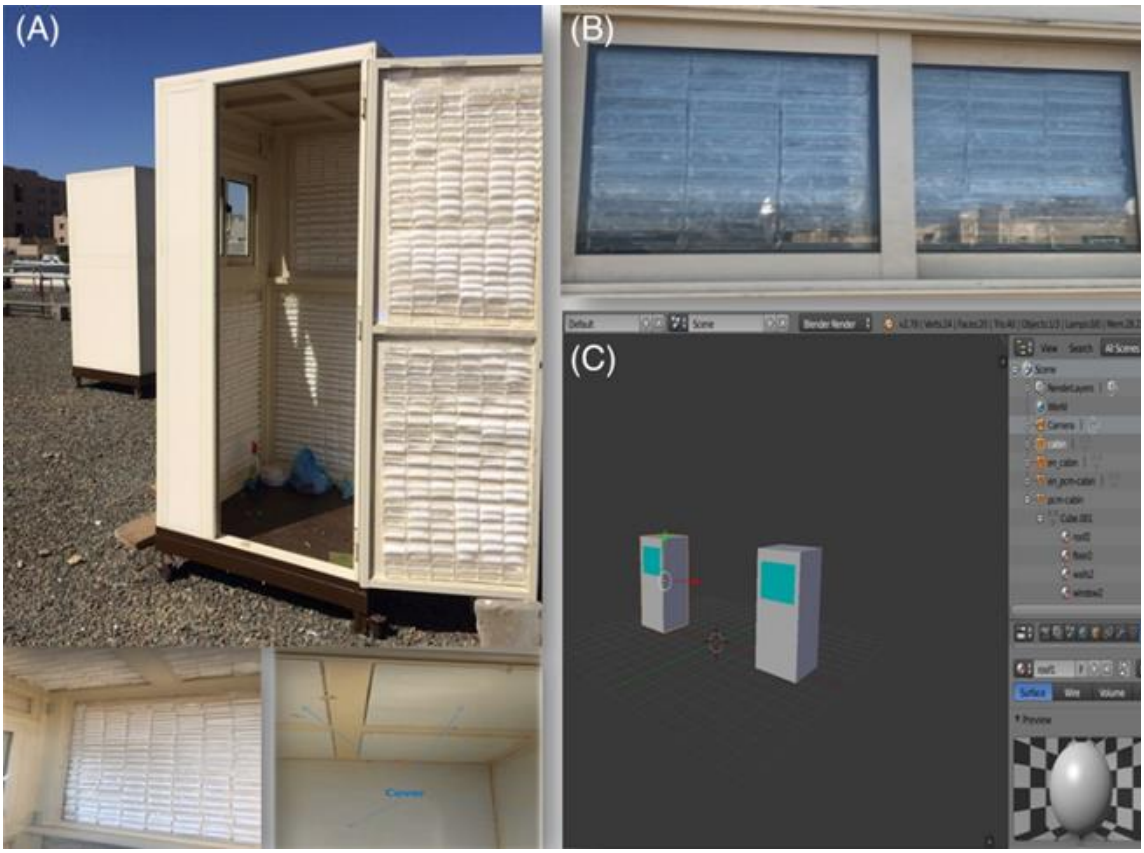

Figure 4.1: (a) Appearance of Experimental Field-test, (b) Window With PCM and (c) Simulation Model.

The walls and ceiling of the control building consist of one layer of a 6-mm-thick Formica laminate board with a thermal conductivity of 0.25 W m^{-1} K^{-1} [101]. The floor was made of 30-cm-thick wood with a thermal conductivity of 0.136 W m^{-1} K^{-1} [82].

For the test building, 1-cm-thick co-oil PCM was used as TES. The PCM was placed in the internal side of the walls and ceiling in square pouches as shown in Figure 4.1.
As mentioned earlier the kind of PCM used in this study was co-oil PCM which is the focus of the current study. Coconut oil has latent heat capacities of melting and freezing of 106.17 kJ kg^{-1} and 107.34 kJ kg^{-1}, respectively, as determined experimentally. Its respective freezing and melting temperatures were measured as 17.44 ℃ and 22.63 ℃ [99], and additional material properties are shown in Table 4.1.

Peippo et al. [102] numerically investigated the optimum melting temperature of a PCM. They concluded that a PCM with a melting point of 1-3 ℃ above the average building temperature is able to attain its optimal diurnal heat storage. It has been formerly stated that the efficiency of PCM in building applications is directly influenced by climatic conditions [6,7]. Souayfane et al. [79] showed a strong relation between the climate condition and the effective performance of PCM. Relatively speaking, semi-arid deserts do not get very hot during the day nor very cold during the night, as opposed to typical conditions in hot and dry deserts. During the summer, temperatures can average between 21-27°C and do not exceed 38°C during the day and are around 10°C at night [103]. These points induced the authors of the present paper to perform the experiment in Abha, Saudi Arabia (18.24°N, 42.51°E), where co-oil PCM may yield significant diurnal heat storage. Abha is located in the southwest of Saudi Arabia and has a semi-arid climate with mild

weather throughout the whole year [104]. For such locations, it is much preferred to reduce the temperature during daytime and increase it during the nighttime.

4.2.2 Instrumentation and Measurements

Temperature and humidity were recorded by a PCE-HT 71N Data-Logger [105] (PCE Americas Inc., Florida, USA) which is capable of detecting and recording data into its internal memory. The PCE-HT 71N works as a Data-Logger that simultaneously measures and records temperature over the range of −40 to 70 °C (measurement accuracy: ±0.1 °C) and humidity in a range of 0 to 100% RH (measurement accuracy: ±3% RH). The PCE-HT 71N Data-Loggers were placed in the middle of the two test buildings at a height of 120 cm for collecting the indoor data, and a separate unit was placed outside at a height of 200 cm for collecting the outdoor data. The time interval for the collected data was set at 15 min; however, these values were averaged on an hourly basis. A pyranometer SR22 [106] (measurement accuracy: ±3% for hourly sums) was used to collect the solar irradiance. The pyranometer SR22 was installed outside at a height of 150 cm in order to reduce the effect of shadows.

Table 4.1: Physical Characteristics of the Materials Used.

Materials	Thickness (cm)	Thermal conductivity (W $m^{-1}°C^{-1}$)	Density (kg m^{-3})		Thermal capacity (J $kg^{-1}°C^{-1}$)		Phase change temperature (°C)		Latent heat (kJ kg^{-1})	
			Solid	Liquid	Solid	Liquid	Solidification	Melting	Solidification	Melting
Coconut oil	1	0.321 [94]	903	-	2900	2100 [99]	17.44	22.63	107.34	106.17 [96]
Formica laminate [98]	0.6	0.25	1450	-	-	-	-	-	-	-
Wood Plate [79]	30	0.136	544	-	1640	-	-	-	-	-
Glass [79]	0.1	1	2500	-	770	-	-	-	-	-

4.3 Numerical Simulation

4.3.1 Simulation Software

The energy model was developed with the 3D design package Blender [107] and simulated with EnergyPlus [108]. Blender geometry and materiality was converted to the EnergyPlus input format by using the VI-Suite [109] with an add-on for the 3D content creation application Blender. The basic Blender geometry model is shown in Figure 4.1(c).

4.3.2 Relationship for the Optimal PCM Layer Thickness

For an optimal operation of passive PCM storage, the PCM layer thickness is considered as one of the most important parameters [110,111]. An obvious merit of increasing the PCM layer thickness is to raise the heat storage capacity. For example, the heat storage capacity of a wall can be five times greater when the wall is integrated with 30% PCM [5]. However, for a very thick layer of PCM, the gained solar energy may not be adequate to melt the PCM completely. On the other hand, for a very thin PCM layer, it may melt too early and heat up excessively. So, it is important to find the optimum PCM thickness that provides the best thermal inertia for lightweight buildings.

During the night time, incomplete energy release reduces energy absorption in the subsequent day (since the system begins the following morning at a partially charged state). In building applications, an efficient latent heat storage device requires all energy absorbed in the day time to be released at night time. This efficiency condition can be used to determine the optimal PCM layer thickness to avoid an excessively thick PCM layer and high material costs. In this study, by employing a simplified heat transfer analysis [102,110,111], an approximate formula of the optimal thickness of co-oil PCM layer is

developed. The physical model of the PCM layer is presented in Figure 4.2. The main assumptions are the heat transfer is dominated by conduction, the temperature profile is quasi-steady, and the volume is constant.

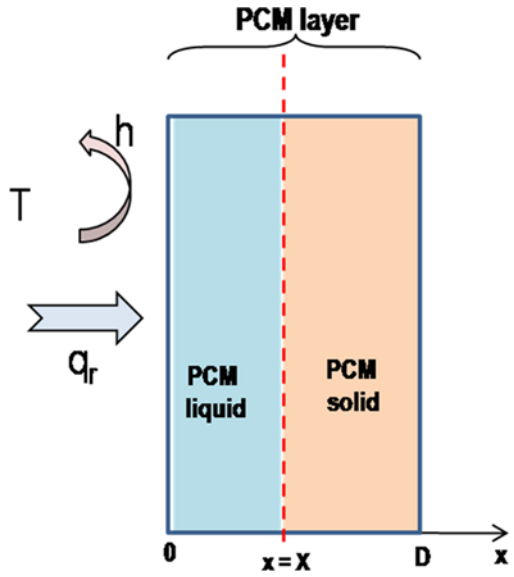

Figure 4.2: Physical Model of the PCM Layer.

The melting process of the PCM layer is described by the following equations:

The initial and boundary conditions are:

$$T(x, t = 0) = T_m \tag{4.1}$$

$$X(t = 0) = 0 \tag{4.2}$$

For $x = 0$

$$-\lambda_l \frac{\partial T}{\partial x}\Big|_{x=0} = q_r - h_d[T(x = 0, t) - T_d] \tag{4.3}$$

For $0 < x < X$

$$\frac{\partial T}{\partial t} = \frac{\lambda_l}{\rho C_{p_l}} \frac{\partial^2 T}{\partial x^2} \tag{4.4}$$

For $x = X$

$$T|_{x=X} = T_m \tag{4.5}$$

$$\rho \Delta H \frac{\partial X}{\partial t} = -\lambda_l \frac{\partial T}{\partial x}\Big|_{x=X} \tag{4.6}$$

where T is the PCM temperature (°C), x the space coordinate (m), t time (s), X the position of the liquid/solid front (m), λ the PCM thermal conductivity (W m^{-1} $°C^{-1}$), ρ the co-oil PCM density (kg m^{-3}), C_p the PCM specific heat capacity (J kg^{-1} $°C^{-1}$), T_m the melting temperature of the co-oil PCM (°C), q_r the average daily heat flux on the wall surface (W m^{-2}), h the convective heat transfer coefficient (W m^{-2} $°C^{-1}$), and ΔH the co-oil PCM latent heat of fusion (J kg^{-1}).

The temperature profile in the PCM layer is assumed to be linear:

$$T = Ax + B \tag{4.7}$$

where A and B are constants.

For $x = 0$

$$-\lambda_l \frac{\partial T}{\partial x}\Big|_{x=0} = q_r - h_d[T_0 - T_d] \tag{4.8}$$

For $x = X$

$$T = T_m \tag{4.9}$$

The temperature profile equation (4.7) can be solved from Eqs. (4.8) and (4.9), and the constants *A* and *B* are found as

$$A = -\frac{q_r - h_d(T_m - T_d)}{\lambda_l + h_d X} \tag{4.10}$$

$$B = T_m + \frac{q_r - h_d(T_m - T_d)}{\lambda_l + h_d X} X \tag{4.11}$$

$$T(x,t) = \left[-\frac{q_r - h_d(T_m - T_d)}{\lambda_l + h_d X}\right] x + T_m + X\left[\frac{q_r - h_d(T_m - T_d)}{\lambda_l + h_d X}\right] \tag{4.12}$$

Finally, the temperature profile can be expressed from Eq. (4.12) as a function of the liquid/solid front *X* and time *t* :

$$T(x,t) = T_m + \frac{q_r - h_d(T_m - T_d)}{\lambda_l + h_d X}(X - x) \tag{4.13}$$

The position of the liquid/solid front *X* can be solved from Eq. (4.5) (Stefan condition) :

$$\rho \Delta H \frac{\partial X}{\partial t} = -\lambda_l \frac{\partial T}{\partial x}\Big|_{x=X} = \lambda_l \frac{q_r - h_d(T_m - T_d)}{\lambda_l + h_d X} \tag{4.14}$$

$$(\lambda_l + h_d X)\frac{\partial X}{\partial t} = \frac{\lambda_l}{\rho \Delta H}[q_r - h_d(T_m - T_d)] \tag{4.15}$$

$$\frac{\partial X}{\partial t} + \frac{h_d}{2\lambda_l}\frac{\partial X^2}{\partial t} = \frac{1}{\rho \Delta H}[q_r - h_d(T_m - T_d)] \tag{4.16}$$

The integration of Eq. (4.16) yields

$$\int_0^{t_{ch}} \left[\frac{\partial X}{\partial t} + \frac{h_d}{2\lambda_l}\frac{\partial X^2}{\partial t}\right] dt = \int_0^{t_{ch}} \left[\frac{1}{\rho \Delta H}[q_r - h_d(T_m - T_d]\right] dt \tag{4.17}$$

$$D_l + \frac{h_d}{2\lambda_l} D_l^2 = \frac{t_{ch}}{\rho \Delta H} [q_r - h_d(T_m - T_d)] \quad (4.18)$$

where D_l is the thickness of the liquid region at $t = t_{ch}$.

For the solidification process a similar analysis can be made for the thickness of the solid region D_s yielding:

$$D_s + \frac{h_n}{2\lambda_s} D_s^2 = \frac{t_{disch}\, h_n}{\rho \Delta H} (T_m - T_n) \quad (4.19)$$

where t_{disch} is the time at which the discharging process takes place during the night and T_n is the average room temperature at night.

A PCM wall can effectively work when it melts completely during the daytime and freezes in the nighttime, where

$$D_l = D_s = D_{opt} \quad (4.20)$$

$$t_{ch} + t_{disch} = 24\ hours \quad (4.21)$$

The energy stored per unit of area at $t = t_{ch}$ is

$$E_{stor} = \rho \Delta H D_l \quad (4.22)$$

Assuming that the differences in conductivities and in the heat transfer coefficients are negligible,

$$h = h_d = h_n \quad (4.23)$$

$$\lambda_l = \lambda_s \quad (4.24)$$

and solving Eqs. (4.18) and (4.19) gives the optimal thickness of the co-oil PCM layer (m), D_{opt}:

$$D_{opt} = \frac{\lambda}{h}\left\{\left[1 + \frac{2h^2\, t_{disch}}{\rho \Delta H \lambda}(T_m - T_n)\right]^{1/2} - 1\right\} \tag{4.25}$$

Recall our main assumption that the heat transfer is controlled by conduction, and assuming a very small Nusselt number

$$Nu = \frac{hD}{\lambda} << 1 \tag{4.26}$$

and using the binomial expansion theorem, Eq. (4.25) can be further simplified as:

$$D_{opt} \approx \frac{h\, t_{disch}}{\rho \Delta H}(T_m - T_n) \tag{4.27}$$

4.4 Results and Discussion

4.4.1 Experimental Investigation

Five experimental cases were considered according to the window orientation (east, west, north, south, and south-facing window equipped with co-oil PCM). In all cases, the windows of the two test rooms were arranged to the same orientation, and the readings were collected at the same outdoor weather conditions. In the first four cases, the walls and ceiling of the test building were covered with co-oil PCM and each case differed from the other only by the orientation of the window. In the fifth case, the two buildings were directed to the south, and the test building window was equipped with co-oil PCM in addition to the walls and ceilings as shown in Figure 4.1.

A discussion of the five cases is provided in the following sections. To analyze the experimental data, the following parameters are defined:

T_H^E: the highest outside environmental temperature.

T_L^E: the lowest outside environmental temperature.

ΔT_H : The difference between the highest control building temperature, T_H^{CB}, reached during a 48-hour period and that of the test building, T_H^{TB}:

$$\Delta T_H = T_H^{CB} - T_H^{TB} \tag{4.28}$$

ΔT_L: The difference between the lowest test building temperature, T_L^{TB}, reached during a 48-hour period and that of the control building, T_L^{CB}:

$$\Delta T_L = T_L^{TB} - T_L^{CB} \tag{4.29}$$

ΔT_{DN}^{TB}: The difference between the highest and the lowest test building temperatures reached during a 48-hour period. This parameter gives the difference in temperature between daytime and night:

$$\Delta T_{DN}^{TB} = T_H^{TB} - T_L^{TB} \tag{4.30}$$

ΔT_{DN}^{CB}: The difference between the highest and the lowest control building temperatures reached during a 48-hour period:

$$\Delta T_{DN}^{CB} = T_H^{CB} - T_L^{CB} \tag{4.31}$$

ΔT_{DN}: The difference between the temperature variation of the two buildings. This parameter represents the influence of the integration of a PCM on the variation of indoor temperature during a complete day:

$$\Delta T_{DN} = \Delta T_{DN}^{TB} - \Delta T_{DN}^{CB} \tag{4.32}$$

φ_H^E: the highest outside relative humidity.

φ_L^E: the lowest outside relative humidity.

$\Delta\varphi_H$: The difference between the highest control building relative humidity, φ_H^{CB}, reached during a 48-hour period and that of the test building, φ_H^{TB}:

$$\Delta\varphi_H = \varphi_H^{CB} - \varphi_H^{TB} \tag{4.33}$$

$\Delta\varphi_L$: The difference between the lowest test building relative humidity, φ_L^{TB}, reached during a 48-hour period and that of the control building, φ_L^{CB}:

$$\Delta\varphi_L = \varphi_L^{TB} - \varphi_L^{CB} \tag{4.34}$$

$\Delta\varphi_{DN}^{TB}$: The difference between the highest and the lowest test building relative humidity reached during a 48-hour period. This parameter gives the difference in relative humidity between daytime and night:

$$\Delta\varphi_{DN}^{TB} = \varphi_{H}^{TB} - \varphi_{L}^{TB} \tag{4.35}$$

$\Delta\varphi_{DN}^{CB}$: The difference between the highest and the lowest control building relative humidity reached during a 48-hour period:

$$\varphi_{DN}^{CB} = \varphi_{H}^{CB} - \varphi_{L}^{CB} \tag{4.36}$$

$\Delta\varphi_{DN}$: The difference between the relative humidity variation of the two buildings. This parameter represents the effect of the integration of the PCM on the variation of relative humidity during a complete day:

$$\Delta\varphi_{DN} = \Delta\varphi_{DN}^{TB} - \Delta\varphi_{DN}^{CB} \tag{4.37}$$

4.4.1.1 West-facing window case

The experiment for the west-facing window was performed for 48 hours from February 20 to February 22, 2018. The 48-hour ambient temperature and solar irradiance along with the indoor temperature of the two buildings are shown in Figure 4.3(a). On February 21, it can be noted that the temperatures of the control building reach their maximum values between the period of 9:30 a.m. to 4 p.m., whereas maximum temperatures of the test building occur from 1:00 p.m. to 4:30 p.m. This lag in response (about 2 hours) demonstrates the anticipated effect of adding co-oil PCM to lower or delay the heat gain by the indoor environment. Also, the experimental data show that the highest reduction of the indoor temperature of the test building over the control building was 4.3℃ at 10 a.m. This proves that when the temperature exceeded the melting point ($\sim$23℃), the latent heat was introduced and started absorbing the gained heat energy by the building. However, the maximum temperature wasn't reduced, from which it can be deduced that the co-oil PCM wasn't completely melted and the sensible heat contributed in increasing the temperature of the building.

Table 4.2 shows the obtained temperatures (T_H^{CB}, T_H^{TB}, T_H^E, T_L^{CB}, T_L^{TB}, T_L^E) of the two buildings and the environment. It is clear that the variation, ΔT_{DN}^{TB}, of the indoor air temperature of the test building during the day is lower than that of the control building, ΔT_{DN}^{CB}, by 0.1-4.2°C (ΔT_{DN} varies from 0.1°C to 4.2°C).

Taken together, it is deduced that a co-oil PCM room with a west-facing window can lower the variation of the indoor temperature and delay the response in the temperature change.

However, the maximum temperature was increased by the sensible heat because of the partial melting of the co-oil PCM.

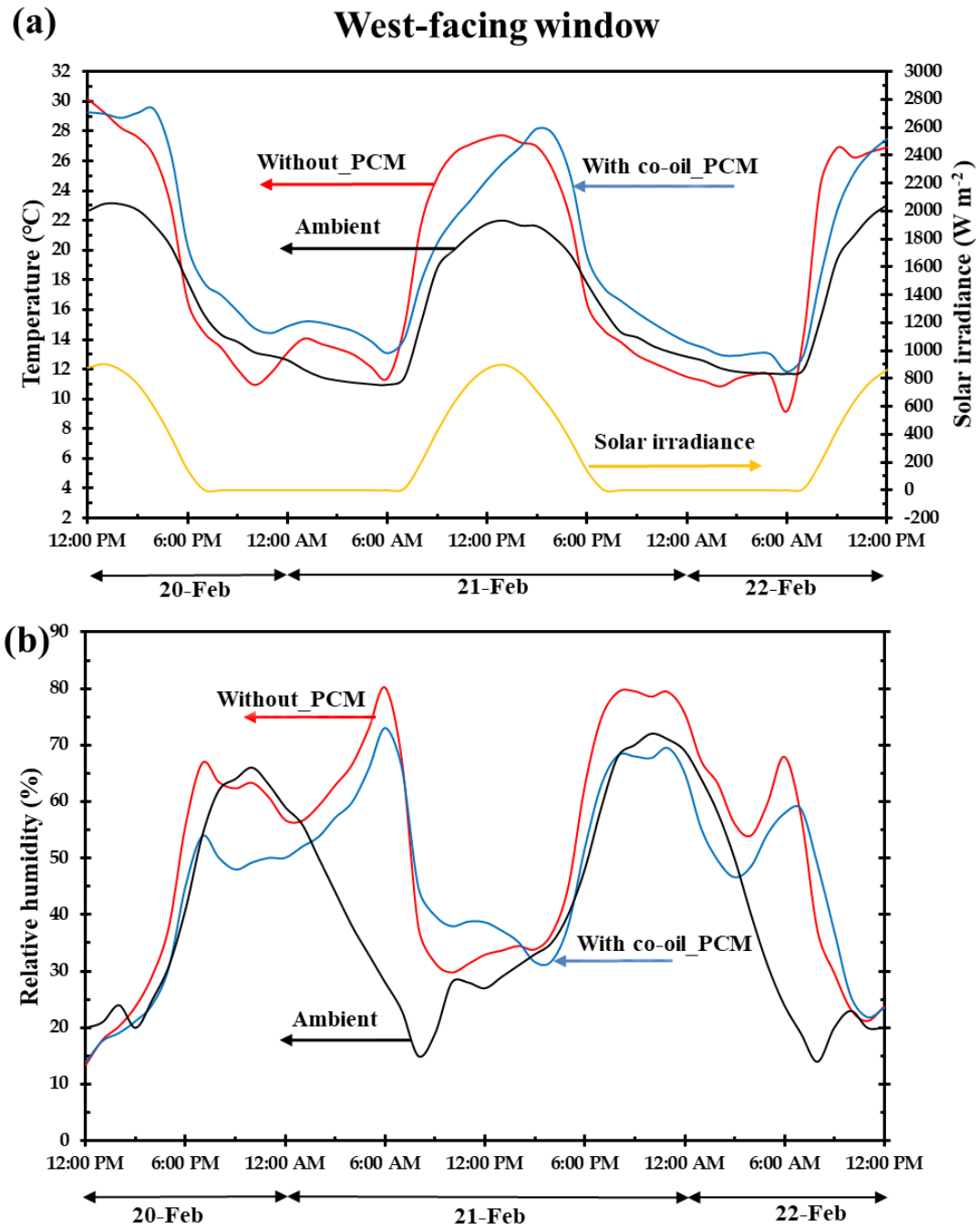

Figure 4.3: Hourly Variation of (a) Temperature and Solar Irradiance and (b) Relative Humidity for West-facing Window.

Table 4.2: Highest and Lowest Temperature for the Five Experimental Cases.

Date	Environment (°C)		Without PCM (°C)			With PCM (°C)		
	T_H^E	T_L^E	T_H^{CB}	T_L^{CB}	ΔT_{DN}^{CB}	T_H^{TB}	T_L^{TB}	ΔT_{DN}^{TB}
Window oriented to the west								
20-Feb-2018	22.7	12.62	30.1	10.9	19.2	29.4	14.4	15
21-Feb-2018	21.9	11	27.7	11.4	16.3	27.7	13.1	14.6
22-Feb-2018	23.1	11.7	26.9	11.1	15.8	27.5	11.8	15.7
Window oriented to the north								
25-Feb-2018	22.9	12.4	26.6	11.3	15.3	27.4	13.2	14.2
26-Feb-2018	23.4	10.3	24.3	8.2	16.1	24.9	9.4	15.5
27-Feb-2018	22.6	10.1	26.7	9	17.7	26.3	9.9	16.4
Window oriented to the east								
28-Feb-2018	23.7	12.4	30.5	12.5	18	29.8	14.1	15.7
1-Mar-2018	21.9	9.9	27.2	10.8	16.4	26.8	12.6	14.2
2-Mar-2018	19.3	7.8	26.8	7.4	19.4	24.8	8.9	15.9
Window oriented to the south								
5-Mar-2018	22.2	14.1	35.1	11.3	23.8	31	13.8	17.2
6-Mar-2018	24.2	11.7	34.6	6.7	27.9	30.9	8	22.9
7-Mar-2018	23.7	7.5	31.3	8.3	23	29	10.4	18.6
PCM window oriented to the south								
11-Mar-2018	23	13	28.2	10.4	17.8	26.1	13.8	12.3
12-Mar-2018	22.1	9.9	32	7.9	24.1	24.5	9.9	14.6
13-Mar-2018	21.6	8.5	33.4	8.1	25.3	27.6	5.4	22.2

Relative humidity has a definite effect on thermal comfort in buildings and it changes together with temperature. Since the PCM influences the indoor temperature, it can be deduced that it could have a corresponding influence on the relative humidity inside the building as well. Figure 4.3(b) shows the evolution of the relative humidity of the test building, the control building, and the ambient over a 48-hour period. Table 4.3 presents the percentages of the relative humidity of the two rooms and the ambient (φ_H^{CB}, $\varphi_H^{TB}, \varphi_H^E, \varphi_L^{CB}$, $\varphi_L^{TB}, \varphi_L^E$). It can be noted that the trends of the indoor humidity are similar; however, the highest values and variation between daytime and nighttime ($\Delta\varphi_{DN}^{TB}$ and $\Delta\varphi_{DN}^{CB}$) are different. As detailed in Table 4.3, it is clear that in comparison with the control building, the highest indoor humidity of the test building, φ_H^{TB}, was reduced by 7.1-16.9% (the value of the parameter $\Delta\varphi_H$). In addition, the indoor relative humidity difference for the test building, $\Delta\varphi_{DN}^{TB}$, was 8.9-17.4% lower than that of the control building, $\Delta\varphi_{DN}^{CB}$. As mentioned earlier, the effect of co-oil PCM on indoor temperature may also extend to affect the relative humidity. Thus, the influence of partial melting of co-oil PCM can be noted in decreasing the relative humidity more at 3 p.m. when the temperature increased because of sensible heating. To summarize, the integration of the co-oil PCM with lightweight buildings improves the air quality (i.e., temperature and relative humidity) and consequently yields a healthier indoor environment.

4.4.1.2 North-facing window case

The evolution over 48 hours of the indoor temperature of the two buildings, the ambient temperature and the solar irradiance are presented in Figure 4.4(a). It is clear that the trends of the outdoor and indoor temperatures are basically the same, in contrast to the results for

the west-facing window. We can deduce that diurnal heat storage was not effectively achieved, and this could be a consequence of the lack of transient solar radiation to the test building due to the window orientation. This lack of transient solar radiation resulted in a partial melting of the co-oil PCM and hence no temperature reduction was noted.

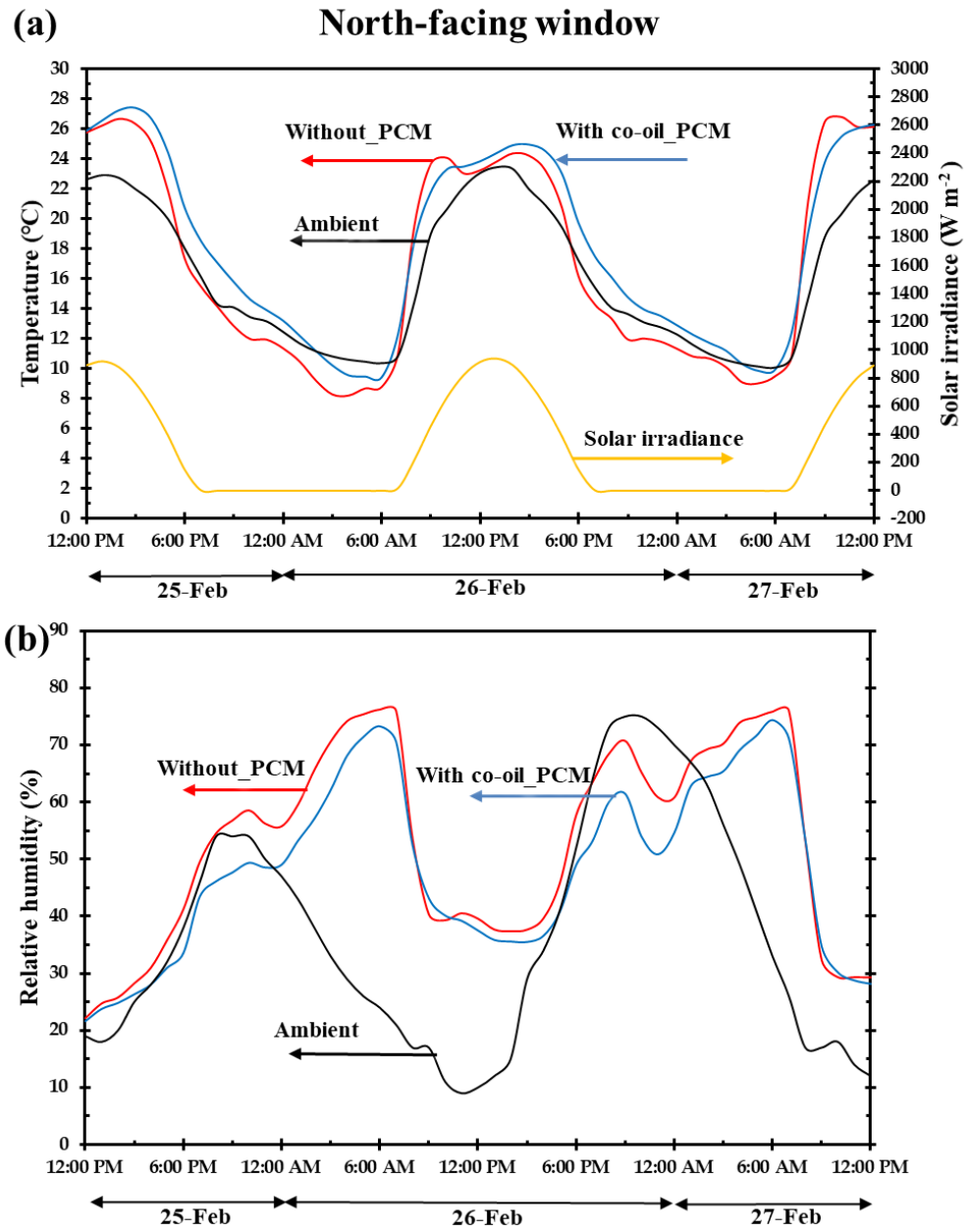

Figure 4.4: Hourly Variation of (a) Temperature and Solar Irradiance and (b) Relative Humidity for North-facing Window.

The variation of the highest and the lowest values of the indoor air temperature for the buildings, for all window orientations, are presented in Table 4.2. It is apparent that the test building reduced the indoor temperature difference by 0.6-1.3°C (value of ΔT_{DN}) over the control building; however, in comparison to the west-facing window case, this reduction was not significant.

The time-dependent history of the ambient and indoor relative humidity is shown in Figure 4.4(b). It can be noted that the indoor humidity trends of the two buildings are almost the same; however, the highest values and the range of variation are different. As highlighted in Table 4.3, the test building reduced the highest indoor humidity, φ_H^{TB}, by 1.6-9.2% (values of $\Delta\varphi_H$) over that of the control building, φ_H^{CB}. It is worthwhile to mention here that the effect of the test building on the indoor relative humidity difference, $\Delta\varphi_{DN}$, was more significant than its influence on the indoor temperature difference, ΔT_{DN}.

4.4.1.3 East-facing window case

The 48-hour time history of the indoor air temperature of the two buildings, the ambient temperature, and solar irradiance are shown in Figure 4.5(a). As seen, the evolutions of the indoor air temperatures of the two buildings were similar; however, the highest and the lowest values were different. Furthermore, Figure 4.5(a) and Table 4.2 show that the indoor air temperature difference for the test building, ΔT_{DN}^{TB}, was 2.2-3.5°C lower than that in the control building, ΔT_{DN}^{CB}. The primary cause of varying temperature inside the room is the direct transmitted solar radiation. Thus, it can be noticed that the range of variation for the east-facing window case is relatively higher when compared to the north-facing window case.

Figure 4.5(b) shows that the evolutions of the indoor relative humidity of the two buildings were basically the same. Table 4.3 indicates that the maximum relative humidity of the test building, φ_H^{TB}, is 2.5-7.6 % lower compared to that of control building, φ_H^{CB}.

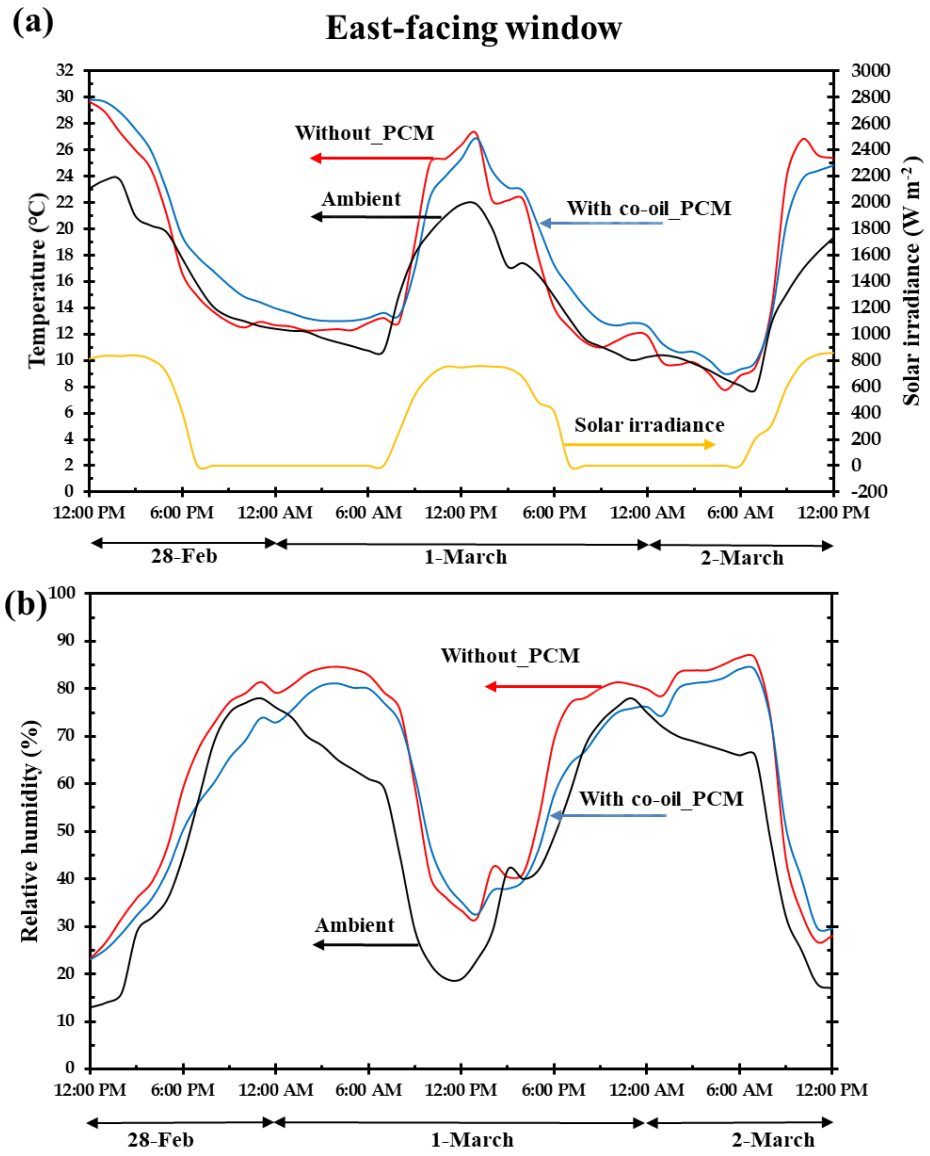

Figure 4.5: Hourly Variation of (a) Temperature and Solar Irradiance and (b) Relative Humidity for East-facing Window.

Table 4.3: Highest and Lowest Relative Humidity for the Five Experimental Cases.

Date	Environment (%)		Without PCM (%)			With PCM (%)		
	φ_H^E	φ_L^E	φ_H^{CB}	φ_L^{CB}	$\Delta\varphi_{DN}^{CB}$	φ_H^{TB}	φ_L^{TB}	$\Delta\varphi_{DN}^{TB}$
Window oriented to the west								
20-Feb-2018	66.1	20	66.9	13.4	53.5	50	13.9	36.1
21-Feb-2018	71.8	15.2	80.2	29.7	50.5	73.1	31.5	41.6
22-Feb-2018	64.3	14.2	67.3	21.1	46.2	57.9	21.8	36.1
Window oriented to the north								
25-Feb-2018	54.1	17.9	58.5	22.1	36.4	49.3	21.5	27.8
26-Feb-2018	74.9	9.1	76.1	37.3	38.8	73.2	35.5	37.7
27-Feb-2018	66.9	12.2	75.9	29.3	46.6	74.3	28.1	46.2
Window oriented to the east								
28-Feb-2018	78.3	13.2	81.4	23.3	58.1	73.8	23.1	50.7
1-Mar-2018	77.8	18.7	84.6	31.7	52.9	81.1	32.5	48.6
2-Mar-2018	72.1	17.2	86.6	28.6	58	84.1	29.5	54.6
Window oriented to the south								
5-Mar-2018	63.2	18.2	82	31.4	50.6	79.5	33.6	45.9
6-Mar-2018	57.4	20.3	82.6	15.8	66.8	81.7	16.1	65.6
7-Mar-2018	43.4	10.2	82.1	8.5	73.6	79.5	8.5	71
PCM window oriented to the south								
11-Mar-2018	59.2	33.3	79.5	33.6	45.9	56.3	16.9	39.4
12-Mar-2018	63.4	18.3	81.8	16.1	65.7	62.8	26.6	36.2
13-Mar-2018	58.7	10.8	67.1	8.5	58.6	63.8	14.3	49.5

4.4.1.4 South-facing window case

Again, the 48-hour history of the ambient temperature, the solar irradiance and the indoor temperature of the two buildings are shown in Figure 4.6(a). For more clear analyses of these experimental data, we considered a complete day and divided it into three regions, AB, BC and CD, as shown in Figure 4.6(a). It is evident that for the region AB (from 6:30 a.m. to 2:00 p.m.), the temperatures of the two buildings and that of the ambient increase with the solar irradiance. Due to the greenhouse effect caused by the double-glazed window, it can be noted that the indoor temperatures of the two buildings are higher than the ambient temperature. The increasing indoor temperatures caused by the greenhouse effect were moderated by the co-oil PCM. Therefore, we can deduce that diurnal heat storage is effectively achieved when sufficient solar radiation transmits to a building which accordingly leads to an increase in the greenhouse effect. The most remarkable result in the AB region is that the highest reduction in the indoor temperature of the test building over the control building was 5.2°C at about 10:30 a.m. On the other hand, for the region CD (from 4:00 p.m. to 6:30 a.m.), due to the use of PCM, we note that the test building indoor temperature is higher than that of the control building. Also, Table 4.2 shows that the lowest indoor temperature, T_L^{TB}, is 1.3-2.5°C higher compared to the control building which suggests that the test building is discharging more heat to the indoor air during nighttime than the control building. This process is beneficial for lightweight buildings in such a climate region where the PCM layer is used as a storage medium during the daytime and recovers it at nighttime as an internal heat source. As seen in Table 4.2, for the test building, the south-facing window had an indoor temperature difference that was approximately twice that of the east-facing window case. Thus, it can be stated that the greatest reduction

in the highest indoor temperature is observed when the window orientation was to the south which in turn increased the incident solar radiation to the test building. This transmitted energy is stored as latent heat.

It is observed that directing the two buildings' windows to the south decreases the indoor relative humidity (Figure 4.6(b)). Also, the indoor relative humidity difference of the test building was reduced by 1.2-4.7% (Table 4.3) over that in the control building. However, this reduction was not high in comparison with that in other orientations. Based on the results here, it can be affirmed that the effect of the test building on the indoor relative humidity difference was much smaller than its influence on the indoor temperature difference

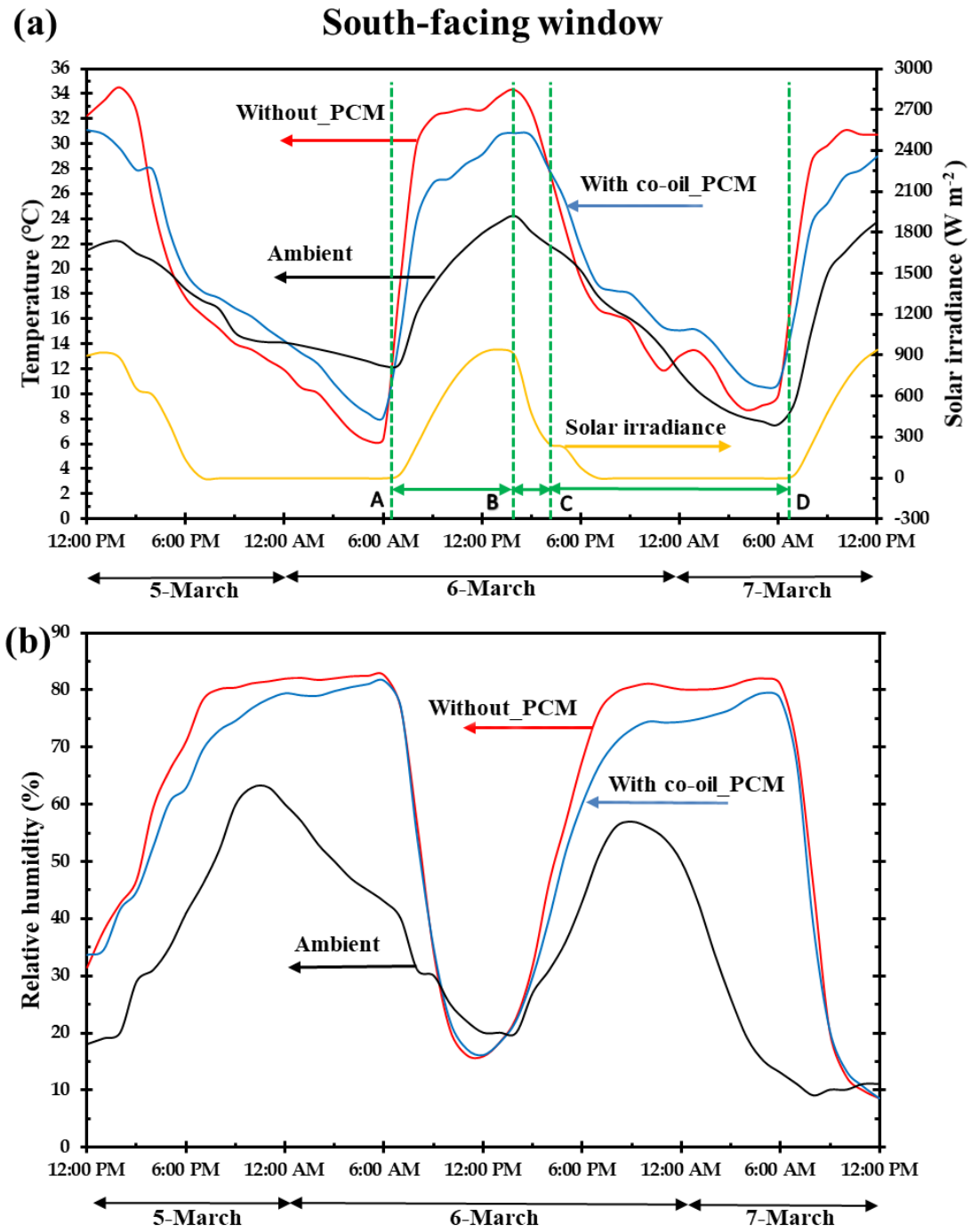

Figure 4.6: Hourly Variation of (a) Temperature and Solar Irradiance and (b) Relative Humidity for South-facing Window.

4.4.1.5 South-facing window equipped with co-oil PCM

A window equipped with PCM can block a relevant amount of solar irradiation from transmitting into the indoor environment. In this case, the south-facing window of the test building was itself equipped with co-oil PCM. The most striking result in this case is that the test building lowered the highest indoor temperature by up to 7.5°C (Figure 4.7(a)) over the control building at 12:15 p.m. on March 12, 2018. The indoor temperature difference for the test building was 3.1-9.5°C (Table 4.2) less than that in the control building. Moreover, the highest and the lowest indoor temperatures of the test building were 2.1-7.5°C (values of ΔT_H) lower and 2-3.4°C (values of ΔT_L) higher, respectively, in comparison with the control building. Thus, integrating co-oil PCM in the window trapped a large amount of incident solar radiation from transmitting to the building and consequently prevented increasing the indoor temperature. Therefore, it can be concluded that coating the test building's window with PCM has a clear influence on lowering the indoor temperature and improving comfort.

As seen in Figure 4.7(b), it is noted that the trends of the ambient and the indoor relative humidity of the test building over the 48 hours were similar. As shown in Table 4.3, it is apparent that the indoor relative humidity difference for the test building was 6.5-29.5% lower than that in the control building. Additionally, the highest indoor relative humidity of the test building was 3.3-23.2% lower when compared with that of the control building. Thus, the fifth case has the most significant effect on the indoor relative humidity compared to the other four cases. This indicates that the test building window equipped with PCM is the most effective case in reducing not only the indoor temperature but also the indoor

relative humidity. Therefore, it can be deduced that the benefits of minimizing the temperature fluctuation within the building are positively reflected on the relative humidity balance which consequently yields a healthier environment. Taken together, the results state that the task of the test building in modifying the indoor temperature and relative humidity was optimized when its window was equipped with PCM and there was a remarkable transmitted solar radiation during the daytime by directing its window to the south.

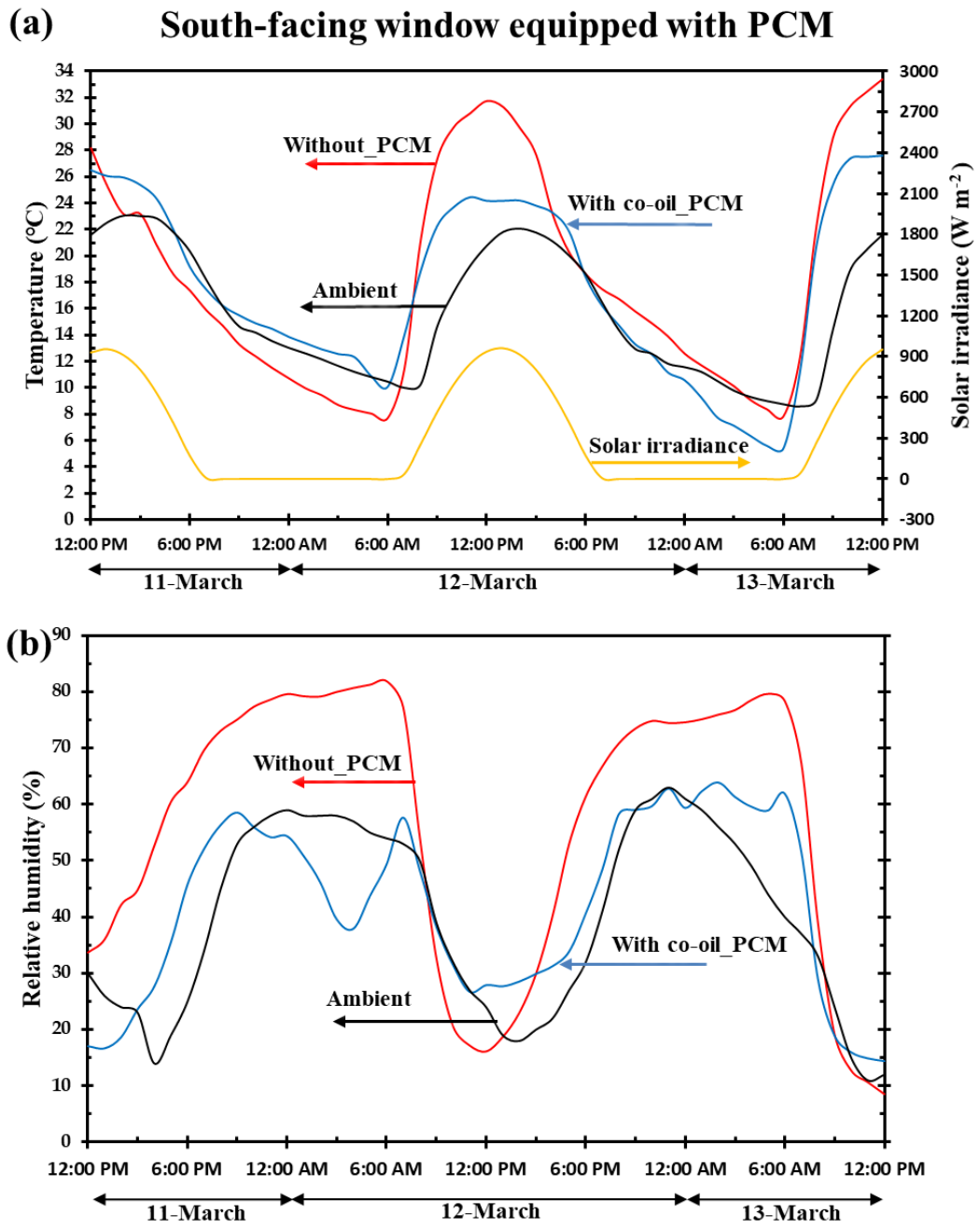

Figure 4.7: Hourly Variation of (a) Temperature and Solar Irradiance and (b) Relative Humidity for South-facing Window Equipped with PCM.

4.4.2 Numerical Results

To further investigate the thermal characteristics of lightweight buildings, two cases were simulated using the validated model (discussed below) to further specify the influence of co-oil PCM in lightweight buildings. The first case is a simulation of the control building with no co-oil PCM. This case shows the effect that the test building has on the indoor relative humidity and temperature when compared to the control building. The second case is a simulation of the test building with various co-oil PCM layer thicknesses. This case helps in determining the optimal thickness of the co-oil PCM layer. In these simulations, the windows were oriented to the south (i.e., the most effective orientation based on the experiments).

4.4.2.1 Numerical model validation

The measured and calculated indoor temperatures of the test and control buildings are shown in Figure 4.8. The continuous lines illustrate the experimental results while the dashed lines illustrate the numerical results. The maximum difference between the numerical prediction and experimental data is 3°C. This difference may have occurred because of the different values of the melting point between the simulations and the experiments. In the simulations, the melting point was set at 23°C, while in reality, the melting temperature varies within a range as shown in Table 4.1. However, the precision of the model is satisfactory for engineering applications.

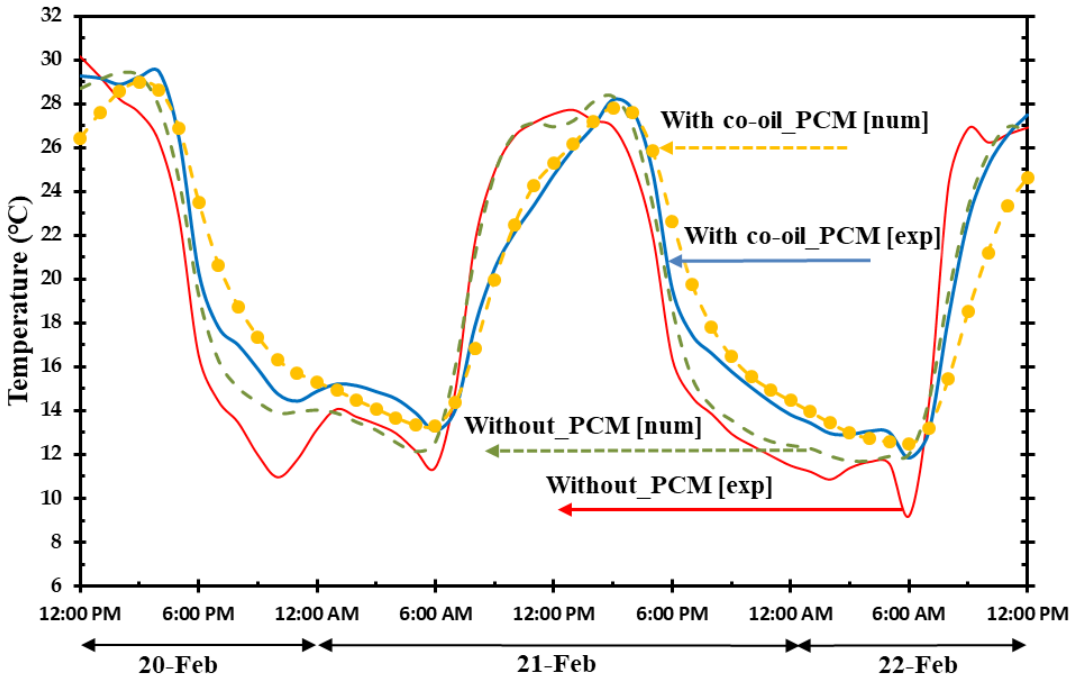

Figure 4.8: Validation of the Numerical Results.

4.4.2.2 Co-oil PCM impact on indoor temperature and relative humidity

Summer season:

In summer, three days were chosen from July 20 to July 23, 2018 to evaluate the effect of co-oil PCM on humidity and indoor temperature. The changes in indoor air temperature of the two simulated buildings along with the ambient temperature and solar irradiance are presented in Figure 4.9(a). It is apparent that the highest indoor temperature of the test model was reduced by up to 5.6°C over the control model at 10:00 a.m. on July 21. Further, the test model indoor temperature curve was pulled to the right representing a delayed response in indoor temperature change of about two hours compared to the control model. As was discussed earlier for the experiments, this delay response phenomenon proves the

effectiveness of co-oil PCM on storing the heat energy and eventually reducing the indoor temperature.

Table 4.4 shows that the indoor temperature's difference for the test model was 3.1-3.9°C lower than that in the control model. Overall, it is apparent that the test model is able to delay the response in temperature change and eventually reduce the indoor temperature.

On the other hand, it is noted that the indoor relative humidity trends of the two models were the same (Figure 4.9(b)). So, it can be deduced that the relative humidity of the two models increases during the summer season, and obviously the difference between them is minor.

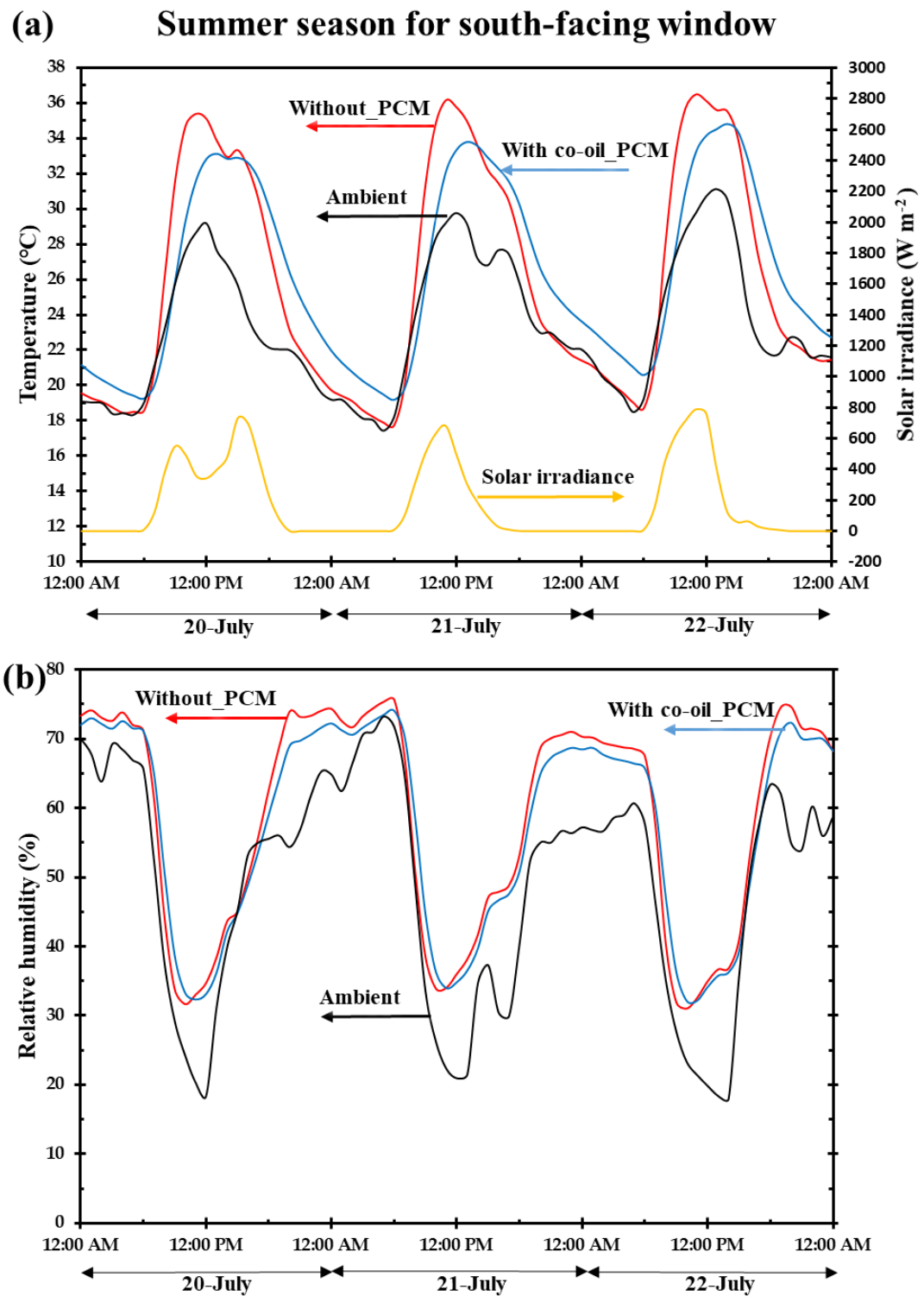

Figure 4.9: Hourly Variation of (a) Temperature and Solar Irradiance and (b) Relative Humidity During Summer Season for South-facing Window.

Winter season

In winter, three days from November 25 to November 28, 2018, were chosen to evaluate the effects of co-oil PCM on indoor temperature and relative humidity. The three days ambient temperature, solar irradiance and the indoor temperature of the two models are shown in Figure 4.10(a). It can be clearly seen that the highest temperatures for the two models were obtained during the same period. In addition, the highest reduction in indoor temperature for the test model was 4.8°C at about 10:00 a.m. on November 26. Thus, it can be deduced that although the test model had a clear influence on reducing the highest temperatures during the winter season, its functionality in lagging the response in temperature change was not as effective as noted during the summer season.

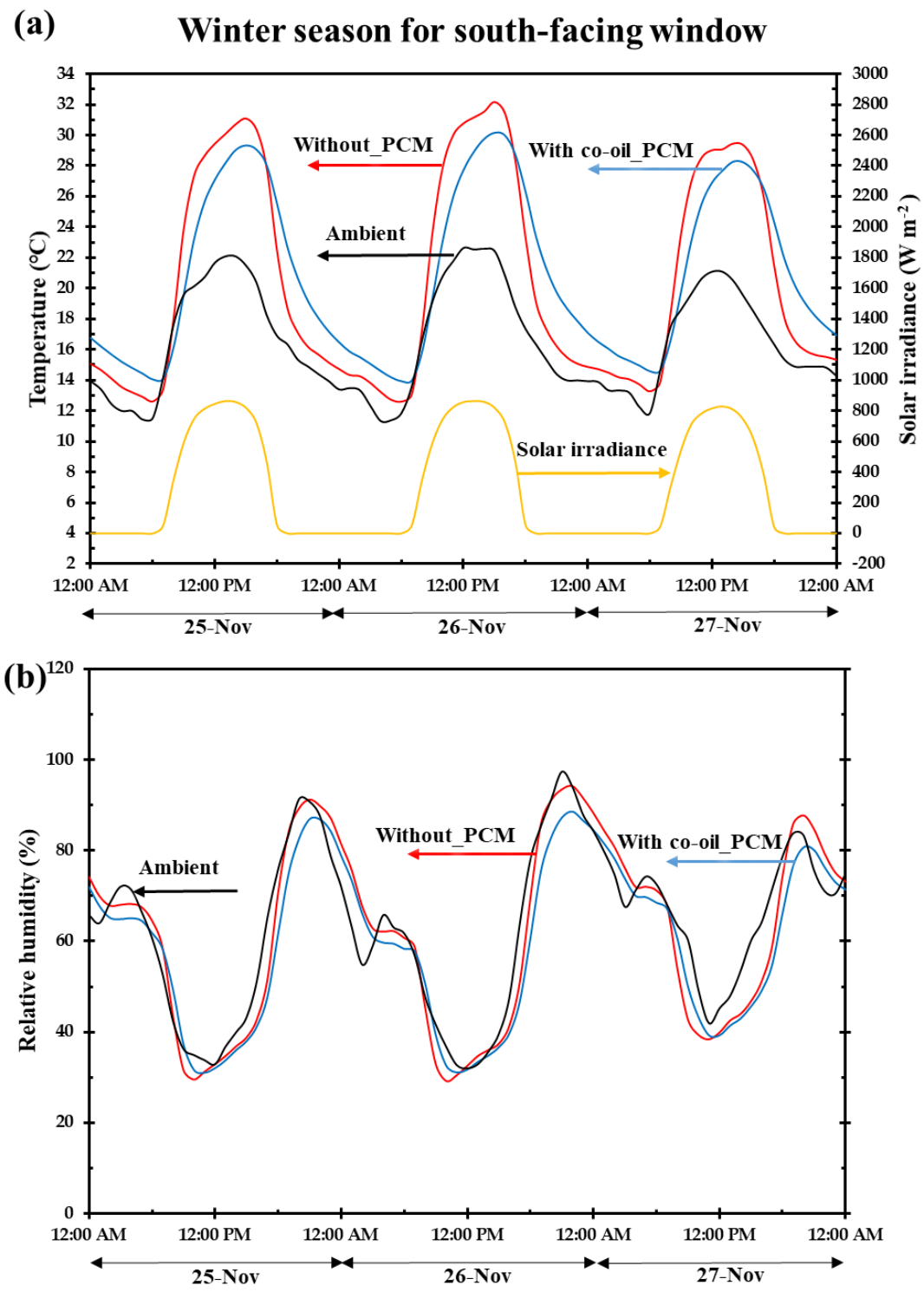

Figure 4.10: Hourly Variation of (a) Temperature and Solar Irradiance and (b) Relative Humidity During Winter Season for South-facing Window.

The highest and the lowest environmental temperatures as well as for the two models over the three days period are shown in Table 4.4. Since the lowest temperatures are of concern, the test model showed 1.3-1.4°C higher amounts than the control model. It can be seen that the test model raised the lowest indoor temperature by 4.2°C at about 7:00 p.m. on November 26. As reported previously, releasing heat inside the room during winter nights would be advantageous in lightweight envelopes in such a climate where heat stored during the day time can be discharged at nighttime. Therefore, it can be stated that the co-oil PCM is one solution to increase the indoor temperature at night time in the winter season when there is no heat source inside.

The hourly variation of the indoor relative humidity during the winter season, for a south-facing window and for three days, is shown in Figure 4.10(b). It is clear, from this figure, that the humidity trends for the two models are basically the same; however, the amplitude of variation and the peak values are different. It can be deduced that the relative humidity of the two models is clearly consistent with the ambient relative humidity during the winter season and the influence of the co-oil PCM is negligible.

Table 4.4: Highest and Lowest Temperatures for Summer and Winter Simulation Cases.

Date	Environment (°C)		Without PCM(°C)			With PCM (°C)		
	T_H^E	T_L^E	T_H^{CB}	T_L^{CB}	ΔT_{DN}^{CB}	T_H^{TB}	T_L^{TB}	ΔT_{DN}^{TB}
Summer season								
20-Jul-2018	29.1	18.3	35.4	18.4	17	33.1	19.2	13.9
21-Jul-2018	29.7	17.4	36.2	17.7	18.5	33.7	19.1	14.6
22-Jul-2018	31.1	18.5	36.1	18.7	17.4	34.8	21	13.8
Winter season								
25-Nov-2018	21.4	11.4	31.1	12.6	18.5	29.3	14	15.3
26-Nov-2018	22.6	11.3	32.2	12.6	19.6	30.1	13.9	16.2
27-Nov-2018	21.1	11.8	29.5	13.2	16.3	28.2	14.5	13.7

4.4.2.3 Effect of co-oil PCM layer thickness

Figure 4.11 shows the influence of co-oil PCM layer thickness on the average daytime temperature of the test model throughout the whole year. It can be clearly seen that there is no significant change in the average daytime indoor temperature beyond 4 cm thickness (a variation of 0.4°C when PCM thickness varies from 4 cm to 8 cm) and thus the use of a thickness more than this value is clearly inefficient. In addition, the optimum co-oil PCM thickness using Eq. (4.27) was found to be 4.6 cm (based on the thermal properties detailed in Table 4.1, and assuming a value of 8 W m^{-2} $°C^{-1}$ [102] for the heat transfer coefficient *h*) which validates the obtained numerical simulation result. Thus, it can be deduced that a co-oil PCM with a thickness more than 4 cm (for the given operating condition) may not melt completely and consequently represents a waste of material.

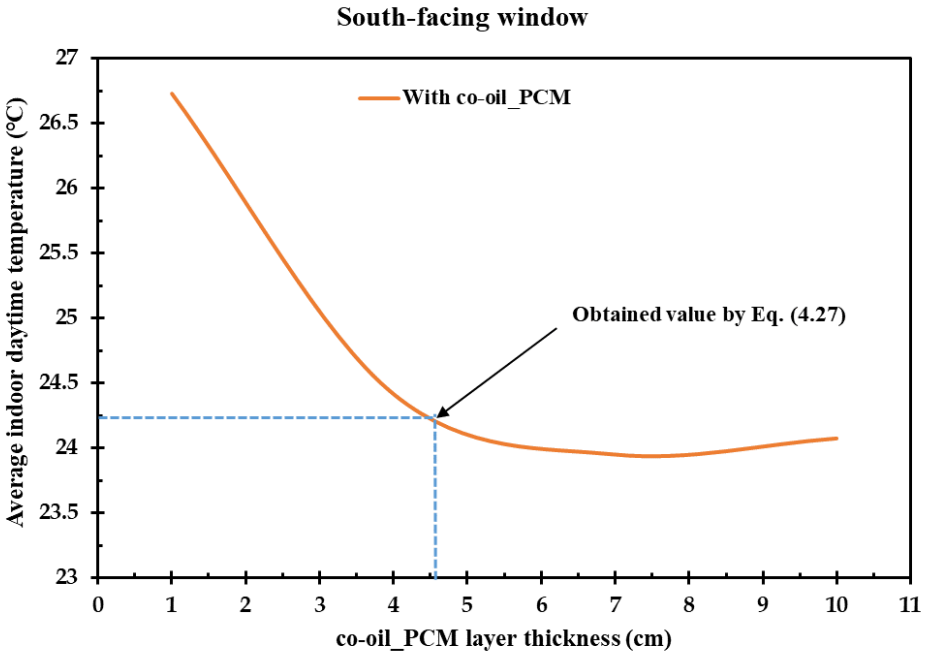

Figure 4.11: Influence of co-oil PCM Layer Thickness on Average Daytime Temperature of Retrofit Model.

4.5 Summary

Experimental investigations of the thermal performance of integrating co-oil PCM into unconditioned lightweight buildings were performed using twin side-by-side single-room buildings with double-glazed windows and under ambient weather conditions. Five cases were tested experimentally (east-facing window, west-facing window, north-facing window, south-facing window and south-facing window equipped with PCM). The obtained results are analyzed and the major conclusions are:

- Co-oil PCM effectively reduces the internal temperature of a lightweight building when the indoor average temperature during the day time is above the melting point by 1-5 °C in semi-arid regions.
- A south-facing window leads to a higher reduction in the indoor temperature as a result of transmitting relatively more solar energy, which contributes to complete melting of the co-oil PCM.
- A south-facing window equipped with PCM is the most effective case in reducing not only the indoor temperature but also the indoor relative humidity. While the highest reduction of the indoor temperature of the test building over the control building is 5.2°C in the south-facing window case, this value jumps to 7.2°C (44.2% more) when the window is equipped with PCM. Moreover, adding PCM to the window also improves the reduction in relative humidity by 20.6%.

In addition, by employing a simplified heat transfer analysis, an approximate relation for the optimal thickness of co-oil PCM layer is developed.

To investigate the thermal characteristics of the lightweight building equipped with PCM, the two buildings considered in the experiments were simulated numerically and the major conclusions are:

- In summer, the co-oil PCM delays the response in indoor temperature change by up to two hours.
- In winter, the co-oil PCM raised the lowest indoor temperature by up to 4.2°C which is advantageous in lightweight buildings during winter nights in such a climate.
- An optimal co-oil PCM layer thickness of 4 cm is found for obtaining the maximum heat storage capacity for the cases studied.

Based on both the experimental and the simulation results, it is concluded that co-oil PCM has the potential to be used in unconditioned lightweight buildings as TES to enhance their thermal mass and reduce the heat gain. This research can be considered to show the efficacy of integrating co-oil PCM into lightweight envelopes in semi-arid regions for reducing the heat gain as well as for improving the thermal comfort of the inhabitants.

5. CONCLUSIONS

Phase change material (PCM) is considered an attractive thermal management tool due to its high volumetric energy storage density and its capability to store/release energy at a relatively constant temperature. In this dissertation, three different thermal energy systems that incorporate PCMs were examined numerically and experimentally with the aim of enhancing the performance of these systems.

In Chapter 2, we proposed a new design that integrates a metal hydride (MH) reactor with a cylindrical sandwich bed packed with PCM (sodium nitrate-$NaNO_3$). The objective of this design is to improve the heat transfer rate and consequently reduce the time-duration of the hydrogenation and dehydrogenation processes in an MH-PCM storage system. A detailed numerical model was developed to predict the time evolution of the MH-PCM system temperature, hydrogen-reacted fraction and liquid fraction. The results showed that the time duration required for the hydrogenation and dehydrogenation processes was improved by 81.5% and 73%, respectively, for the new MH-PCM system design compared to the conventional MH-PCM jacket system that includes only a single PCM bed.

In Chapter 3, we proposed a novel design that consists of an MH reactor encircled by cascaded PCM beds. The objective here is to provide further improvement in the performance of MH-PCM sandwich system proposed in chapter 2 through the implementation of cascaded PCMs. The system performance was investigated numerically to predict the optimum storage capacity distribution ratio of the PCMs, the time evolution of the MH-PCM system temperature, equilibrium pressure, hydrogen-reacted fraction and

liquid fraction. Two PCMs were considered: one with a melting point of 591 K (PCM591) and another with a melting point of 580 K (PCM580). It was found that the optimum storage capacity ratio of the PCM591 to the total PCMs' storage capacity (ϕ_{PCM591}) is 40%, whereas the optimum storage capacity of the inner PCM beds to the total PCMs' storage capacity, with ϕ_{PCM591} = 40%, is 60%. The time duration required for the hydrogenation and dehydrogenation processes was improved by 26% and 51%, respectively, for the proposed cascaded MH-PCM sandwich design compared to the proposed design in chapter 2. To sum up, the cascaded MH-PCM sandwich design appears to significantly improve the performance of such systems.

In Chapter 4, organic coconut oil PCM (co-oil PCM) was tested experimentally and numerically for the first time in building applications. Twin side-by-side single-room buildings (with and without PCM) were constructed and studied experimentally under ambient weather conditions in a semi-arid region. Furthermore, numerical simulation of the buildings was carried out to evaluate the contribution of the co-oil to their thermal performance and to determine the effect of the co-oil layer thickness on the heat storage capacity. Moreover, by employing a simplified heat transfer analysis, an approximate relation for the optimal thickness of co-oil PCM layer was developed. Experimental and numerical results show that co-oil PCM can be a promising solution to improve the indoor thermal environment. It was found that with a south-facing window equipped with co-oil PCM, the indoor temperature is lowered by 23.8% compared to the case without PCM. In addition, the mathematical and numerical model showed that an optimal co-oil PCM layer thickness of ~4 cm was found to achieve the maximum heat storage capacity.

REFERENCES

[1] H. Nazir, M. Batool, F.J. Bolivar Osorio, M. Isaza-Ruiz, X. Xu, K. Vignarooban, P. Phelan, Inamuddin, A.M. Kannan, Recent developments in phase change materials for energy storage applications: A review, Int. J. Heat Mass Transf. 129 (2019) 491–523. doi:10.1016/j.ijheatmasstransfer.2018.09.126.

[2] U. Pelay, L. Luo, Y. Fan, D. Stitou, M. Rood, Thermal energy storage systems for concentrated solar power plants, Renew. Sustain. Energy Rev. 79 (2017) 82–100. doi:10.1016/j.rser.2017.03.139.

[3] C.A. Chung, S.W. Yang, C.Y. Yang, C.W. Hsu, P.Y. Chiu, Experimental study on the hydrogen charge and discharge rates of metal hydride tanks using heat pipes to enhance heat transfer, Appl. Energy. 103 (2013) 581–587. doi:10.1016/j.apenergy.2012.10.024.

[4] C. Corgnale, B. Hardy, T. Motyka, R. Zidan, Metal hydride based thermal energy storage system requirements for high performance concentrating solar power plants, Int. J. Hydrogen Energy. 41 (2016) 20217–20230. doi:10.1016/j.ijhydene.2016.09.108.

[5] H. Akeiber, P. Nejat, M.Z.A. Majid, M.A. Wahid, F. Jomehzadeh, I. Zeynali Famileh, J.K. Calautit, B.R. Hughes, S.A. Zaki, A review on phase change material (PCM) for sustainable passive cooling in building envelopes, Renew. Sustain. Energy Rev. 60 (2016) 1470–1497. doi:10.1016/j.rser.2016.03.036.

[6] R. Ji, Z. Zou, M. Chen, Y. Zheng, S. Qu, Numerical assessing energy performance for building envelopes with phase change material, Int. J. Energy Res. 43 (2019) 6222–6232. doi:10.1002/er.4293.

[7] R. Ji, Y. Zheng, Z. Zou, S. Wei, S. Qu, Climate applicability study of building envelopes containing phase change materials, Int. J. Energy Res. 43 (2019) 7397–7408. doi:10.1002/er.4772.

[8] L.F. Cabeza, Advances in Thermal Energy Storage Systems, 1st ed. Vo, Woodhead, 2014. web.

[9] P. Muthukumar, A. Kumar, N.N. Raju, K. Malleswararao, M.M. Rahman, A critical review on design aspects and developmental status of metal hydride based thermal machines, Int. J. Hydrogen Energy. 43 (2018) 17753–17779. doi:10.1016/j.ijhydene.2018.07.157.

[10] J. Sunku Prasad, P. Muthukumar, F. Desai, D.N. Basu, M.M. Rahman, A critical review of high-temperature reversible thermochemical energy storage systems, Appl. Energy. 254 (2019) 113733. doi:10.1016/j.apenergy.2019.113733.

[11] K. Manickam, P. Mistry, G. Walker, D. Grant, C.E. Buckley, T.D. Humphries, M. Paskevicius, T. Jensen, R. Albert, K. Peinecke, M. Felderhoff, Future perspectives of thermal energy storage with metal hydrides, Int. J. Hydrogen Energy. 44 (2019) 7738–7745. doi:10.1016/j.ijhydene.2018.12.011.

[12] Q. Luo, Y. Guo, B. Liu, Y. Feng, J. Zhang, Q. Li, K. Chou, Thermodynamics and kinetics of phase transformation in rare earth–magnesium alloys: A critical review, J. Mater. Sci. Technol. 44 (2020) 171–190. doi:10.1016/j.jmst.2020.01.022.

[13] W. Zhao, Y. Yang, Z. Bao, D. Yan, Z. Zhu, Methods for measuring the effective thermal conductivity of metal hydride beds: A review, Int. J. Hydrogen Energy. 45 (2020) 6680–6700. doi:10.1016/j.ijhydene.2019.12.185.

[14] X. Lin, D. Sun, S. Chen, Q. Zhu, H. Leng, Q. Li, Numerical analysis on pulverization and self-densification for hydrogen storage performance of a metal hydride tank, Appl. Therm. Eng. 161 (2019) 114129. doi:10.1016/j.applthermaleng.2019.114129.

[15] X. Lin, Q. Zhu, H. Leng, H. Yang, T. Lyu, Q. Li, Numerical analysis of the effects of particle radius and porosity on hydrogen absorption performances in metal hydride tank, Appl. Energy. 250 (2019) 1065–1072. doi:10.1016/j.apenergy.2019.04.181.

[16] G. Hermosilla-Lara, G. Momen, P.H. Marty, B. Le Neindre, K. Hassouni, Hydrogen storage by adsorption on activated carbon: Investigation of the thermal effects during the charging process, Int. J. Hydrogen Energy. 32 (2007) 1542–1553. doi:10.1016/j.ijhydene.2006.10.048.

[17] B. Delhomme, P. De Rango, P. Marty, M. Bacia, B. Zawilski, C. Raufast, S. Miraglia, D. Fruchart, Large scale magnesium hydride tank coupled with an external heat source, Int. J. Hydrogen Energy. 37 (2012) 9103–9111. doi:10.1016/j.ijhydene.2012.03.018.

[18] C.A. Chung, C.J. Ho, Thermal-fluid behavior of the hydriding and dehydriding processes in a metal hydride hydrogen storage canister, Int. J. Hydrogen Energy. 34 (2009) 4351–4364. doi:10.1016/j.ijhydene.2009.03.028.

[19] A. Chaise, P. De Rango, P. Marty, D. Fruchart, Experimental and numerical study of a magnesium hydride tank, Int. J. Hydrogen Energy. 35 (2010) 6311–6322.

doi:10.1016/j.ijhydene.2010.03.057.

[20] J. Yao, P. Zhu, C. Qian, U. Hamidullah, S. Kurko, F. Yang, Z. Zhang, Z. Wu, Study of an autothermal-equilibrium metal hydride reactor by reaction heat recovery as hydrogen source for the application of fuel cell power system, Energy Convers. Manag. 213 (2020) 112864. doi:10.1016/j.enconman.2020.112864.

[21] M. Gambini, T. Stilo, M. Vellini, Hydrogen storage systems for fuel cells: Comparison between high and low-temperature metal hydrides, Int. J. Hydrogen Energy. 44 (2019) 15118–15134. doi:10.1016/j.ijhydene.2019.04.083.

[22] M. Paskevicius, D.A. Sheppard, K. Williamson, C.E. Buckley, Metal hydride thermal heat storage prototype for concentrating solar thermal power, Energy. 88 (2015) 469–477. doi:10.1016/j.energy.2015.05.068.

[23] A. d'Entremont, C. Corgnale, M. Sulic, B. Hardy, R. Zidan, T. Motyka, Modeling of a thermal energy storage system based on coupled metal hydrides (magnesium iron – sodium alanate) for concentrating solar power plants, Int. J. Hydrogen Energy. 42 (2017) 22518–22529. doi:10.1016/j.ijhydene.2017.04.231.

[24] A. d'Entremont, C. Corgnale, B. Hardy, R. Zidan, Simulation of high temperature thermal energy storage system based on coupled metal hydrides for solar driven steam power plants, Int. J. Hydrogen Energy. 43 (2018) 817–830. doi:10.1016/j.ijhydene.2017.11.100.

[25] K. Malleswararao, A. N, S. Srinivasa Murthy, P. Dutta, Performance prediction of a coupled metal hydride based thermal energy storage system, Int. J. Hydrogen Energy. (2020). doi:10.1016/j.ijhydene.2020.03.251.

[26] C. Corgnale, B. Hardy, T. Motyka, R. Zidan, J. Teprovich, B. Peters, Screening analysis of metal hydride based thermal energy storage systems for concentrating solar power plants, Renew. Sustain. Energy Rev. 38 (2014) 821–833. doi:10.1016/j.rser.2014.07.049.

[27] F. Askri, A. Miled, S. Mellouli, H. Ben Mâad, Numerical investigation of high temperature metal hydride water pumping system, Int. J. Hydrogen Energy. 44 (2019) 16777–16792. doi:10.1016/j.ijhydene.2019.04.263.

[28] A. Miled, S. Mellouli, H. Ben Maad, F. Askri, Improvement of the performance of metal hydride pump by using phase change heat exchanger, Int. J. Hydrogen Energy. 42 (2017) 26343–26361. doi:10.1016/j.ijhydene.2017.08.118.

[29] S.N. Nyamsi, F. Yang, Z. Zhang, An optimization study on the finned tube heat exchanger used in hydride hydrogen storage system - Analytical method and numerical simulation, Int. J. Hydrogen Energy. 37 (2012) 16078–16092. doi:10.1016/j.ijhydene.2012.08.074.

[30] F. Askri, M. Ben Salah, A. Jemni, S. Ben Nasrallah, Optimization of hydrogen storage in metal-hydride tanks, Int. J. Hydrogen Energy. 34 (2009) 897–905. doi:10.1016/j.ijhydene.2008.11.021.

[31] B.D. MacDonald, A.M. Rowe, Impacts of external heat transfer enhancements on metal hydride storage tanks, Int. J. Hydrogen Energy. 31 (2006) 1721–1731. doi:10.1016/j.ijhydene.2006.01.007.

[32] S. Mellouli, H. Dhaou, F. Askri, A. Jemni, S. Ben Nasrallah, Hydrogen storage in metal hydride tanks equipped with metal foam heat exchanger, Int. J. Hydrogen Energy. 34 (2009) 9393–9401. doi:10.1016/j.ijhydene.2009.09.043.

[33] J. Payá, M. Linder, R. Mertz, J.M. Corberán, Analysis and optimization of a metal hydride cooling system, Int. J. Hydrogen Energy. 36 (2011) 920–930. doi:10.1016/j.ijhydene.2010.08.112.

[34] Z. Bao, Z. Wu, S.N. Nyamsi, F. Yang, Z. Zhang, Three-dimensional modeling and sensitivity analysis of multi-tubular metal hydride reactors, Appl. Therm. Eng. 52 (2013) 97–108. doi:10.1016/j.applthermaleng.2012.11.023.

[35] F. Askri, M. Ben Salah, A. Jemni, S. Ben Nasrallah, Heat and mass transfer studies on metal-hydrogen reactor filled with MmNi4.6Fe0.4, Int. J. Hydrogen Energy. 34 (2009) 6705–6711. doi:10.1016/j.ijhydene.2009.06.069.

[36] Z. Bao, F. Yang, Z. Wu, X. Cao, Z. Zhang, Simulation studies on heat and mass transfer in high-temperature magnesium hydride reactors, Appl. Energy. 112 (2013) 1181–1189. doi:10.1016/j.apenergy.2013.04.053.

[37] Z. Bao, Performance investigation and optimization of metal hydride reactors for high temperature thermochemical heat storage, Int. J. Hydrogen Energy. 40 (2015) 5664–5676. doi:10.1016/j.ijhydene.2015.02.123.

[38] S. Mellouli, F. Askri, H. Dhaou, A. Jemni, S. Ben Nasrallah, Numerical simulation of heat and mass transfer in metal hydride hydrogen storage tanks for fuel cell vehicles, Int. J. Hydrogen Energy. 35 (2010) 1693–1705. doi:10.1016/j.ijhydene.2009.12.052.

[39] H. Dhaou, N. Ben Khedher, S. Mellouli, A. Souahlia, F. Askri, A. Jemni, S. Ben Nasrallah, Improvement of thermal performance of spiral heat exchanger on hydrogen storage by adding copper fins, Int. J. Therm. Sci. 50 (2011) 2536–2542. doi:10.1016/j.ijthermalsci.2011.05.016.

[40] S. Mellouli, F. Askri, H. Dhaou, A. Jemni, S.B.N. Ben Nasrallah, A novel design of a heat exchanger for a metal-hydrogen reactor, Int. J. Hydrogen Energy. 32 (2007) 3501–3507. doi:10.1016/j.ijhydene.2007.02.039.

[41] A. Chaise, P. de Rango, P. Marty, D. Fruchart, S. Miraglia, R. Olivès, S. Garrier, Enhancement of hydrogen sorption in magnesium hydride using expanded natural graphite, Int. J. Hydrogen Energy. 34 (2009) 8589–8596. doi:10.1016/j.ijhydene.2009.07.112.

[42] A.A. Rabienataj Darzi, H. Hassanzadeh Afrouzi, A. Moshfegh, M. Farhadi, Absorption and desorption of hydrogen in long metal hydride tank equipped with phase change material jacket, Int. J. Hydrogen Energy. 41 (2016) 9595–9610. doi:10.1016/j.ijhydene.2016.04.051.

[43] K.E. Elfeky, N. Ahmed, Q. Wang, Numerical comparison between single PCM and multi-stage PCM based high temperature thermal energy storage for CSP tower plants, Appl. Therm. Eng. 139 (2018) 609–622. doi:10.1016/j.applthermaleng.2018.04.122.

[44] T. Alqahtani, S. Mellouli, A. Bamasag, F. Askri, P. Phelan, Experimental and numerical assessment of using coconut oil as a phase-change material for unconditioned buildings, Int J Energy Res. (2020) 1–20. doi:10.1002/er.5176.

[45] L. Zhao, J. Luo, H. Wang, G. Song, G. Tang, Self-assembly fabrication of microencapsulated n-octadecane with natural silk fibroin shell for thermal-regulating textiles, Appl. Therm. Eng. 99 (2016) 495–501. doi:10.1016/j.applthermaleng.2015.12.111.

[46] M.H. Abokersh, M. El-Morsi, O. Sharaf, W. Abdelrahman, On-demand operation of a compact solar water heater based on U-pipe evacuated tube solar collector combined with phase change material, Sol. Energy. 155 (2017) 1130–1147. doi:10.1016/j.solener.2017.07.008.

[47] S. Garrier, B. Delhomme, P. De Rango, P. Marty, D. Fruchart, S. Miraglia, A new MgH2 tank concept using a phase-change material to store the heat of reaction, Int. J. Hydrogen Energy. 38 (2013) 9766–9771. doi:10.1016/j.ijhydene.2013.05.026.

[48] S. Mellouli, N. Ben Khedher, F. Askri, A. Jemni, S. Ben Nasrallah, Numerical analysis of metal hydride tank with phase change material, Appl. Therm. Eng. 90 (2015) 674–682. doi:10.1016/j.applthermaleng.2015.07.022.

[49] H. Ben Mâad, A. Miled, F. Askri, S. Ben Nasrallah, Numerical simulation of absorption-desorption cyclic processes for metal-hydrogen reactor with heat recovery using phase-change material, Appl. Therm. Eng. 96 (2016) 267–276. doi:10.1016/j.applthermaleng.2015.11.093.

[50] S. Mellouli, E. Abhilash, F. Askri, S. Ben Nasrallah, Integration of thermal energy storage unit in a metal hydride hydrogen storage tank, Appl. Therm. Eng. 102 (2016) 1185–1196. doi:10.1016/j.applthermaleng.2016.03.116.

[51] S. Mellouli, F. Askri, E. Abhilash, S. Ben Nasrallah, Impact of using a heat transfer fluid pipe in a metal hydride-phase change material tank, Appl. Therm. Eng. 113 (2017) 554–565. doi:10.1016/j.applthermaleng.2016.11.065.

[52] H. Ben Mâad, F. Askri, J. Virgone, S. Ben Nasrallah, Numerical study of high temperature metal-hydrogen reactor (Mg2Ni-H2) with heat reaction recovery using phase-change material during desorption, Appl. Therm. Eng. 140 (2018) 225–234. doi:10.1016/j.applthermaleng.2018.05.009.

[53] H. El Mghari, J. Huot, J. Xiao, Analysis of hydrogen storage performance of metal hydride reactor with phase change materials, Int. J. Hydrogen Energy. 44 (2019) 28893–28908. doi:10.1016/j.ijhydene.2019.09.090.

[54] S.N. Nyamsi, I. Tolj, M. Lototskyy, Metal hydride beds-phase change materials: Dual mode thermal energy storage for medium-high temperature industrialwaste heat recovery, Energies. 12 (2019). doi:10.3390/en12203949.

[55] L. Tong, J. Xiao, P. Bénard, R. Chahine, Thermal management of metal hydride hydrogen storage reservoir using phase change materials, Int. J. Hydrogen Energy. 44 (2019) 21055–21066. doi:10.1016/j.ijhydene.2019.03.127.

[56] T. Alqahtani, S. Mellouli, A. Bamasag, F. Askri, P.E. Phelan, Thermal performance analysis of a metal hydride reactor encircled by a phase change material sandwich bed, Int. J. Hydrog. Energy. (in press, (2020).

[57] S. Mellouli, F. Askri, H. Dhaou, A. Jemni, S. Ben Nasrallah, A study of the thermal behavior of a deformable metal-hydride bed, Int. J. Hydrogen Energy. 41 (2016) 1711–1724. doi:10.1016/j.ijhydene.2015.10.058.

[58] V.M.B. Nunes, M.J.V. Lourenço, F.J.V. Santos, C.A. Nieto De Castro, Viscosity of molten sodium nitrate, Int. J. Thermophys. 27 (2006) 1638–1649. doi:10.1007/s10765-006-0119-1.

[59] C.A. Chung, C.S. Lin, Prediction of hydrogen desorption performance of Mg2Ni hydride reactors, Int. J. Hydrogen Energy. 34 (2009) 9409–9423. doi:10.1016/j.ijhydene.2009.09.061.

[60] S. Mellouli, F. Askri, A. Edacherian, T. Alqahtani, S. Algarni, J. Abdelmajid, P. Phelan, Performance analysis of a thermal energy storage system based on paired metal hydrides for concentrating solar power plants, Appl. Therm. Eng. 144 (2018). doi:10.1016/j.applthermaleng.2018.09.014.

[61] A. Chaise, P. Marty, P. de Rango, D. Fruchart, A simple criterion for estimating the effect of pressure gradients during hydrogen absorption in a hydride reactor, Int. J. Heat Mass Transf. 52 (2009) 4564–4572. doi:10.1016/j.ijheatmasstransfer.2009.03.052.

[62] T. Alqahtani, S. Mellouli, F. Askri, P.E. Phelan, Performance analysis of a metal hydride-thermal energy storage system for concentrating solar power plants, ASTFE Digit. Libr. (2019) 1667–1676. doi:10.1615/TFEC2019.sol.027379.

[63] Y.B. Tao, Y.L. He, Effects of natural convection on latent heat storage performance of salt in a horizontal concentric tube, Appl. Energy. 143 (2015) 38–46. doi:10.1016/j.apenergy.2015.01.008.

[64] P. Muthukumar, M. Groll, Erratum: Metal hydride based heating and cooling systems: A review, Int. J. Hydrogen Energy. 35 (2010) 8816–8829. doi:10.1016/j.ijhydene.2010.04.087.

[65] F.S. Yang, G.X. Wang, Z.X. Zhang, V. Rudolph, Investigation on the influences of heat transfer enhancement measures in a thermally driven metal hydride heat pump, Int. J. Hydrogen Energy. 35 (2010) 9725–9735. doi:10.1016/j.ijhydene.2010.06.110.

[66] F.S. Yang, G.X. Wang, Z.X. Zhang, X.Y. Meng, V. Rudolph, Design of the metal hydride reactors - A review on the key technical issues, Int. J. Hydrogen Energy. 35 (2010) 3832–3840. doi:10.1016/j.ijhydene.2010.01.053.

[67] H. Wang, A.K. Prasad, S.G. Advani, Hydrogen storage system based on hydride materials incorporating a helical-coil heat exchanger, Int. J. Hydrogen Energy. 37 (2012) 14292–14299. doi:10.1016/j.ijhydene.2012.07.016.

[68] R. Elarem, T. Alqahtani, S. Mellouli, F. Askri, A. Edacherian, T. Vineet, I.A. Badruddin, J. Abdelmajid, A comprehensive review of heat transfer intensification methods for latent heat storage units, Energy Storage. (2020) 1–30. doi:10.1002/est2.127.

[69] J.N.W. Chiu, V. Martin, Multistage latent heat cold thermal energy storage design analysis, Appl. Energy. 112 (2013) 1438–1445. doi:10.1016/j.apenergy.2013.01.054.

[70] L. Yang, X. Zhang, G. Xu, Thermal performance of a solar storage packed bed using spherical capsules filled with PCM having different melting points, Energy Build. 68 (2014) 639–646. doi:10.1016/j.enbuild.2013.09.045.

[71] P. Wang, X. Wang, Y. Huang, C. Li, Z. Peng, Y. Ding, Thermal energy charging behaviour of a heat exchange device with a zigzag plate configuration containing multi-phase-change-materials (m-PCMs), Appl. Energy. 142 (2015) 328–336. doi:10.1016/j.apenergy.2014.12.050.

[72] S. Pincemin, R. Olives, X. Py, M. Christ, Highly conductive composites made of phase change materials and graphite for thermal storage, Sol. Energy Mater. Sol. Cells. 92 (2008) 603–613. doi:10.1016/j.solmat.2007.11.010.

[73] A. Sharma, V. V Tyagi, C.R. Chen, D. Buddhi, Review on thermal energy storage with phase change materials and applications, 13 (2009) 318–345. doi:10.1016/j.rser.2007.10.005.

[74] A.A.A. Abuelnuor, A.A.M. Omara, K.M. Saqr, I.H.I. Elhag, Improving indoor thermal comfort by using phase change materials: A review, Int. J. Energy Res. 42 (2018) 2084–2103. doi:10.1002/er.4000.

[75] K. Du, J. Calautit, Z. Wang, Y. Wu, H. Liu, A review of the applications of phase change materials in cooling, heating and power generation in different temperature ranges, Appl. Energy. 220 (2018) 242–273. doi:10.1016/j.apenergy.2018.03.005.

[76] I. Sarbu, A. Dorca, Review on heat transfer analysis in thermal energy storage using latent heat storage systems and phase change materials, Int. J. Energy Res. 43 (2019) 29–64. doi:10.1002/er.4196.

[77] S. Edsjø, B. Petter, Phase change materials and products for building applications A, 94 (2015) 150–176.

[78] Y. Hu, F. Niu, S. Deng, N. Mao, M. Song, Review on building energy performance

improvement using phase change materials, Energy Build. 158 (2017) 776–793. doi:10.1016/j.enbuild.2017.10.066.

[79] F. Souayfane, F. Fardoun, P.H. Biwole, Phase change materials (PCM) for cooling applications in buildings: A review, Energy Build. 129 (2016) 396–431. doi:10.1016/j.enbuild.2016.04.006.

[80] P. Schossig, H.M. Henning, S. Gschwander, T. Haussmann, Micro-encapsulated phase-change materials integrated into construction materials, Sol. Energy Mater. Sol. Cells. 89 (2005) 297–306. doi:10.1016/j.solmat.2005.01.017.

[81] O. Zubillaga, M. Nogués, M. Medrano, L.F. Cabeza, C. Castellón, R. Leppers, Use of microencapsulated PCM in concrete walls for energy savings, Energy Build. 39 (2006) 113–119. doi:10.1016/j.enbuild.2006.03.030.

[82] F. Kuznik, J. Virgone, J.J. Roux, Energetic efficiency of room wall containing PCM wallboard: A full-scale experimental investigation, Energy Build. 40 (2008) 148–156. doi:10.1016/j.enbuild.2007.01.022.

[83] F. Berroug, E.K. Lakhal, M. El Omari, M. Faraji, H. El Qarnia, Thermal performance of a greenhouse with a phase change material north wall, Energy Build. 43 (2011) 3027–3035. doi:10.1016/j.enbuild.2011.07.020.

[84] C. Liu, D. Feldman, D. Banu, D. Hawes, A.K. Athienitis, Investigation of the thermal performance of a passive solar test-room with wall latent heat storage, Build. Environ. 32 (2002) 405–410. doi:10.1016/s0360-1323(97)00009-7.

[85] E. Meng, H. Yu, B. Zhou, Study of the thermal behavior of the composite phase change material (PCM) room in summer and winter, Appl. Therm. Eng. 126 (2017) 212–225. doi:10.1016/j.applthermaleng.2017.07.110.

[86] M. Zhang, M.A. Medina, J.B. King, Development of a thermally enhanced frame wall with phase-change materials for on-peak air conditioning demand reduction and energy savings in residential buildings, Int. J. Energy Res. 29 (2005) 795–809. doi:10.1002/er.1082.

[87] K.O. Lee, M.A. Medina, Using phase change materials for residential air conditioning peak demand reduction and energy conservation in coastal and transitional climates in the State of California, Energy Build. 116 (2016) 69–77. doi:10.1016/j.enbuild.2015.12.012.

[88] M. Sayyar, R.R. Weerasiri, P. Soroushian, J. Lu, Experimental and numerical study

of shape-stable phase-change nanocomposite toward energy-efficient building constructions, Energy Build. 75 (2014) 249–255. doi:10.1016/j.enbuild.2014.02.018.

[89] X. Shi, W. Tang, H. Cui, F. Xing, S.A. Memon, Experimental assessment of position of macro encapsulated phase change material in concrete walls on indoor temperatures and humidity levels, Energy Build. 71 (2013) 80–87. doi:10.1016/j.enbuild.2013.12.001.

[90] J.S. Sage-Lauck, D.J. Sailor, Evaluation of phase change materials for improving thermal comfort in a super-insulated residential building, Energy Build. 79 (2014) 32–40. doi:10.1016/j.enbuild.2014.04.028.

[91] J. Lei, J. Yang, E.H. Yang, Energy performance of building envelopes integrated with phase change materials for cooling load reduction in tropical Singapore, Appl. Energy. 162 (2016) 207–217. doi:10.1016/j.apenergy.2015.10.031.

[92] M.I. Hasan, H.O. Basher, A.O. Shdhan, Experimental investigation of phase change materials for insulation of residential buildings, Sustain. Cities Soc. 36 (2018) 42–58. doi:10.1016/j.scs.2017.10.009.

[93] F. Goia, M. Perino, V. Serra, Improving thermal comfort conditions by means of PCM glazing systems, Energy Build. 60 (2013) 442–452. doi:10.1016/j.enbuild.2013.01.029.

[94] A. Sarı, Thermal reliability test of some fatty acids as PCMs used for solar thermal latent heat storage applications, Energy Convers. Manag. 44 (2003) 2277–2287. doi:10.1016/s0196-8904(02)00251-0.

[95] A. Sar, K. Kaygusuz, Some fatty acids used for latent heat storage: Thermal stability and corrosion of metals with respect to thermal cycling, Renew. Energy. 28 (2003) 939–948. doi:10.1016/S0960-1481(02)00110-6.

[96] Z. Fahmi, W. Putri, I. Sutjahja, D. Kurnia, S. Wonorahardjo, Potential of Thermal Energy Storage Using Coconut Oil for Air Temperature Control, Buildings. 8 (2018) 95. doi:10.3390/buildings8080095.

[97] Y. Kang, S.G. Jeong, S. Wi, S. Kim, Energy efficient Bio-based PCM with silica fume composites to apply in concrete for energy saving in buildings, Sol. Energy Mater. Sol. Cells. 143 (2015) 430–434. doi:10.1016/j.solmat.2015.07.026.

[98] S. Wi, J. Seo, S.G. Jeong, S.J. Chang, Y. Kang, S. Kim, Thermal properties of shape-

stabilized phase change materials using fatty acid ester and exfoliated graphite nanoplatelets for saving energy in buildings, Sol. Energy Mater. Sol. Cells. 143 (2015) 168–173. doi:10.1016/j.solmat.2015.06.040.

[99] L. Boussaba, A. Foufa, S. Makhlouf, G. Lefebvre, L. Royon, Elaboration and properties of a composite bio-based PCM for an application in building envelopes, Constr. Build. Mater. 185 (2018) 156–165. doi:10.1016/j.conbuildmat.2018.07.098.

[100] Y. Özonur, M. Mazman, H.Ö. Paksoy, H. Evliya, Microencapsulation of coco fatty acid mixture for thermal energy storage with phase change material, Int. J. Energy Res. 30 (2006) 741–749. doi:10.1002/er.1177.

[101] TS Formica. http://www.formica.com.br/ingles/produtos/datasheets/TSColor.pdf., (2017).

[102] K. Peippo, P. Kauranen, P.D. Lund, A multicomponent PCM wall optimized for passive solar heating, Energy Build. 17 (1991) 259–270. doi:10.1016/0378-7788(91)90009-R.

[103] U. (UC B. The biomes group, The desert biome, UC, Berkeley. (2004). https://ucmp.berkeley.edu/glossary/gloss5/biome/deserts.html (accessed December 9, 2019).

[104] Climate-data.org, Abha climate, (n.d.). https://en.climate-data.org/asia/saudi-arabia/asir-region/abha-3634/ (accessed December 9, 2019).

[105] Pce-instruments, Products ans solutions for the industry, (n.d.). http://www.pce-instruments.com (accessed December 9, 2019).

[106] Hukseflux thermal sensors, SR22 pyranomete, (n.d.). https://www.hukseflux.com/ (accessed December 9, 2019).

[107] Blender.org, Blender, (n.d.). http://www.blender.org (accessed December 9, 2019).

[108] B. Drury, O. Curtis, K. Linda, C. Frederick, EnergyPlus : Energy simulation program, ASHRAE J. 42 (2000) 49–56.

[109] R. Southall, F. Biljecki, The VI-Suite: a set of environmental analysis tools with geospatial data applications, Open Geospatial Data, Softw. Stand. 2 (2017) 1–13. doi:10.1186/s40965-017-0036-1.

[110] C. Charach, Y. Zarmi, A. Zemel, SIMPLE METHOD FOR ASSESSING THE THERMAL PERFORMANCE OF PCM PANELS, Advances in Solar Energy Technology, 1987. doi:10.1016/B978-0-08-034315-0.50235-4.

[111] J.B. Drake, A Study of the Optimal Transition Temperature of PCM Wallboard for Solar Energy Storage, Oak Ridge Natl. Lab. Rep. ORNL/TM-10210. (1987) 1–14.